Titre: Title:	Transient Heat Transfer in Vertical Ground Heat Exchangers
Auteur: Author:	Ali Salimshirazi
Date:	2012
Type:	Mémoire ou thèse / Dissertation or Thesis
Référence: Citation:	Salimshirazi, A. (2012). Transient Heat Transfer in Vertical Ground Heat Exchangers [Ph.D. thesis, École Polytechnique de Montréal]. PolyPublie. https://publications.polymtl.ca/908/

UNIVERSITÉ DE MONTRÉAL

TRANSIENT HEAT TRANSFER IN VERTICAL GROUND HEAT EXCHANGERS

ALI SALIMSHIRAZI

DÉPARTEMENT DE GÉNIE MÉCANIQUE

ÉCOLE POLYTECHNIQUE DE MONTRÉAL

THÈSE PRÉSENTÉE EN VUE DE L'OBTENTION

DU DIPLÔME DE PHILOSOPHIAE DOCTOR

(GÉNIE MÉCANIQUE)

JUILLET 2012

UNIVERSITÉ DE MONTRÉAL

ÉCOLE POLYTECHNIQUE DE MONTRÉAL

Cette thèse intitulée:

TRANSIENT HEAT TRANSFER IN VERTICAL GROUND HEAT EXCHANGERS

présentée par : SALIMSHIRAZI Ali

en vue de l'obtention du diplôme de : Philosophiae Doctor

a été dûment acceptée par le jury d'examen constitué de :

M. KUMMERT Michaël, Ph.D., président
M. BERNIER Michel, Ph.D., membre et directeur de recherche

M. PASQUIER Philippe, Ph.D., membre

M. HARRISON Stephen, Ph.D., membre

DEDICATION

To my dear parents:

Mrs. Mina Salman

Mr. Mohammad-Ali Salim Shirazi

for their boundless love and support.

ACKNOWLEDGEMENTS

My years of graduate study are nearing completion. This is the opportune moment to convey my gratitude to all who crossed my path during this journey, contributed and shown me the way.

Undoubtedly, my supervisor, Professor *Michel Bernier* deserves to be at the top of the list. It was an excellent opportunity to work under his tutelage. I am sincerely grateful to him for his kind guidance, precious advises, availability, encouragement and confidence in me. His exceptional high standards inspired me to improve my skills and progress academically.

I would like to extend my thanks to all the present and former students of my supervisor for the discussions we had and sharing their knowledge and friendship with me; my good friends: *Parham*, *Simon*, *Antoine*, *Yannick*, *Massimo*, *Daniel*, *Demba* and *Hervé.* My special thanks go to *Parham Eslami Nejad* for his assistance in calibrating the thermocouples used in my experiments.

I am deeply grateful to Prof. *B. R. Baliga* for the knowledge I acquired from his incredible lectures. I am thankful to the staffs of Mechanical Engineering Department specially Mr. *Jean-Marie Béland* for his superb work on my experimental apparatus. I'd like to express my gratitude to *Dr. Kummert*, *Dr. Pasquier* and *Dr. Harrison* for accepting to be a member of the jury.

I have made many friends in Montreal and the best memories are the times I spent with them. My Special thanks to *Soroush Shahriary* for his help during the first years of my Ph.D. also to my best friend, *Shahram Tabandeh* whom I know from school days. I had great times playing drums in our *École Polytechnique Professors Jazz Quartet Band*, thanks *Christian*, *Richard* and *Michel*. Special thanks to my violins and drum-set as well as all my music teachers, mentors and heroes.

Also, I would like to acknowledge the financial support of the *Solar Building Research Network (SBRN)* which funded most of this work.

I am grateful to my dear Aunt, *Nahid Salman* and Uncles Dr.*R. Salman* and Dr. *M. Salim Shirazi.*

Last, but most importantly, I would like to thank my parents and my lovely sisters Maryam and Fatemeh; whose unconditional love and encouragement have always been a great support to me.

Ali SALIM SHIRAZI

Montréal, Québec, Canada, July 2012

RESUME

Cette thèse porte sur le transfert de chaleur en régime transitoire à l'intérieur et au voisinage de puits géothermiques verticaux.

Un modèle hybride analytique-numérique unidimensionnel du transfert de chaleur dans les puits géothermiques est d'abord présenté. Dans ce modèle, le transfert de chaleur à l'intérieur du puits est traité numériquement alors que pour l'extérieur du puits la méthode de la source cylindrique est utilisée. Cette approche unidimensionnelle s'appuie sur plusieurs hypothèses qui sont rigoureusement présentées. De plus, plusieurs intervalles de temps doivent être considérés à partir du temps de résidence du fluide dans le puits jusqu'au pas de temps des simulations énergétiques en passant par le pas de temps des simulations numériques dans le puits. Le modèle hybride est validé avec succès en le comparant à des résultats numériques et à des résultats d'une expérience de terrain. Il est ensuite utilisé dans des simulations énergétiques d'une pompe à chaleur géothermique mono étagée reliée à un puits géothermique et opérant sur une saison de chauffage. Deux types de simulations sont réalisés, d'abord en considérant la capacité thermique du puits et ensuite en la négligeant. Les résultats montrent que le coefficient de performance (COP) annuel de la pompe à chaleur peut être sous-estimé de 4 à 4.6% lorsque les simulations ne tiennent pas compte de la capacité thermique du coulis et du fluide dans le puits géothermique.

Une part importante de ce travail a porté sur la conception, la construction, et la mise en service d'une installation expérimentale à échelle réduite (1/100) pour l'étude du transfert de chaleur transitoire au voisinage de puits géothermiques dans un bac à sable. Cette installation comprend : i) un puits géothermique d'une longueur de 1.23 m muni d'un tube en U précisément positionné et rempli de petites billes de verre qui agissent comme coulis; ii) une soixantaine de thermocouples étalonnés et localisés précisément dans le bac au moyen de fils tendus permettant de mesurer la température du sable; iii) du sable de qualité laboratoire dont on connait les propriétés thermiques; iv) de l'équipement de conditionnement du fluide caloporteur permettant d'alimenter le puits avec le débit et la température voulus.

Cette installation expérimentale s'est avérée être indispensable pour la validation du modèle numérique bi-dimensionnel et axi-symmétrique développé dans le cadre de cette thèse. Les résultats numériques issus de ce modèle se comparent très favorablement aux résultats expérimentaux alors que la plupart des résultats sont à l'intérieur de la bande d'incertitude

expérimentale. Les températures mesurées à la paroi du puits le long de la circonférence semblent corroborés certains résultats analytiques récents générés à l'aide de la méthode multipole.

ABSTRACT

Transient heat transfer inside and in the vicinity of vertical ground heat exchangers is the main focus of the present thesis.

A hybrid analytical-numerical one-dimensional model is presented where heat transfer in the borehole is treated numerically and ground heat transfer is handled with the classic cylindrical heat source analytical solution. The one-dimensional approach imposes several assumptions which are rigorously presented. As well, the model requires careful treatment of the various time periods from the residence time of the fluid in the borehole to the energy simulation time and including the time steps of the numerical simulation. The hybrid model is successfully validated against analytical solutions and field data. It is used in simulations over an entire heating season with a single-stage geothermal heat pump linked to a borehole. Two sets of simulations are performed: with and without borehole thermal capacity. Results show that for a typical borehole, the annual heat pump coefficient of performance (COP) can be underestimated by 4 to 4.6% when the borehole simulations do not account for the grout and fluid thermal capacities.

A significant level of effort went into the design, construction, and commissioning of a small-scale (1/100) experimental sand tank to study transient heat transfer in the vicinity of boreholes. The main features of the facility include: i) an instrumented 1.23 m long borehole with a carefully positioned U-tube and filled with well-characterized small glass beads which act as the grout; ii) a string rack instrumented with some 60 calibrated thermocouples precisely located for sand temperature measurement; iii) laboratory-grade sand with known thermal properties; iv) fluid conditioning equipment that allow to feed the facility with user-specified inlet temperature and flow rate.

The experimental facility proved to be invaluable for validating a two-dimensional axi-symmetric numerical model developed for this study. Comparison results show that the numerical results are in very good agreement with the experimental data with most of the results lying within the experimental uncertainty. The measured azimuthal temperature variation at the borehole wall seems to corroborate recent findings obtained using the analytical multipole method.

TABLE OF CONTENTS

LIST OF TABLES

LIST OF FIGURES

LIST OF APPENDICES

NOMENCLATURE

a	coefficient of the discretization equations
BC-B	bottom boundary condition
BC-L	left boundary condition
BC-R	right boundary condition
BC-T	top boundary condition
c	specific heat (kJ/kg-K)
D	half the centre-to-centre distance between pipes in the U-tube configuration (m)
D_b	borehole diameter (m)
D_{eq}	diameter of the equivalent pipe (m)
D_p	diameter of U-tube pipes (m)
dt	time step (s)
f	flow meter output signal (Hz)
F_0	Fourier number ($Fo = \alpha_{gd} t / r_{bore}^2$)
G	G-factor in the CHS method
h	film coefficient (W/m^2-K)
H	overall height of the calculation domain for the proposed 2-D model (m)
int	integer figure
IT	internal time, number of intermediate calculations during each *TI* (-)
k	thermal conductivity (W/m-K)
L	active borehole length (m)
L1	vertical distance from ground surface to the top of borehole as shown in Figure 3.2 (m)
L2	vertical distance below the of borehole as shown in Figure 3.2 (m)

m measured mass (kg)

$\dot{m}$ mass flow rate (kg/s)

NI number of calculations done in the numerical borehole model during each RT (-)

q' rate of heat transfer per unit length at the equivalent pipe wall (W/m)

q'' heat flux imposed at the inner pipe wall (W/m^2)

r radial distance from the borehole center (m)

r_b borehole radius (m)

r_{eq} equivalent pipe radius = $D_{eq}/2$ (m)

r_p pipe radius of the U-tubes pipes (m)

$R_{b,ss}$ steady state borehole thermal resistance for the real single U-tube borehole geometry (K-m/W)

RT residence time Figure 2.5

t time (s)

t_{res} residence time (s), given by Equation (2.5)

T temperature (°C)

TI time increment, the time between two step changes in inlet conditions (s)

T_i inlet fluid temperature to the borehole (ºC)

T_m mean fluid temperature = $(T_i + T_o)/2$ (ºC)

T_o outlet fluid temperature from the borehole (ºC)

$T_{r_{eq}}$ temperature at r_{eq} (ºC)

T_w borehole wall temperature (ºC)

u fluid velocity (m/s)

U uncertainty

z axial coordinate along the borehole depth (m)

Subscripts

bore associated with the borehole wall

b bottom neighbor

e east neighbor

eq associated with the equivalent diameter pipe

f fluid

gd ground

gt grout

i internal, inlet

in internal (for internal radius in Chapter 3)

n north neighbor

o external, outlet

p associated with the U-tube pipes also denotes point in discretization equations

real associated with the real U-tube configuration

eq associated with the equivalent pipe wall

s south neighbor

t top neighbor

w west neighbor

∞ far field

Superscripts

^{0} value at the preceding time step

Greek letters

α thermal diffusivity (m^2/s)

δr radial distance between two control-volume faces (m)

δz *axial* distance between two control-volume faces (m)

Δr radial increment (m)

Δzr axial increment (m)

Δt time step (s)

θ temperature at a particular radial distance minus that of the far field; $\theta(r,t)=T(r,t)-T_\infty$ (ºC)

σ standard deviation

ρ density (kg/m^3)

Abbreviations

1-D	one dimensional
2-D	two dimensional
CHS	cylindrical heat source
COP	coefficient of performance
DST	duct ground heat storage model
FLS	finite line source
GCHP	ground coupled heat pump
GHE	ground heat exchanger
GSHP	ground source heat pump
HDPE	high density polyethylene
ILS	infinite line source
TC	thermocouple
TCI-IN	T-type hollow tube thermocouple measuring fluid temperature at inlet side
TCI-OUT	T-type hollow tube thermocouple measuring fluid temperature at outlet side

INTRODUCTION

Background and generalities

The energy consumed in residential and commercial/institutional buildings account for almost 30 percent of the total annual energy consumption in Canada (NRCan, 2006). Approximately 60 percent of this amount is used for space heating and cooling. A recent report by The National Round Table on the Environment and the Economy and Sustainable Development Technology Canada indicates that the commercial building sector is accountable for 14% of the end-use energy consumption and for 13% of the carbon emissions in Canada. Furthermore, the recent environmental ambition to reduce carbon emissions has given rise to extensive research on alternative, low-cost energy sources and on energy efficiency measures.

Ground coupled heat pump systems are energy-efficient, environment friendly and sustainable alternatives (Nouanegue et al. (2009)) to conventional systems. In general, these systems collect (or reject) heat through ground heat exchangers which can be installed either vertically or horizontally. This research concentrates on vertical systems.

A schematic representation of a vertical ground heat exchanger (GHE) is shown in Figure 0.1. It consists of a borehole in which a U-tube pipe has been inserted. The borehole is usually filled with a grout to enhance heat transfer by providing good thermal contact between the fluid and the ground. The grout is also used to protect underground aquifers. The depth of the borehole (L) is approximately 100 m (328 ft) and its diameter is usually in the 10-15 cm range (4 to 6 inches) while the inside diameter of the U-tube pipes is approximately 25 mm (1 inch). High density polyethylene (HDPE) pipes are used for the U-tubes. The center-to-center distance between these pipes varies from cases where the pipes are touching each other to cases where the pipes are touching the borehole wall on opposite sides. A fluid is pumped into the U-tube. In heating, the fluid has a lower temperature than the ground and heat is transferred from the ground to the fluid. In cooling, heat transfer is in the opposite direction as the fluid is at a higher temperature than the ground. The borehole can experience a variety of flow rates ranging from no flow to full flow conditions and any flow in between if the system is equipped with a variable flow pumping system. At full flow, the residence time, i.e., the time required for the fluid to travel from the inlet to the outlet, is of the order of a few minutes. The temperature difference between the inlet (T_i)

and outlet (T_o) temperatures will vary according to the flow rate with typical values around 5 ºC (9 ºF).

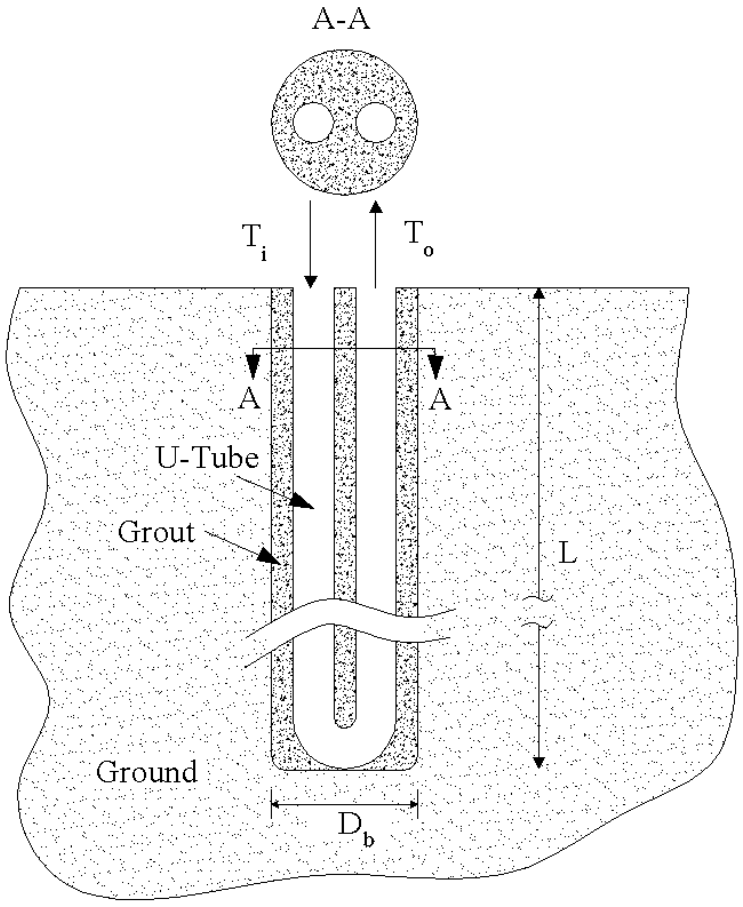

Figure 0.1: Schematic representation of a typical single U-tube ground heat exchanger.

Variations in the inlet conditions (either temperature or flow) do not translate immediately into a similar change in the outlet conditions. This is due to two main reasons. First, the residence time of the fluid in the borehole creates a delay. Second, any changes at the inlet are dampened by the fluid and grout thermal capacities.

Problem definition

Determination of the length of the geothermal heat exchanger is one of the fundamental issues in designing a reliable ground coupled heat pump system. Over estimation of the GHE length leads to high installation costs while under-sizing may lead to operational problems resulting from

ground return fluid temperature that are outside the heat pump operating range. Accurate prediction of the outlet fluid temperature from the borehole is important for design purposes, building annual energy simulations and estimation of the heat pump energy consumption. Therefore, accurate heat transfer predictions in and around boreholes is important.

In general, ground heat exchanger models are divided into two distinct regions each with its own time scale with rapid changes inside the borehole and slow variations of ground temperature far away from the borehole. The current study concentrates on the borehole and its immediate vicinity. There are a number of borehole models in the literature that can be used to predict the thermal behavior of boreholes. With a few exceptions, most of these models are steady-state models which neglect the thermal capacity of the boreholes by simply replacing the borehole with a steady-state thermal resistance. While this assumption might be acceptable if the heat pump operates continuously, it is questionable when heat pumps undergo on/off cycles to meet the building load. A paucity of information in the literature has been identified in two areas. First, the effects of grout thermal capacity on the annual energy consumption of heat pumps have not been studied extensively. Second, field-monitored data are usually inadequate for precise model validation and there is a lack of good experimental data obtained in controlled conditions. Given these gaps in the literature, this work was undertaken with the following objectives.

Objectives

The objectives of this study are to:

1. develop a computationally efficient transient one-dimensional model that accounts for grout and fluid thermal capacity that could be incorporated in energy simulation programs;
2. develop a two-dimensional numerical model of the ground in the vicinity of boreholes;
3. design and construct a small-scale experimental apparatus to validate the current models and to provide a database for future works.

Organization of this thesis

Aside from the introduction and conclusion, this thesis is structured around five chapters and five appendices. Chapter 1 addresses previous research considered relevant to this study. The hybrid one-dimensional transient model is presented in Chapter 2 along with results on the impact of borehole thermal capacity on the annual heat pump energy consumption. It should be noted that Chapter 2 has been submitted to a journal for publication. A two-dimensional numerical model of the ground is presented in Chapter 3; verifications with other solutions are provided. Chapter 4 describes the experimental set-up and the results of a preliminary experiment. The final set of experimental results is presented in Chapter 5 including comparisons with the model developed in Chapter 3. A detailed flowchart is presented in Figure 0.2 to illustrate the various steps undertaken during the course of this study.

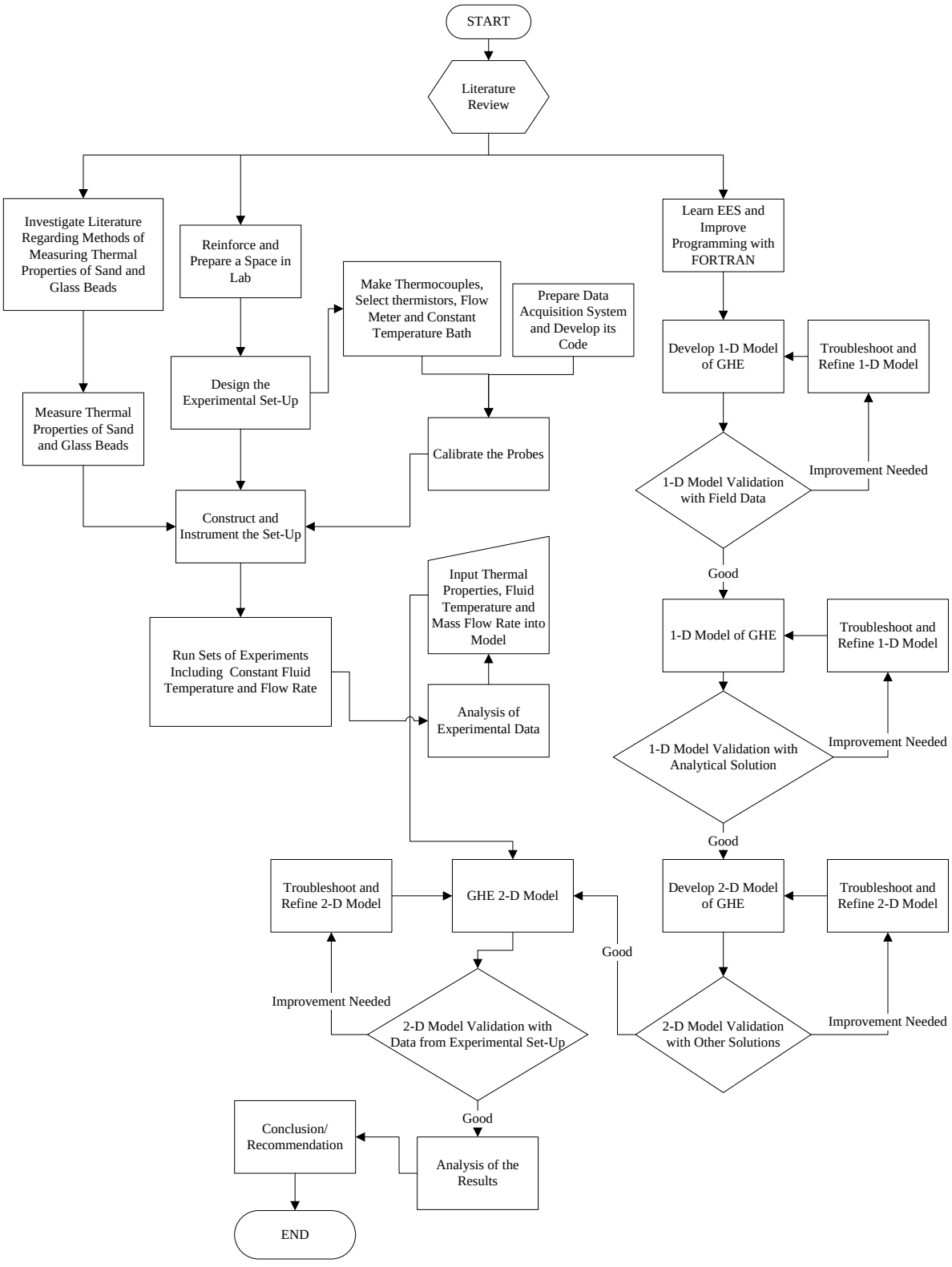

Figure 0.2: Flow chart illustrating the work done in this study.

CHAPTER 1 LITERATURE REVIEW

1.1 Introduction

Transient heat transfer inside and in the vicinity of vertical ground heat exchangers (GHE) is the main focus of this thesis. Existing models used for analyzing vertical GHE are described in this chapter. First, a brief review of some of the fundamental studies on ground heat transfer for boreholes and bore field is presented. Then, previous works related to modeling of GHE is reviewed.

1.2 Fundamental studies on ground heat transfer

There are two major analytical solutions to the transient heat transfer equation in cylindrical coordinates. They are referred to as the line source (either infinite of finite) and the cylindrical heat source solutions. A brief review of these solutions is presented in the following paragraphs.

1.2.1 Infinite line source (ILS) method

The line source theory, first introduced by Lord Kelvin in 1882, is considered as one of the most basic analytical transient one-dimensional solutions which can be used for geothermal applications. As schematically shown in Figure 1.1, the borehole geometry is approximated by an infinite line source/sink surrounded by an infinite homogeneous medium (i.e., ground). Pure heat conduction in the ground is assumed and the solution is one-dimensional in the radial direction. When using the ILS it should be realised that the heat transfer rate is applied at the center of the borehole. The time it takes for a heat impulse at the center to reach steady-state at the borehole wall (for $D_b/2 = r_b \approx 5$ to 7.5 cm) has been evaluated by Eskilson (1987) to be equal to $5r_b^2/\alpha$, where α is the thermal diffusivity of the ground. This time, which is typically 3 to 6 hours, corresponds to the time at which the difference between accurate models (such as the *g-function*) and the infinite line source (ILS) solution falls below 10 %. Ingersoll *et al.* (1954) proposed a lower time limit of $20r_b^2/\alpha$, which corresponds to a difference of 3 % according to Philippe et al. (2009). For long operating times (typically of the order of a year), axial heat conduction is significant and the ILS model becomes imprecise.

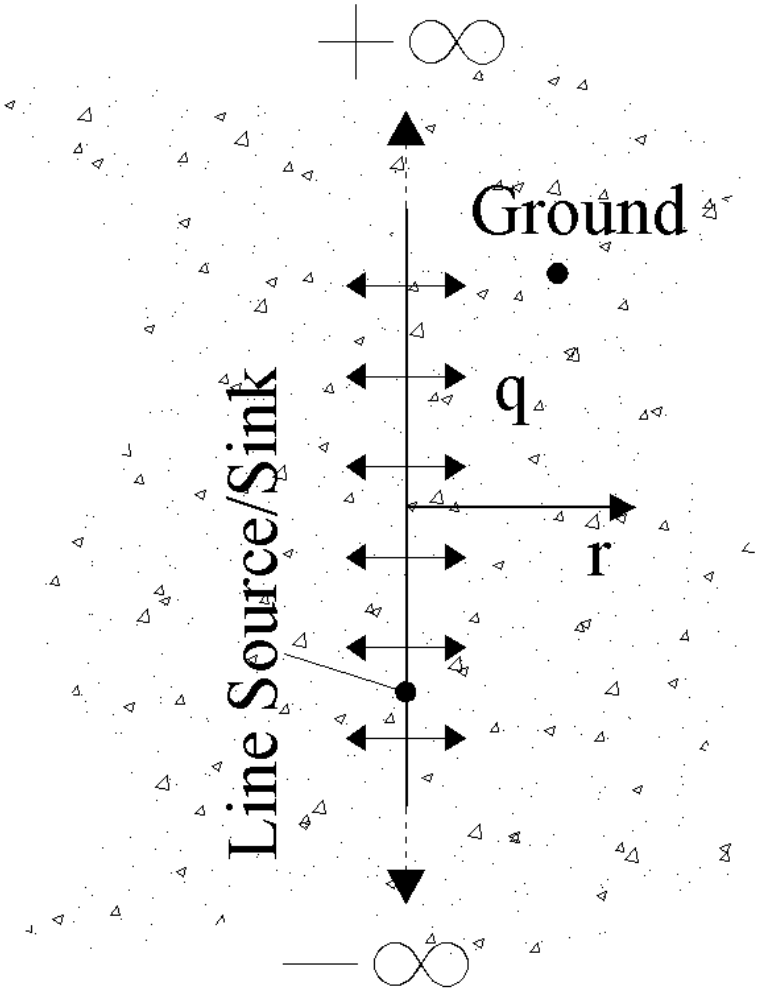

Figure 1.1: Schematic representation of the infinite line source model.

1.2.2 Finite-line source (FLS) method

Eskilson (1987), Diao et al. (2004) and Zeng et al. (2002) developed an explicit solution of a finite line-source to express more accurately the two dimensional temperature response (radial and along the length of the borehole) of vertical boreholes submitted to a uniform heat transfer rate per unit length in a semi-infinite homogeneous constant-property ground, as schematically shown in Figure 1.2. The FLS will be described further in Chapter 3 in conjunction with the presentation of the proposed two-dimensional ground model.

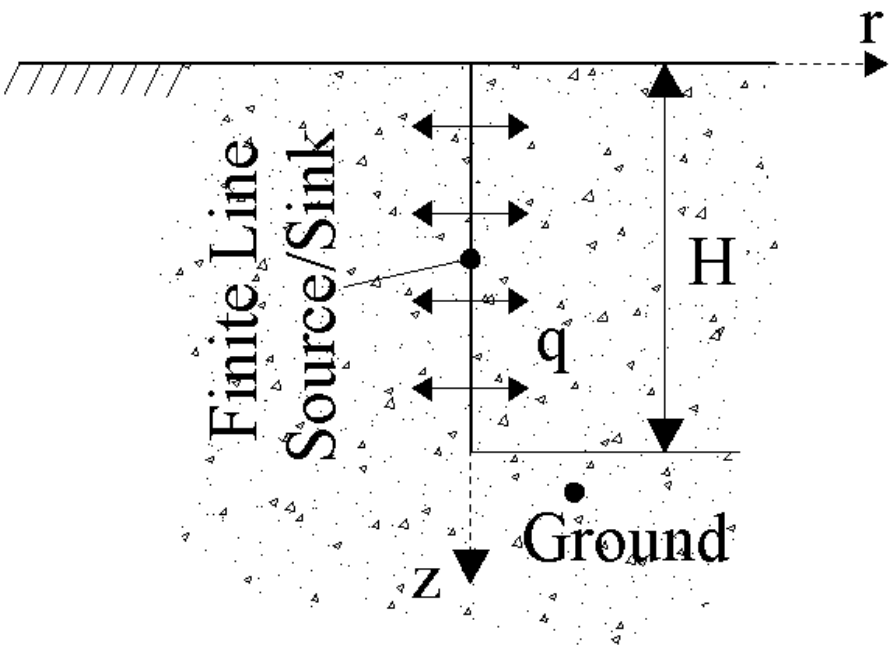

Figure 1.2: Schematic representation of the finite line source model.

1.2.3 Cylindrical heat source (CHS) method

One convenient and simple method of evaluating ground heat transfer is to use the so-called cylindrical heat source (CHS) method which was originally proposed by Ingersoll (1954), based on the work of Carslaw and Jaeger (1947). The CHS method, as shown in Figure 1.3, is based on the analytical solution to transient heat transfer from a cylinder embedded in an infinite homogeneous medium. The CHS solution for constant heat transfer rate is given in terms of a G-factor which depends on F_o, the Fourier number, and p (where p is the ratio of the radius where the point of interest is located over the radius of the borehole). The solution to the G-factor involves the solution of a relatively complex integral (Bernier, 2000 ; Bernier, 2001). Fortunately, tabulated values of G are available for p=1, 2, 5,and 10 Ingersoll (1954). In addition, Bernier and Salim Shirazi (2007) have recently proposed G-factor correlations for p = 20, 50 and 100. The CHS method suffers form its inherent one-dimensional nature and like the line source method it becomes inaccurate for long operating time when axial conduction becomes significant. According to the recent work of Sheriff (2007) axial conduction starts to be significant for $\alpha t/r^2 > 10^4$.

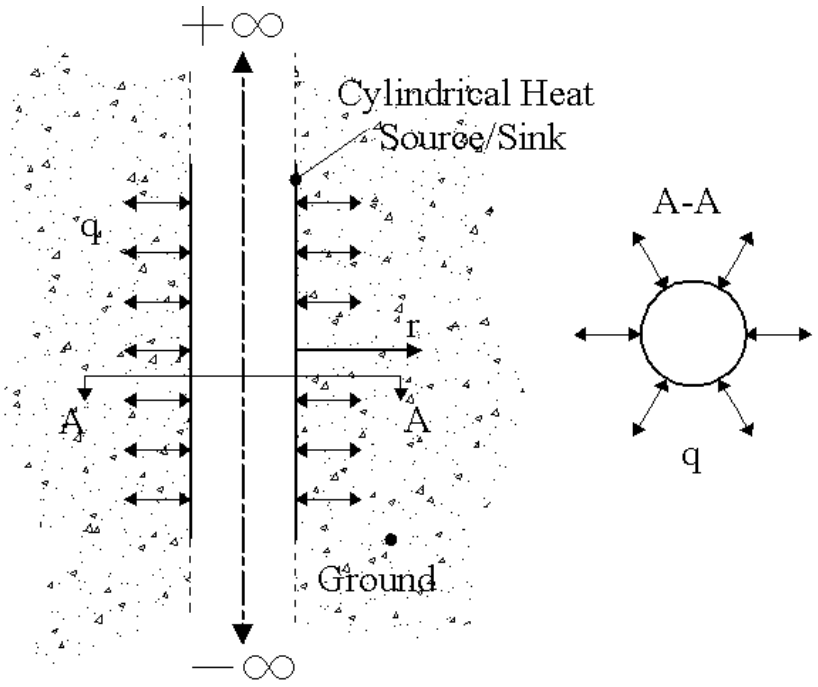

Figure 1.3: Schematic representation of the cylindrical heat source (CHS) method.

Philippe et al. (2009) compared the infinite line source, the infinite cylindrical source and the finite line source models and a validity map was presented for typical operating conditions. They showed that if the relative error of the borehole wall temperature is to be kept below a certain value, say 2%, the infinite line source model can be applied after 34 hours and up to 1.6 years of operation. For operation time below 34 hours, the infinite cylindrical source is recommended to stay below the same level of error. After 1.6 years of operation, the two-dimensional effects become significant and the finite line source should be used.

1.2.4 Other analytical approaches

Man et al. (2010) proposed analytical models for 1D and 2D solid cylindrical heat sources (with infinite and finite vertical dimension, respectively) which can be used for modeling pile GHEs with spiral coils. The models take the simplifying assumption of replacing the spiral heating coil with a continuous cylindrical heat source with no thickness, mass or heat capacity as shown in Figure 1.4. They account for the heat capacity of the borehole or pile by assuming a homogeneous medium for the whole calculation domain including the solid cylindrical region

inside the pile. The infinite heat source model was compared by the authors against the classical line source and “hollow” cylindrical source models.

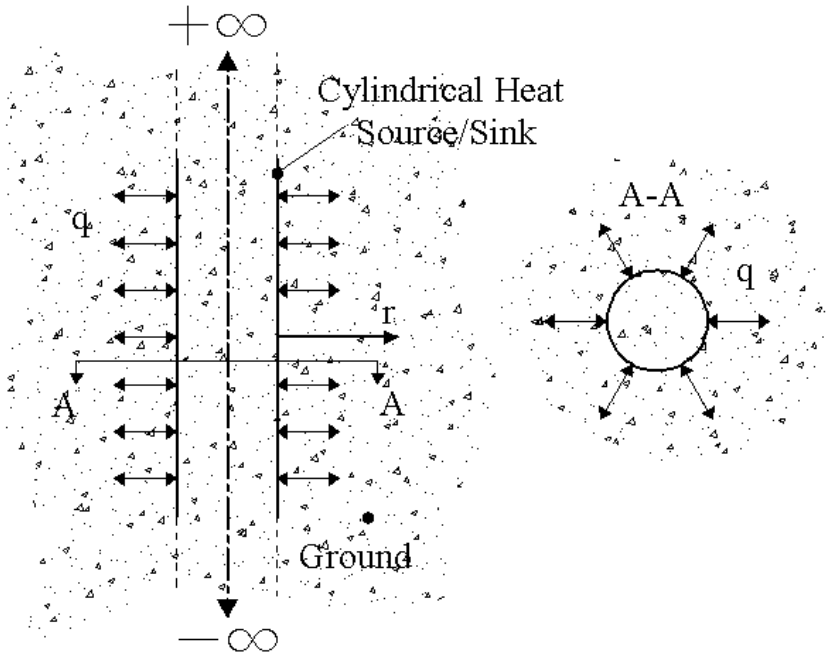

Figure 1.4: Schematic representation of the model proposed by Man et al. (2010).

An analytical solution to the heat flow from an infinite buried cable to its surrounding ground was proposed by Carslaw and Jaeger (1947). As illustrated in Figure 1.5, the cable consists of the following layers: a metal core, insulation and an outer protective sheath. Unlike the line source and cylindrical heat source methods, the buried cable model takes into account the thermal capacities of the metal core and protective sheath. However, their thermal resistances are ignored due to their high thermal conductivities. On the other hand, the thermal resistance of the insulation ring is accounted for while its thermal capacity is neglected.

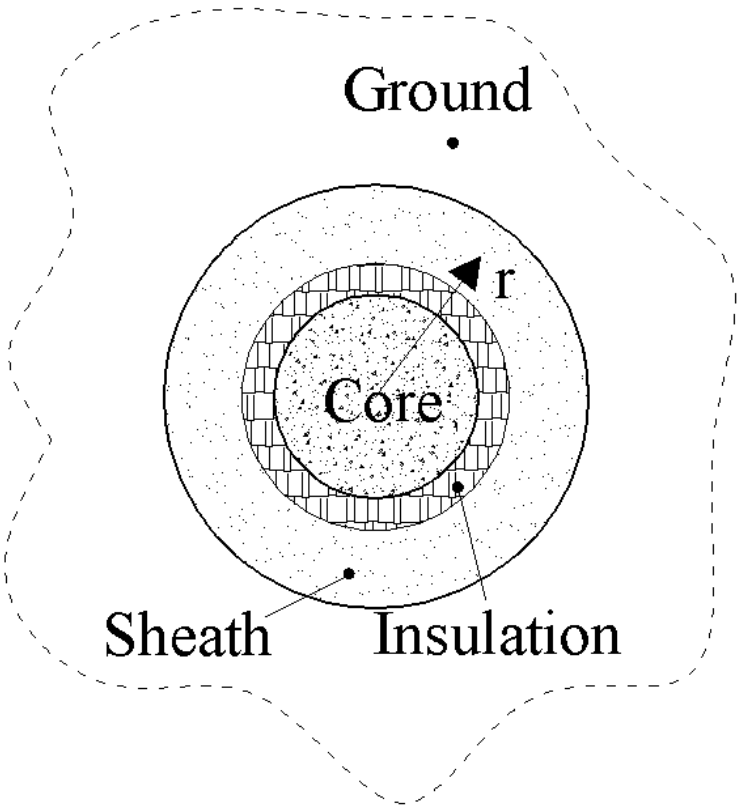

Figure 1.5: Cross section of the buried cable used by Carslaw and Jaeger (1947).

An analytical approach for evaluating the short time response of boreholes, based on the buried cable solution, is proposed by Young (2001). In that solution, the electrical cable consists of a current carrying core separated from a metal sheath by insulation which acts as a contact thermal resistance. By analogy, Young replaced the core with the working fluid and the metal sheath with grout thermal capacity. The contact resistance represents the steady state thermal resistance. It is expressed using the multipole approach proposed by Bennet et al. (1987). To improve the accuracy of the model, Young considered moving part of the grout thermal capacity from the outside of the thermal resistance to the inside by introducing a grout allocation factor, GAF. The total thermal mass of the working fluid was taken into account. It included the thermal mass of the fluid inside the U-tube as well as in the distribution piping system connected to the GHEs. The goal was to study the effect of the total fluid thermal mass on the working fluid temperature during the peak loads as well as the impact of the peak load duration on the fluid temperature in peak load dominant buildings such as churches. This effect was introduced using a fluid

multiplication factor. It was shown that the choice of the fluid multiplication factor has an important impact on the GHE design.

After examining and comparing several existing steady state methods, Young concluded that the method chosen to calculate the borehole thermal resistance has also a significant effect on the estimated length of the GHE. Among available methods, the multipole method of Bennet et al. (1987) was selected as the best analytical steady state approach. Young indicated that the grout thermal resistance was highly sensitive to the U-tube diameter, shank spacing between the U-tube pipes, borehole diameter, as well as the grout and ground thermal conductivities. When the U-tube legs touch the borehole wall, the thermal mass of the grout has less of an impact as most of the heat can be transferred directly to the ground. Young compared his model against the line source model for an hourly annual simulation of a small office building. He concluded that the heat pump energy consumption calculated by the line source model is as precise as his proposed model. Yet, Young mentioned that for short duration peak loads, line source over predicts the peak outlet fluid temperature from the borehole by as much as 1.3ºC.

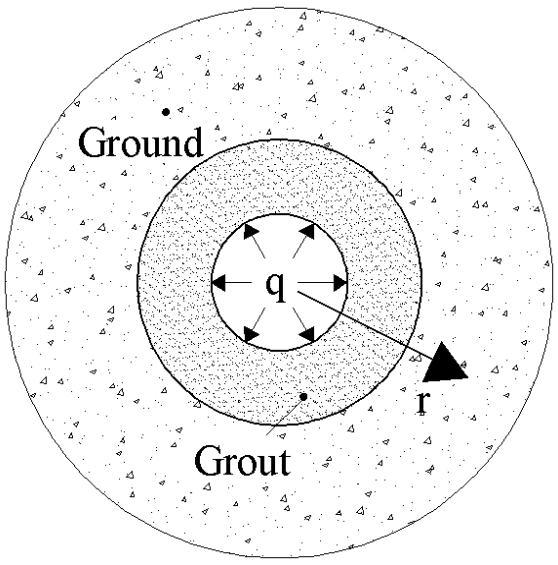

Figure 1.6: Schematic representation of the geometry used by Lamarche and Beauchamp (2007).

Using the method of optimal linearization, with the initial solution given by the integral method, Kandula (2010) presented a closed form approximate solution of the transient temperature distribution in a hollow cylinder with a linear variation of thermal conductivity with temperature. The boundary conditions are convective heating at the exposed inner surface while the outer

surface is adiabatic. The non-linear analytical solution compares well with the finite difference numerical solution.

1.3 Bore field models

As schematically shown in Figure 1.7, some installations have more than one borehole. Analytical solutions such as the ones presented in the previous section have to be superimposed in space when there is borehole thermal interference in a bore field (Chapuis, 2009). Two of the most popular approaches to model bore fields are the g-function concept introduced by Eskilson (1987) and the DST model from Hellström (1991). These two approaches will now be briefly reviewed.

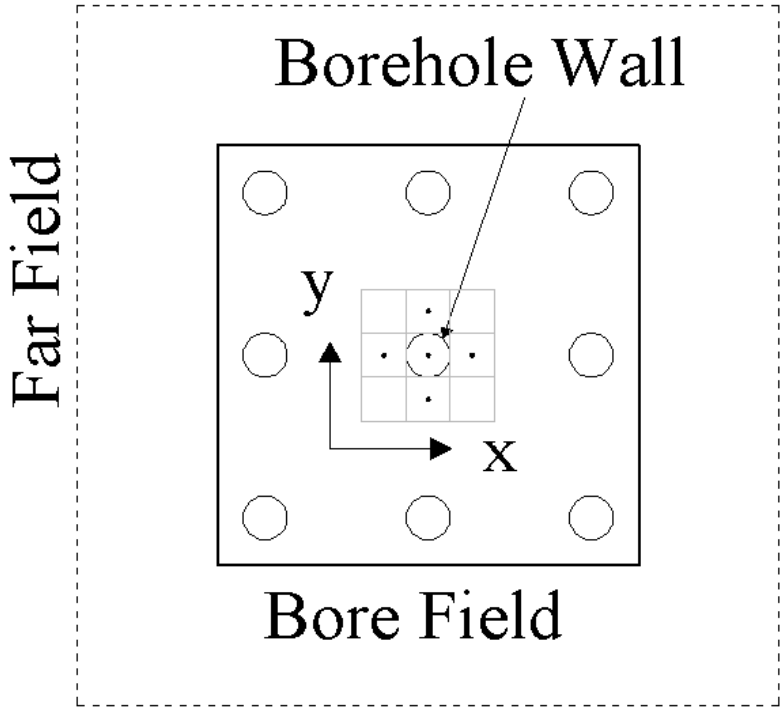

Figure 1.7: Schematic representation of a 3 × 3 bore field.

Eskilson's model calculates the average borehole wall temperature in a bore field using numerical solution techniques. Only heat transfer in the ground is considered and heat transfer inside the borehole has to be accounted for using another model. The numerical model solves the governing equations in a radial-axial cylindrical coordinate system using the finite difference method. A

spatial superimposition technique is used to obtain the response of the whole bore field. The g-functions which are a set of non-dimensional temperature response factors are derived from the temperature response of the bore field. The g-functions facilitate the calculation of the temperature change at the borehole wall corresponding to a step heat input. Once the response of the bore field to a single step heat pulse is represented by a g-function, its response to any heat rejection/extraction function can be determined by simply converting the heat rejection/extraction into a set of step functions and superimposing the response to each step function. The g-functions are presented as curves, plotted versus non-dimensional time, $\ln(t/t_s)$, where $t_s = H^2/(9\alpha)$ is the time scale and H is the borehole vertical length. Each g-function curve corresponds to a particular r_b/H, where r_b is the borehole radius, and a single B/H where B is the distance between the boreholes. As the number of boreholes increases, the thermal interaction between them becomes stronger especially for long operating time periods. For short operating times, Eskilson considers the g-functions to be valid for times greater than $5(r_b)^2/\alpha$.

Hellström (1991) developed a three dimensional simulation model for seasonal thermal energy storage equipped with ground source heat exchangers. The storage temperature is calculated by considering the following three components: a local solution, a global temperature and a steady flux solution. The local component takes into account the convective rate of heat transfer from the circulating fluid to the heat store volume while the global component considers the conductive heat transfer between the boreholes and the cylindrical volume by implementing the temperature difference between the heat store volume and the undisturbed ground temperature. These two solutions are obtained using an explicit finite difference approach. The steady flux component which takes into account the distribution of the heat coming from the fluid to the borehole and then diffusing to the cylindrical soil volume is determined analytically. Finally, the ground temperature distribution is obtained through superposition methods. Hellström's model, also known as the DST model, has been implemented in TRNSYS. It is considered one of the most accurate bore field models. The reader is referred to the work of Chapuis (2009) and Chapuis and Bernier (2009) for a complete description of the DST model.

1.4 Heat transfer modeling inside the borehole

This section reviews heat transfer models for the inside of the borehole. Other papers on the same subject, but more pertinent to Chapter 2, are included in that chapter.

Some early but fundamental work on borehole modeling was done by Kavanaugh (1985). In his work, he determined the rate of heat transfer or the temperature distribution around a buried pipe in the ground using the cylindrical heat source solution. He developed the cylindrical heat source approach considering a single isolated pipe surrounded by an infinite solid (soil) having constant properties. Kavanaugh also makes some adjustments to the cylindrical heat source approach to get a better match with his experimental data. Deerman and Kavanaugh (1991) extended the cylindrical heat source model to account for variable heat transfer rates. However, their approach is not suitable for the analysis of short-term field data. Kavanaugh, proposed an equivalent single pipe instead of a U-tube. The equivalent diameter approximates the U-tube geometry and is calculated using $D_{eq} = \sqrt{n}(D_o)$ where n is the number of U-tube legs (2 for a single U-tube).

Muraya et al. (1996) developed a transient two-dimensional finite element model for single U-tube boreholes to analyze thermal interaction between the two pipes of the U-tube. Defining a heat exchanger effectiveness, the thermal interference was quantified by investigating the impacts of the shank spacing, U-tube leg temperatures, ground temperature and backfills. The problem was solved numerically and it was found that the shank spacing and backfill thermal conductivity had the most significant influence on the effectiveness results. To properly account for the backfill thermal conductivity, the effectiveness had to be modified. They reported that the overall heat transfer to the ground can be increased by increasing the shank spacing and backfill thermal conductivity.

Remund (1999) proposed a set of relationships, based on the concept of conduction shape factors, to calculate steady-state borehole thermal resistances. Empirically-based coefficients are presented for three single U-tube borehole configurations, often referred to as the A, B, and C, configurations. It should be mentioned that in the proposed relations, the convection resistance on the inside pipe wall is not included. The Remund relationships are often used because of their simplicity.

Yavuzturk and Spitler (2001) used actual operational field data from an elementary school to validate their short time step temperature response factor model. Reasonable agreement was reported between the measured data and the short time step model, despite some shortcomings in the experimental data set. The predicted entering fluid temperature to the heat pump shows maximum deviation relative to the measured data when the fluid flow rate is discontinuous.

Lee and Lam (2008) studied the performance of ground heat exchangers and proposed a three-dimensional model using the implicit finite difference method in rectangular coordinates. The model approximates each borehole as a square column circumscribed by the borehole radius. Their approach can handle variable temperature and loading along the borehole. However, quasi-steady state heat transfer is assumed inside the borehole. Comparison has been done between simulation results from their model and those of the finite line source as well as cylindrical heat source method.

Cui et al. (2008) developed a finite element numerical model for simulating GHEs in alternative operation modes over a short time period for GCHP applications. It was concluded that for short time scale simulations, the proposed model is more suitable than the line source model.

Bandyopadhyay et al. (2008a) developed a one-dimensional (radial) analytical solution for the transient heat transfer from cylinder in homogeneous media. In order to take into account the thermal capacity of the working fluid, the proposed approach considers it as a “heat generating” virtual solid, VS, which is in direct contact with the grout medium through a thermal contact conductance. A finite element model was used for comparison. By varying the Biot number and comparing the analytical results of fluid temperature with those of the finite element model, they extended the solution to the U-tube geometry. Good agreement was reported for the case where the two pipes of the U-tube were in close contact. In a related article, Bandyopadhyay et al. (2008b) obtained a semi-analytical solution for the short time transient response of a grouted borehole subjected to a constant internal heat generation rate. Using numerical algorithms, the average fluid temperature as well as the borehole wall temperature have been obtained and compared against their corresponding simulated results from finite element models of the actual single U-tube grouted boreholes. Good agreement is reported between the numerical results for boreholes with touching pipes against the results obtain from the proposed method using a single equivalent core. Sensitivity analysis has been done for several non-touching pipes while varying

the Biot number in order to reach a better agreement between the numerical and proposed approaches.

Li and Zheng (2009) introduced a three dimensional unstructured finite volume numerical model of a GHE using a Delaunay mesh generator to capture the geometry of the borehole. The model takes the inlet fluid temperature to the GHE together with volumetric flow rate as input to calculate the outlet fluid temperature. Experimental data (i.e., inlet and outlet fluid temperature) from a so-called ground sink direct cooling system (GSDCS) operating on an intermittent mode (12 hours on, 12 hours off) is used to verify the proposed numerical model. The flow rate is considered to be constant during the whole on-cycle period. The numerical model neglects the conductive heat transfer along the fluid as well as the pipe thermal capacity. The bottom boundary condition is imposed at the bottom of the borehole thus neglecting end effects. Similarly, the top boundary condition is imposed at the ground surface where the top of the borehole is assumed to be located. Hourly comparison curves have been presented showing relatively good agreement between the numerical results and the experimental data except at the start of the operation.

Javed et al. (2009) reviewed and compared several analytical and hybrid models for vertical GHE for short and long term analysis. They addressed the strengths and limitations of these models and concluded that there is a shortage of analytical models when it comes to bore fields. There is also a need for proper analytical models for simulating both the short and long term response of GHEs without distorting the actual borehole geometry.

De Carli et al. (2010) developed a model to simulate the thermal behavior of vertical GHEs based on the electrical analogy using thermal resistances and lumped capacities to solve the unsteady heat transfer phenomenon. The model is capable of simulating three pipe arrangements commonly found in GHEs: single U-tube, double U-tube and coaxial pipe. The simulation domain is divided into a number of overlapped slices in the vertical direction with each slice subdivided into a number of annular regions. Heat transfer between two vertical slices in the vertical direction is neglected and only the heat flux along the radial direction is considered. The borehole thermal capacity (fluid, pipe, and grout) is not taken into account. For the flow, the mean fluid temperature is assumed to have the same value as the outlet fluid temperature in a particular vertical slice. Making these assumptions, the flow temperature profile and ground

temperature at different radial and vertical distances can be determined. Comparison has been done between measured and simulated results and good agreement is reported.

In a recent review article, Lamarche et al. (2010) compared different existing approaches to calculate borehole thermal resistance including the thermal short-circuit between the U-tube pipes. An unsteady 3-D numerical simulation of a single U-tube borehole was performed and good agreement was reported between the axial fluid temperature distribution of a single U-tube borehole obtained from the approach proposed by Zeng et al. (2003) and that of the three-dimensional simulation.

Oppelt et al. (2010) proposed a steady-state model for the grout region inside a certain type of parallel double U-tube configuration. The numerical domain in the vertical direction is divided into a number of non-conducting slices. The grout region of each slice is divided into three elements each one representing a certain temperature zone. The proposed model was combined with an existing model to calculate the temperature distribution within the ground and the fluid. Annual simulations of heat pump operation with a time step of one hour are possible with this model. Comparison has been done between the outlet fluid temperature from the "combined" proposed model against that of a 3D numerical model (developed in ANSYS CFX) during heat pump operation for three different pipe spacings. The comparison showed relatively good agreement especially for the case where the pipes were equally distanced from the borehole center and borehole wall. The proposed model proved to be faster in terms of simulation time compared to the numerical model.

Zeng et al. (2003), based on Hellström's work, established a quasi-three dimensional analytical steady-state solution for single and double U-tube configurations arranged either in series or in parallel. The axial temperature variation along the length of the U-tube can be predicted. This study shows that the double U-tube configuration provides a larger heat transfer area between the flowing fluid and the grout leading to a smaller borehole resistance. For double U-tubes BHEs, the parallel arrangement is suggested. Their results show that increasing the U-tube shank spacing decreases the borehole resistance noticeably. Equivalent borehole thermal resistances are proposed for several combinations of circuit arrangement. Their models also account for thermal interaction between U-tube legs. Diao et al. (2004) adopted the analytical borehole model of Zeng

et al. (2003) and combined it with the finite-line source model to simulate the heat transfer phenomenon inside the borehole as well as its surrounding ground.

Marcotte and Pasquier (2008) proposed a "p-linear" average temperature using a three-dimensional numerical simulation to estimate the borehole thermal resistance from a thermal response test. It was reported that the assumptions of constant heat flux along the borehole length or constant borehole wall temperature lead to an overestimation of the borehole thermal resistance and consequently to the borehole length. The economic impact of an oversized borehole length was evaluated in a case study with multiple boreholes.

Marcotte et al. (2010) examined the effects of axial heat conduction in boreholes comparing results obtained from the finite and infinite line source solutions. Presenting simulation results for an unbalanced annual load, two cases with different ratio of borehole spacing over borehole length were studied. One of the main conclusion is that the greater this ratio, the more significant the axial effects are while determining the total number of boreholes required in a bore field.

Beier (2011) proposed an analytical model of the actual vertical temperature profile in a GHE for the late-time period of an in-situ test. With this method, one can estimate the ground thermal conductivity as well as the borehole thermal resistance without using the usual average fluid temperature approximation. A sensitivity study based on the vertical fluid temperature profile model has been carried out which shows the errors associated with making the mean fluid temperature approximation assumption while estimating the borehole resistance. Their research proposes to use the *p*-linear average method of Marcotte and Pasquier (2008) over the usual mean temperature approximation.

Du and Chen (2011) also proposed the use of a *p*-linear dimensionless fluid temperature to estimate the steady-state fluid temperature and the borehole thermal resistance. Comparison with results from a quasi-three-dimensional model for single and double U-tube boreholes lead to suggested *p* values for the proper estimation of the thermal resistance.

Beier et al. (2011) constructed an 18 m long laboratory sandbox filled with saturated sand to generate reference data sets for a single U-tube borehole under controlled conditions. An aluminum tube is used as the borehole wall. The inside is filled with a grout and includes a HDPE U-tube with spacers. Much like the experimental set-up used in the present work, they measured sand temperatures at several locations including the borehole wall. Thermistors are installed in

the sand on the horizontal plane that runs through the centerline of the U-tube, all on the inlet side. Two other thermistors measure the inlet-outlet fluid temperatures. A thermal response test was carried out with a steady heat input to determine the ground thermal conductivity as well as the borehole thermal resistance

Recently, Claesson and Hellström (2011) revised and expanded the multipole method to evaluate the steady state heat transfer between a set of arbitrarily positioned circular pipes inside a composite cylindrical region. The proposed method calculates the local thermal resistances between the working fluid in the borehole and the ground in the immediate vicinity of the borehole. The classic Multipole method is improved by replacing the constant temperature condition at a circle outside the borehole by an average radial temperature. In fact, averaged temperature is prescribed at the borehole wall as the outer boundary condition. Also, instead of starting the analysis with prescribed fluid temperatures, prescribed heat fluxes are implemented.

Pasquier and Marcotte (2012) improved the thermal resistance capacity model (TRCM) of Bauer et al. (2011) to integrate the thermal capacities of the working fluid and the pipe. Comparison is done between their proposed approach against a numerical model (which does not account for the fluid thermal capacity). Good agreement between the two models at short and late simulation times is achieved. However, the comparison is not as good for intermediate times. It should be mentioned that the fluid temperature of the inlet and outlet pipes are assumed to be constant over time.

CHAPTER 2 THERMAL CAPACITY EFFECTS IN BOREHOLE GROUND HEAT EXCHANGERS

2.1 Introduction

This chapter reproduces the content of a journal article submitted to Energy and Buildings (Salim Shirazi and Bernier, 2012). The review presented in section 2.3 complements the literature review presented in Chapter 1.

In this article, a one-dimensional transient borehole model is proposed to account for fluid and grout thermal capacities in borehole ground heat exchangers with the objective of predicting the outlet fluid temperature for varying inlet temperature and flow rate. The standard two-pipe configuration is replaced with an equivalent geometry consisting of a single pipe and a cylinder core filled with grout. Transient radial heat transfer in the grout is solved numerically while the ground outside the borehole is treated analytically using the cylindrical heat source method. The proposed model is validated successfully against analytical solutions and experimental results.

For a typical two-pipe configuration, it is shown that the fluid outlet temperature predicted with and without borehole thermal capacity differ by 1.4, 0.35, and 0.23 °C after 0.1, 0.2 and 1 hour, respectively. Annual simulations are also performed over an entire heating season (5600 hours) with a 6 minute time step. Results show that the outlet fluid temperature is always higher when borehole thermal capacity is included. Furthermore, the difference in fluid outlet temperature prediction with and without borehole thermal capacity increases when the heat pump operates infrequently. The end result is that the annual COP predicted is approximately 4.5% higher when borehole thermal capacity is included.

2.2 Problem statement

Closed-loop ground coupled heat pump systems rely on ground heat exchangers (GHE) to reject or extract heat from the ground. A schematic representation of such a heat exchanger is shown in Figure 2.1. It consists of a borehole in which a U-tube pipe is inserted. The borehole is usually filled with a grout to enhance heat transfer and protect underground aquifers. In general, the depth of the borehole (L) is approximately 100 m (328 ft) and its diameter is usually in the 10-15 cm range (4 to 6 inches). High density polyethylene (HDPE) pipes are typically used for the U-

tubes. The inside diameter of these pipes is approximately 25 mm (1 inch). The center-to-center distance between these pipes varies from cases where the pipes are touching each other in the center of the borehole to cases where the pipes are touching the borehole wall on opposite sides. These two cases are often referred to as the A and C configurations (Remund (1999)). In the B configuration (shown in Figure 2.1), the pipes are equally distanced from each other and from the borehole wall.

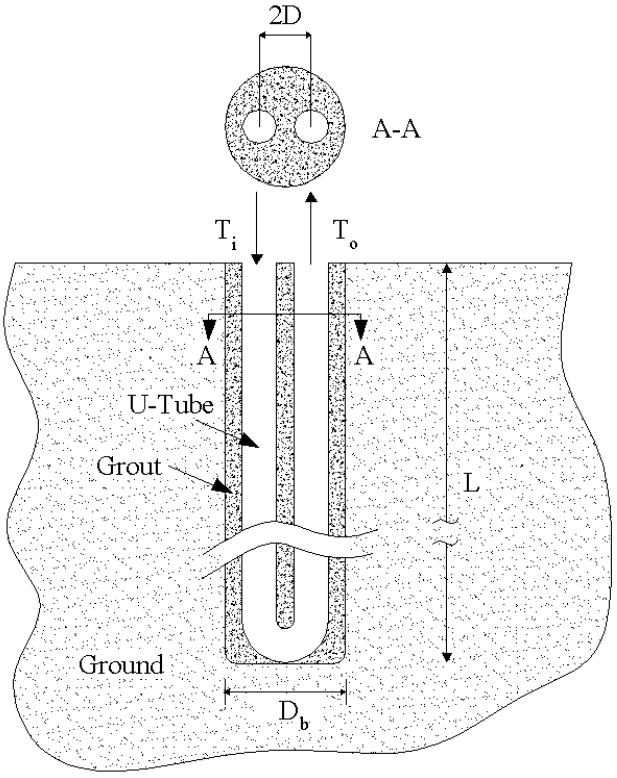

Figure 2.1: Schematic representation of a typical single U-tube ground heat exchanger

Heat is transferred from the fluid circulating in the pipes to the ground. The borehole can experience a variety of flow rates ranging from no flow to full flow conditions and any flow in between if the system is equipped with a variable flow pumping system. At full flow, the residence time, i.e., the time required for the fluid to travel from the inlet to the outlet, is of the order of a few minutes. The difference between the inlet (T_i) and outlet (T_o) temperatures is typically around 5 ºC (9 ºF). Inlet conditions (either temperature or flow) variations do not lead to instantaneous changes in the outlet conditions. This is due to two main reasons. First, the

residence time of the fluid in the borehole induces a delay. Second, any changes at the inlet are dampened by the fluid and grout thermal capacities.

Ground heat exchangers can be modeled in two distinct regions: from the fluid to the borehole wall, and from the borehole wall to the far field. Ground models have been the subject of many investigations including a comparison exercise (Bernier et al. (2007)). The present study concentrates on the inside of the borehole. A one-dimensional transient borehole model is proposed to account for fluid and grout thermal capacities. The objective is to accurately predict the outlet fluid temperature for varying inlet conditions so that borehole thermal capacity can be accounted for in energy simulation programs. The borehole model is coupled here to a ground model which is based on the cylindrical heat source method.

2.3 Review of previous studies

Some of the important pioneering works can be attributed to Eskilson (1987) and Hellström (1991). Using spatial superposition, Hellström developed a 3-D simulation model for borehole thermal energy storage systems. The model was implemented in the TRNSYS (2006) simulation program by Hellström el al. (1996). However, the thermal capacity of the borehole is not included in the model. When there is flow in the borehole, the fluid temperature is evaluated using the borehole wall temperature and a steady-state thermal resistance. For no flow conditions, the fluid temperature is set equal to the borehole wall temperature.

Eskilson's model calculates the average borehole temperature in a bore field using numerically generated *g-functions*. It is important to note that the borehole thermal capacity is not accounted for in the original *g-functions* and that heat transfer to the ground is applied at the borehole wall. Therefore, if only the heat transfer rate in the fluid is known, then one has to evaluate the time it takes for a heat impulse in the fluid to reach steady-state at the borehole wall in order to properly use *g-functions*. This time has been evaluated by Eskilson to be equal to $t_b = 5r_b^2/\alpha_g$, where r_b is the borehole radius and α_g is the thermal diffusivity of the grout material. For typical boreholes, t_b is of the order of 3 to 6 hours (Yavuzturk and Spitler (1999)).

Wetter and Huber (1997) modeled the transient behavior of a single borehole with a double U-tube configuration. This model was implemented in TRNSYS as Type 451. It accounts for grout thermal capacity as well as fluid thermal capacity. In the radial direction, heat transfer is

simulated numerically from the borehole center up to a distance of two meters where the boundary temperature is evaluated using Kelvin's line-source solution. The four-pipe geometry is transformed into a single pipe of equivalent diameter centrally located in the borehole. The grid spacing is non-uniform in the radial direction with one grid point located in the equivalent annulus representing the grout. In the axial direction, the computational domain is subdivided into several ground layers. The fluid temperature is calculated numerically in each of these layers using a transient energy balance.

Rottmayer et al. (1997) proposed a finite difference model to simulate a vertical ground heat exchanger. The model combines the borehole as well as the adjacent ground. It solves the three-dimensional transient problem using the explicit finite difference approach in cylindrical coordinates. The thermal capacity of the fluid is taken into account but it is assumed that pipe and grout thermal capacities can be neglected. The authors justify the use of this assumption by claiming that "the thermal energy change of the grout over a year is on the order of 0.5% of the total heat flow, and thus the wall and grout capacitances are not significant in annual simulations".

Gu and O'Neal (1998) developed an analytical solution to obtain the transient temperature response in a composite media (grout and surrounding ground). Using an equivalent pipe diameter, the governing one-dimensional radial equation is solved using a generalized orthogonal expansion technique to obtain a solution that applies to both the grout and the surrounding ground. Results obtained with their approach compare favorably with experimental results obtained on a small-scale borehole.

Shonder and Beck (1999) developed a radial one-dimensional transient model with the objective of estimating ground and grout thermal conductivities from experimental data obtained on a horizontal test rig. The model lumps the inlet and outlet pipes into a single pipe with an effective radius and adds a film at the outer surface of the pipe. This film has an effective heat capacity to model the fluid and grout thermal capacities. The resulting mathematical model is used in conjunction with a parameter estimation technique to derive values of soil and grout thermal conductivity from experimental data. After 30 hours, the predicted ground thermal conductivity is in excellent agreement with the measured value. The estimated grout thermal conductivity is compared to a range of acceptable values as the actual value is not known. Calculations

performed for two different equivalent pipe radii show that the method is relatively insensitive to the choice of the equivalent pipe radius.

Yavuzturk and Spitler (1999) and Yavuzturk et al. (1999) extended Eskilson's work so that *g-functions* could be used for short time periods. The short-time *g-functions* are derived from two-dimensional numerical simulations (radial and azimuthal) of the borehole, including the grout capacity, and neighboring ground. A "pie sector" approximation is used to model the U-tube geometry. The numerical model is applied to a step pulse for a given borehole geometry and known ground thermal properties. The resulting average transient borehole temperatures are calculated and converted to short-time *g-functions*.

Recently, Yavuzturk et al. (2009) proposed to improve the model of Yavuzturk and Spitler (1999) to include the borehole thermal capacity (fluid and grout). The steady-state thermal resistance for single U-tube boreholes proposed by Liu and Hellström (2006) is first evaluated. Then, the two-pipe geometry is replaced by an equivalent single pipe diameter centered in the borehole. The thermal resistance from the equivalent diameter to the borehole wall is the same as the one determined for the two-pipe geometry. A finite element model is developed to calculate numerically transient effects in the grout. The transient borehole thermal response is coupled to a short time step ground response model through an iterative procedure. The coupling is performed at the borehole wall. Their model is reported to be validated with success with analytical solutions and with field data from a thermal conductivity test. However, their model is only used for a constant step change in the inlet fluid conditions at the borehole.

An analytical approach, based on the "buried cable" solution given by Carslaw and Jaeger (1947), is proposed by Young (2001) to evaluate the short time response of boreholes. The electrical cable consists of a current carrying core separated from a metal sheath by insulation which acts as a thermal contact resistance. By analogy, Young replaced the core with the working fluid, the metal sheath with the grout. The contact resistance represents the steady state borehole thermal resistance which is expressed using the multipole method of Bennet et al. (1987). To improve the accuracy of the model, Young considered moving a part of the grout thermal capacity from the outside of the thermal resistance to the inside by introducing a grout allocation factor. The total thermal mass of the working fluid is taken into account by introducing a fluid multiplication factor. This includes the thermal mass of the fluid inside the U-tube as well as in

the building distribution piping system. Their proposed approach was validated successfully using an in-house two-dimensional (radial and azimuthal) code.

Sutton et al. (2002) introduced a grout time constant to account for the grout thermal capacity in a borehole. It is defined as the time at which the transient response of the borehole, expressed by a transient borehole resistance, reaches the corresponding steady state resistance. The transient borehole resistance is obtained using a transient cylindrical source response which is solved using a technique presented by Hellström (1991) based on the numerical inversion technique first proposed by Veillon (1972). The effects of grout thermal capacity are, however, not specifically presented. Furthermore, the fluid thermal capacity is not taken into account.

Xu and Spitler (2006) found it necessary to modify the short-time step *g-function* generation of Yavuzturk and Spitler (1999) to account for variable film coefficients inside the pipes and for the thermal mass of the fluid in the borehole. The short time-step *g-functions* are generated with a one-dimensional numerical model which approximates the two-dimensional geometry. The so-called multipole method is used to calibrate the thermal resistance of the 1-D model so that it matches the total borehole thermal resistance of the 2-D borehole configuration. An equivalent thermal conductivity which combines the grout and the tube thermal conductivity is used in the 1-D model. Their approach is then validated against a boundary-fitted coordinates 2-D finite volume model. The authors introduced a so-called fluid factor to account for the thermal mass of the fluid outside the borehole in the building loop.

Lamarche and Beauchamp (2007) analyzed the short-time transient thermal response of ground heat exchangers including grout thermal capacity effects. They provide analytical solutions, based on Laplace transforms, to radial heat transfer in composite cylinders. Solutions were obtained for constant heat flux and convection boundary conditions on the inner cylinder. The two-pipe configuration was transformed into an equivalent radius using the approach suggested by Sutton et al. (2002) with the borehole resistance proposed by Hellström (1991). The pipe and fluid thermal capacities are not included in their analysis. Their proposed analytical approach was compared to results from COMSOL numerical simulations and the buried cable approach proposed by Young (2001). This comparison shows that their proposed approach is in good agreement with the COMSOL solutions. However, the comparison with the buried cable

approach is not as good. This might be due to the fact that grout allocation and fluid multiplication factors were not considered.

He et al. (2009, 2011) presented a three-dimensional numerical model of a borehole, based on the finite-volume solver known as General Elliptical Multi-block Solver(GEMS3D) to simulate fluid transport along the U-tube as well as transient heat transfer in and around a GHE. Simulation results are compared with those of a two-dimensional model. By applying step changes in borehole inlet parameters, simulation results show the importance of the delayed response associated with the fluid transport along the U-tube. This effect is important when a system is operating at peak load or during the On-Off cyclic operation of the heat pump. Unlike their proposed numerical model, their two- dimensional model showed an instant response to the inlet step changes, indicating some of the shortcomings associated with two-dimensional models.

Applying state model reduction techniques, Kim et al. (2010) proposed a new reduced model (RM) for GHEs. The model can handle the rapid heat transfer phenomenon inside the borehole as well the slow processes occurring outside the borehole. The ground surrounding the GHE is divided into several slices in the vertical direction and each slice is decomposed into several sub-domains in the radial direction each of which can have a different time step. The RM approach is compared against two TRNSYS types: TYPE-451, a double U-tube GHE model accounting for grout and fluid capacity, and the DST, which does not take into account the grout thermal capacity. The RM and TYPE 451 gave almost the same annual average COP while there was a 2.5% difference between the RM and DST models, with the RM model giving higher COPs. In a related article, Kim et al. (2010) verified the numerically-based RM model against analytical solutions from the literature. The authors show that it is possible to obtain accurate results by using only 6% of the original nodes with a resulting computation time reduced by 95% compared to a complete model.

Yang et al. (2010) presented a detailed literature review of models and systems for vertical borehole systems. The review gives a brief analysis of the 1D, 2D, and 3D approaches to model borehole heat transfer. For one-dimensional models, the equivalent diameter with negligible thermal capacity approach is reviewed and it is concluded that it is inadequate to evaluate the dynamic response of boreholes as well as thermal short-circuiting between the U-tube legs. The Hellström relationships are presented for the two-dimensional case. When the fluid temperatures

in both pipes are assumed equal (assumption attributed to Eskilson), the borehole thermal resistance calculations are simplified but thermal short-circuiting cannot be accounted for. Finally, the quasi 3-D model of Zeng et al. (2003) is presented.

Using the well-known delta-circuit model, Bauer et al. (2011) developed two-dimensional thermal resistance and capacity models (called TRCMs) for symmetrically positioned coaxial, single and double U-tube borehole configurations. The capacity of the grouting material is taken into account with one capacity per tube while the borehole is divided into two zones for single U-tube and four zones for double U-tube GHEs. For double U-tube GHEs, the thermal resistances are calculated using the multipole method. These models are compared against two-dimensional fully discretized finite- element models as well as the delta-circuit model (which does not account for the borehole thermal capacity). Good agreement was achieved after the first fifteen minutes of the simulation. It should be noted that the thermal capacities of the fluid and pipes are not taken into account.

In summary, the literature review shows that most borehole models are steady-state models which neglect the thermal capacity of the borehole. While the assumption of a steady-state thermal resistance might be acceptable when the heat pump operates continuously, it is questionable when heat pumps undergo on/off cycles to meet the building load. It is also clear from this review that there is a need to quantify the effect of borehole thermal capacity on heat pump annual coefficient of performance. This chapter proposes to examine these two issues with a relatively simple approach using a one-dimensional model based on an equivalent geometry. The impact of a step change in inlet conditions is first examined and then annual simulations with and without borehole capacity are performed.

This review also reveals the lack of existing credible experimental data obtained under controlled conditions for validating ground heat exchanger models. An experimental apparatus is designed, constructed, instrumented and commissioned and is presented in Chapter 4.

2.4 Proposed model

The following analysis is based on the assumption that the essence of transient heat transfer in boreholes can be captured by replacing the U-tube, two-pipe geometry, by a grout-filled cylinder delimited by an inside equivalent diameter (to be defined shortly) and the real borehole diameter.

The transformation of the geometry is illustrated in Figure 2.2 and 2.3. The resulting one-dimensional approximation neglects the axial (along the length of the borehole) and azimuthal (along the circumference) variations and only considers radial variations. Even though this approach does not provide the fine details that a 3-D transient model would give, it has the advantage of being computationally less intensive which enables inclusion of borehole (fluid and grout) thermal capacities in annual energy simulations.

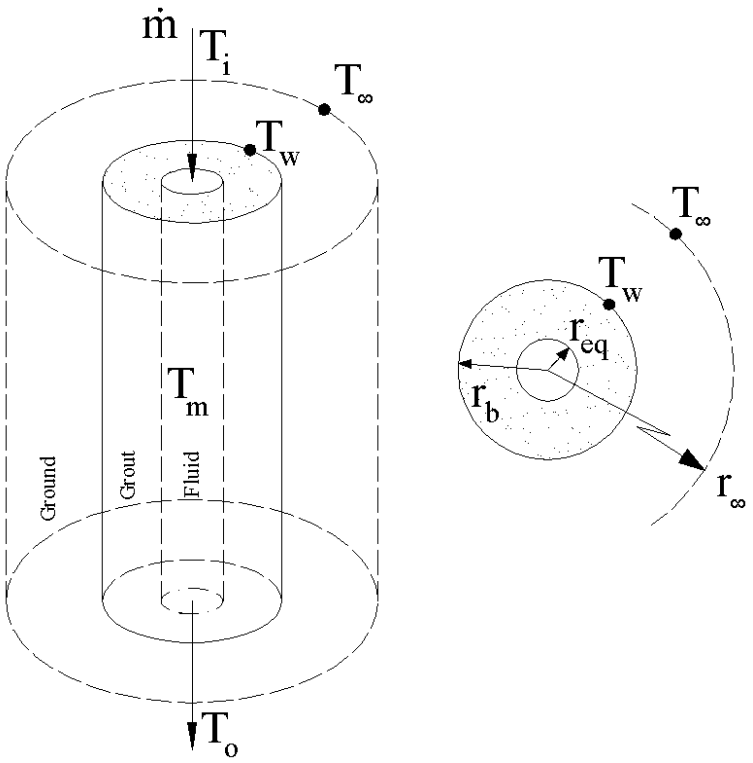

Figure 2.2: Representation of the transformation from a two-pipe geometry (Figure 2.1) to an equivalent single pipe.

The objective is to predict the outlet fluid temperature for a given set of transient fluid temperatures and flow rates at the borehole inlet. Transient radial heat transfer in the cylinder core (consisting of the grout and the working fluid) is solved numerically while the ground outside the borehole is treated analytically using the cylindrical heat source method. These two models are coupled through the heat flux and temperature at the borehole diameter. The temperature variation in the fluid is obtained from an energy balance. Since the fluid temperature is unknown a priori, an iterative procedure is used to obtain the outlet fluid temperature**.**

2.4.1 Equivalent diameter approximation

As shown in Figure 2.3, the standard U-tube borehole is approximated by a core cylinder with an equivalent inside diameter and an outside diameter corresponding to the real borehole diameter. The thermal capacity of the HDPE pipes is neglected. The comparison presented in Table 2.1 shows that this assumption is justified as the grout thermal capacity is usually much higher than the pipe thermal capacity.

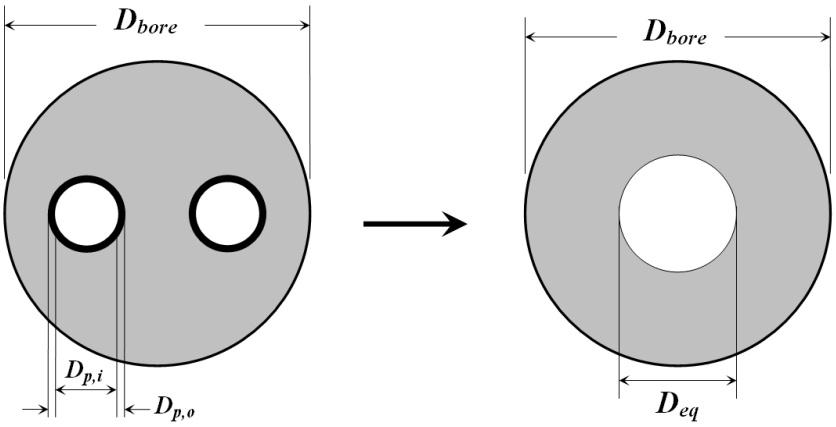

Figure 2.3: Approximation of the real geometry with an equivalent cylinder with an equivalent inside diameter.

Table 2.1: Comparison between pipe and grout thermal capacities in typical boreholes.

Pipe size and type	Thermal capacity per unit length of borehole ($J \cdot m^{-1} \cdot K^{-1}$)		Thermal capacity ratio (-)
SDR-11 HDPE pipes	Pipe	Grout	Grout/Pipe
19 mm (3/4")	325	64600	199
25 mm (1")	505	62100	123
30 mm (1 1/4")	815	58000	71

Based on:

Two SDR-11 pipes (1 U-tube)

Borehole diameter = 0.15 m (6 inches)

Volumetric heat capacities for pipe and grout: 1.77 and 3.9 $MJ \cdot m^{-3} \cdot K^{-1}$, respectively

The equivalent pipe diameter, D_{eq}, is based on the steady-state borehole thermal resistance, $R_{b,ss}$ of Hellström (1991):

$$R_{b,ss} = \frac{1}{4\pi k_{gt}}\left[\ln\left(\frac{r_b}{r_p}\right) + \ln\left(\frac{r_b}{2D}\right) + \sigma \ln\left(\frac{r_b^4}{r_b^4 - D^4}\right)\right] + \frac{1}{2}R_p$$

where: (2.1)

$$\sigma = \left(\frac{k_{gt} - k_{gr}}{k_{gt} + k_{gr}}\right),\ R_p = \frac{\ln(D_{p,o}/D_{p,i})}{2\pi k_p}$$

where D is half the center-to-center distance between the two legs of the U-tube, k_{gr} and k_{gt} are the ground and grout thermal conductivities, r_b is the borehole radius, r_p (=$D_{p,o}$ /2) is the pipe radius, and R_p is the pipe thermal resistance. The equivalent diameter is obtained by equating the steady-state borehole thermal resistance for the real geometry, $R_{b,ss}$, to the thermal resistance of the equivalent cylinder:

$$R_{b,ss} = \frac{\ln(D_b / D_{eq})}{2\pi k_{gt}} \tag{2.2}$$

where D_b is the borehole diameter. Solving for the equivalent pipe diameter D_{eq}, one obtains:

$$D_{eq} = D_b e^{-2\pi k_{gt} R_{b,ss}} \tag{2.3}$$

In order to account for possible flow rate variations during simulations, the thermal resistance associated with the internal film coefficient, which is not included in $R_{b,ss}$ is calculated separately and added to $R_{b,ss}$.

The transformation from a U-tube geometry to an equivalent cylinder has repercussions on the fluid velocity in the borehole and the internal film coefficient. Modifications are therefore necessary in the equivalent geometry to maintain identical heat transfer in both geometries. The first of these modifications concerns the equivalent internal film coefficient, h_{eq}, which is given by:

$$h_{eq} = \left(2\frac{D_{p,i}}{D_{eq}}\right)h \tag{2.4}$$

where h is the internal film coefficient of the U-tube configuration. This value can be obtained from standard correlations such as the ones given by Holman (2002). The residence time of the fluid in the GHE, t_{res}, corresponds to the time required for the fluid to travel from the inlet to the outlet. For the U-tube configuration, t_{res} is given by:

$$t_{res} = \rho_f A \frac{2L}{\dot{m}} \tag{2.5}$$

where ρ_f is the fluid density, A is the cross-sectional area of the U-tube pipe ($=\pi D_{p,i}^2/4$), and $\dot{m}$ is the mass flow rate. For the equivalent cylinder, the residence time is:

$$\left(t_{res}\right)_{eq} = \rho_{f,eq} A_{eq} \frac{L}{\dot{m}} \tag{2.6}$$

where "$_{eq}$" refer to the equivalent cylinder geometry and A_{eq} is the cross-sectional area of the equivalent cylinder ($=\pi D_{eq}^2/4$). The mass flow rates and residence times have to be identical in both the real and equivalent geometries which imply that the fluid density ($\rho_{f,eq}$) and velocity (u_{eq}) in the equivalent cylinder are equal to:

$$\rho_{f,eq} = 2\rho_f \left(\frac{D_{p,i}}{D_{eq}}\right)^2 \tag{2.7}$$

$$u_{eq} = \left(\frac{\rho_f}{\rho_{f,eq}}\right)\left(\frac{D_{p,i}}{D_{eq}}\right)^2 u \tag{2.8}$$

where u is the fluid velocity in the U-tube configuration.

From Equations (2.7) and (2.8), one can conclude:

$$u_{eq} = 0.5u \tag{2.9}$$

Finally, the total fluid thermal capacity inside the equivalent pipe has to be identical to that of the real geometry. This leads to:

$$c_{f,eq} = 2\left(\frac{D_{p,i}}{D_{eq}}\right)^2 \left(\frac{\rho_f}{\rho_{f,eq}}\right) c_f \tag{2.10}$$

where c_f and $c_{f,eq}$ are the specific heat capacities of the fluid in the U-tube geometry and in the equivalent pipe, respectively. From Equations (2.7) and (2.10) one can write:

$$c_{f,eq} = c_f \tag{2.11}$$

To summarize, based on the known characteristics of the U-tube geometry (i.e., D_b, k_{gt} , $D_{p,i}$, L) and the operating conditions (i.e., h, $\dot{m}$, ρ_f , c_f), Equations (2.3), (2.4), (2.7), (2.9) and (2.11) are used to obtain the corresponding values for the equivalent geometry.

2.4.2 Transient heat transfer in the borehole

Transient heat transfer in the equivalent geometry is solved numerically. The problem is governed by the unsteady one-dimensional energy equation in cylindrical coordinates:

$$\rho_{gt} c_{p_{gt}} \frac{\partial T}{\partial t} = k_{gt} \frac{1}{r} \frac{\partial}{\partial r}\left(r \frac{\partial T}{\partial r} \right) \tag{2.12}$$

where the subscript "*gt*" refers to grout properties which are assumed to be constant. Figure 2.4 presents the extent of the calculation domain.

Equation(2.12) is subjected to the following boundary conditions:

$$\begin{aligned} & T = T_w(t) \quad \text{at} \quad r = r_b \\ & -2\pi r_{eq} k_{gt} \left. \frac{\partial T}{\partial r} \right|_{r=r_{eq}} = q'(t) \\ & q'(t) = 2\pi r_{eq} h_{eq} (T_{r_{eq}} - T_m) \end{aligned} \tag{2.13}$$

where r_{eq} is the equivalent radius (=$D_{eq}/2$), $T_{r_{eq}}$ is the temperature at the equivalent radius, and T_m is the mean fluid temperature in the borehole (= (T_{in} + T_{out})/2). The whole domain is assumed to be at the undisturbed ground temperature, T_∞ at t = 0.

The problem is solved using the control volume-based finite difference method of Patankar (1980) with the fully implicit approach. Using the nomenclature presented in Figure 2.4, the discretized equation for an internal node *P* is given by:

$$a_P T_p = a_N T_N + a_S T_S + b \tag{2.14}$$

where the coefficients are:

$$a_N = \frac{r_n k_{gt,n}}{(\delta r)_n} \quad , \quad a_S = \frac{r_s k_{gt,s}}{(\delta r)_s}$$

$$a_P^0 = \frac{\rho_{gt} c_{gt}}{2\Delta t}\left(r_n^2 - r_s^2\right) \ , \ b = a_P^0 T_P^0 \qquad (2.15)$$

$$a_P = a_P^0 + a_N + a_S$$

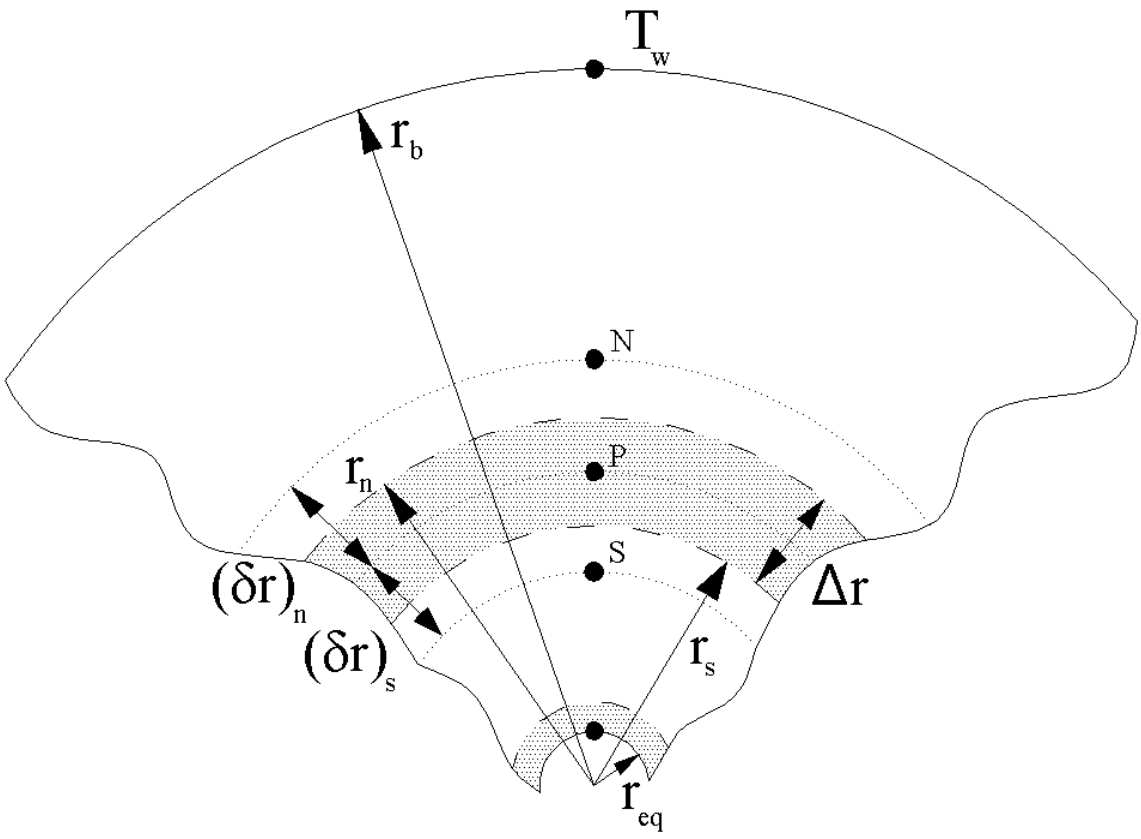

Figure 2.4: Schematic of the grids in the radial direction

The superscript " ^{0} " refers to conditions at the previous time step and Δt is the time step. The first node is located on the interior wall in a half control volume. For this particular node, the discretized equation for the temperature at r_{eq}, $T_{r_{eq}}$ is given by:

$$a_P T_{r_{eq}} = a_N T_N + b$$

where:

$$a_N = \frac{r_n k_{gt,n}}{(\delta r)_n} \quad , \quad a_P^0 = \frac{\rho_{gt} c_{gt}}{2\Delta t}\left(r_n^2 - r_{eq}^2\right) \tag{2.16}$$

$$a_P = a_P^0 + a_N \quad , \quad b = a_P^0 T_{r_{eq}}^0 + r_{eq} q''_{r_{eq}}$$

In Equation (2.16) when heat is transferred from the fluid to the pipe, one can write: $q''_{r_{eq}} = h_{eq}\left(T_m - T_{r_{eq}}\right)$.

A non-uniform grid structure, based on Anderson's (1996) approach, is used with a resulting concentration of grid points near steep temperature gradients. Time and grid independence checks are reported in Appendix A. The results of these checks indicate that 10 grid points are needed in the core cylinder and that the time step should be approximately equal to *RT*/20 (where *RT* is the residence time) in order to obtain a solution that is independent of the time step and grid spacing.

2.4.3 Treatment of the fluid thermal capacity

2.4.3.1 Flow in the borehole

The one-dimensional approach assumed in the proposed model implies that fluid axial conduction is neglected and that the mean fluid temperature, T_m, is uniform over the full length of the borehole during a given time step. Based on these assumptions, and assuming constant fluid thermal properties, a transient energy balance on the fluid volume in the borehole yields:

$$\dot{m} c_{f,eq}\left(T_i - T_o\right) - h_{eq} A_{eq}\left(T_m - T_{r_{eq}}\right) = \left(\rho_{f,eq} c_{f,eq} V_{eq}\right) \frac{dT_m}{dt} \tag{2.17}$$

where V_{eq} is the volume occupied by the fluid in the borehole. Discretizing Equation (2.17) using the implicit approach gives:

$$\dot{m} c_{f,eq}\left(T_i - T_o\right) - 2\pi r_{eq} L h_{eq}\left(T_m - T_{r_{eq}}\right) = \frac{\left(\rho_{f,eq} c_{f,eq}\right)\pi r_{eq}^2 L}{RT}\left(T_m - T_m^0\right)$$

where: (2.18)

$$T_m = \frac{T_i + T_o}{2}$$

Equation (2.18) states the net energy entering the control volume by advection minus the energy leaving it by convection is equal to the fluid internal energy variation over a certain period of time, which in this case is the fluid residence time, *RT*. On the left hand side of Equation (2.18) all temperatures are evaluated at the current time step while on the right hand side, T_m^0 is the mean fluid temperature prevailing during the previous time step.

Substituting for T_m^0 and rearranging Equation (2.18) to solve for T_o at the current time step, yields:

$$T_o = \frac{1}{B}\left[CT_i + DT_{r_{eq}} + A\left(T_o^0 + T_i^0\right)\right]$$

where:

$$A = \frac{\left(\rho_{f,eq} c_{f,eq}\right)\pi r_{eq}^2 L}{2RT} \qquad (2.19)$$

$$B = \dot{m} c_{f,eq} + \pi r_{eq} L h_{eq} + A_{eq}$$

$$C = \dot{m} c_{f,eq} - \pi r_{eq} L h_{eq} - A_{eq}$$

$$D = 2\pi r_{eq} L h_{eq}$$

2.4.3.2 No flow in the borehole

When there is no flow, Equation (2.18) reduces to:

$$T_m = \frac{ET_m^0 + T_{r_{eq}}}{1+E}$$

where: (2.20)

$$E = \frac{\left(\rho_{f,eq} c_{f,eq}\right) r_{eq}}{2h_{eq} TI}$$

When fluid thermal capacity is neglected, Equation (2.20), reduces to $T_m = T_{req}$. In addition, if the grout thermal capacity is neglected, then T_m and T_{req} are equal to the borehole wall temperature $T_{w.}$ Thus, when there is no flow and the grout and fluid thermal capacities are neglected, the fluid temperature is equal to the borehole wall temperature much like what is done in the DST model (Hellström et al. (1996)).

2.4.4 Heat transfer in the ground

Heat transfer from the borehole wall to the far-field is similar to the heat transfer from a cylinder subjected to a heat flux boundary condition on its inner wall and embedded in an infinite homogeneous medium with a constant far-field temperature, T_∞. This problem has been solved analytically by Carslaw and Jaeger (1947) and is often referred to the cylindrical heat source (CHS) solution. This solution is somewhat complicated and not practical for energy simulations unless pre-calculated curve-fitted relationships (Bernier, 2001 ; Bernier and Salim Shirazi, 2007) or approximations such as the one provided by Cooper (1976) are used. For a constant heat flux boundary condition, the time variation of the borehole wall temperature, $T_{w,t}$, given by the CHS is:

$$T_{w,t} = T_\infty - \frac{q}{L}\frac{G(Fo)}{k_{gr}} \tag{2.21}$$

where, q is the heat transfer rate (a positive "q" value implies heating, i.e., heat transfer from the ground to the fluid), $G(Fo)$ is the solution given by Cooper (1976) for a given Fourier number (Fo) defined as $Fo = \alpha_{gr} t / r_b^2$ where α_{gr} is the ground thermal diffusivity and t is the time.

When performing energy simulations the heat flux will vary. In these cases, the temporal superposition and load aggregation algorithm developed by Bernier et al. (2004) is used. The technique, referred to as “Multiple Load Aggregation Algorithm” or MLAA, uses two major thermal history periods, referred to as “past” and “immediate”. This technique leads to:

$$T_{w,t} = T_\infty - \frac{1}{k_{gr} L}(MLAA) \tag{2.22}$$

where $MLAA$ represents the terms of the Multiple Load Aggregation Algorithm (Bernier et al., 2004).

2.4.5 Solution methodology

The solution flowchart for the proposed model is given in Figure 2.5. As shown in this figure, for each time increment TI, there are two inner iterative loops identified as “numerical borehole model” and “intermediate calculations”. Several temporal variables are used. The Time

Increment (*TI*) is the time difference between two step changes in the inlet conditions. The value of *TI* can vary from a few minutes to one hour in energy simulation programs. The Residence Time, *RT*, given by Equation (2.5), is the time required for the fluid to travel through the ground heat exchanger and is of the order of 2 to 5 minutes in full flow. A number of intermediate calculations (*IT*) are performed during each *TI*. The value of *IT* is equal to the truncated value of the ratio *TI/RT*. During each *RT*, a number of calculations (*NI*) are performed (usually around 20–see Appendix A) in the numerical borehole model. In other words, the time step in the numerical simulations, *dt*, is given by the ratio *RT / NI*.

The main objective of the calculations is the determination of the outlet fluid temperature from the borehole, T_o, for values of T_i and $\dot{m}$ prevailing during a given *TI*. The procedure starts by calculating the equivalent parameters given by equations (2.3), (2.4), (2.7), (2.9) and (2.11). Then, for the current time increment *TI*, T_m^0 and T_w are set equal to their corresponding values at the previous *TI*. The intermediate calculations loop is initiated with a guess value for T_m for the numerical borehole model. Then, $T_{r_{eq}}$ and q_{bore} as well as the nodal temperatures in the equivalent cylinder are determined for each *dt*. At the last *NI* (an amount of time equivalent to *RT* has passed) calculations are performed in the numerical borehole model before passing the values of $T_{r_{eq}}$ and q_{bore} to the intermediate calculations loop.

Values of $T_{r_{eq}}$ and q_{bore} are then used to calculate T_m, T_o and $q_{r_{eq}}$ at a time corresponding to the product $i \times RT$. Then, the recently calculated value of T_m is compared to the guessed value of T_m. If both values do not agree within a certain tolerance, calculations are repeated with a new value of T_m. At convergence, T_m^0 is set to the recent value of T_m and the next intermediate calculation starts. Intermediate calculations proceed until $i=IT$. Then, values of T_o, T_m, $T_{r_{eq}}$, $q_{r_{eq}}$ and q_{bore} at the current *TI* are calculated. Finally, before returning to the next *TI*, T_w is evaluated using Equation (2.22) from the calculated value of q_{bore} at the current *TI*.

Figure 2.6 has been drawn to illustrate the calculation process when coupled to an energy simulation program which uses an hourly time step. As shown on this figure, the inlet temperature to the borehole changes at each hour, starting at 7.11 °C for TI = 88 to 3.64 °C for TI = 91. The values of T_o that are returned to the hourly simulation program are: 7.54, 7.55, 5.67, and 4.56 °C for TI = 88, 89, 90, and 91 respectively. It is to be noted that these values do not

coincide exactly with the end of the time increment. This is due to the fact that the ratio TI/RT is not an integer in this case. The figure shows how the proposed model handles a step change in T_i. This is particularly evident when T_i changes from 7.11 to 4.96 °C at the beginning of 89th hour. Corresponding values of T_o experience a sharp drop at the beginning of the time increment, then T_o stabilizes to reach somewhat of a plateau at 5.67°C. As shown, values of T_o are also available at the end of each residence time (RT).

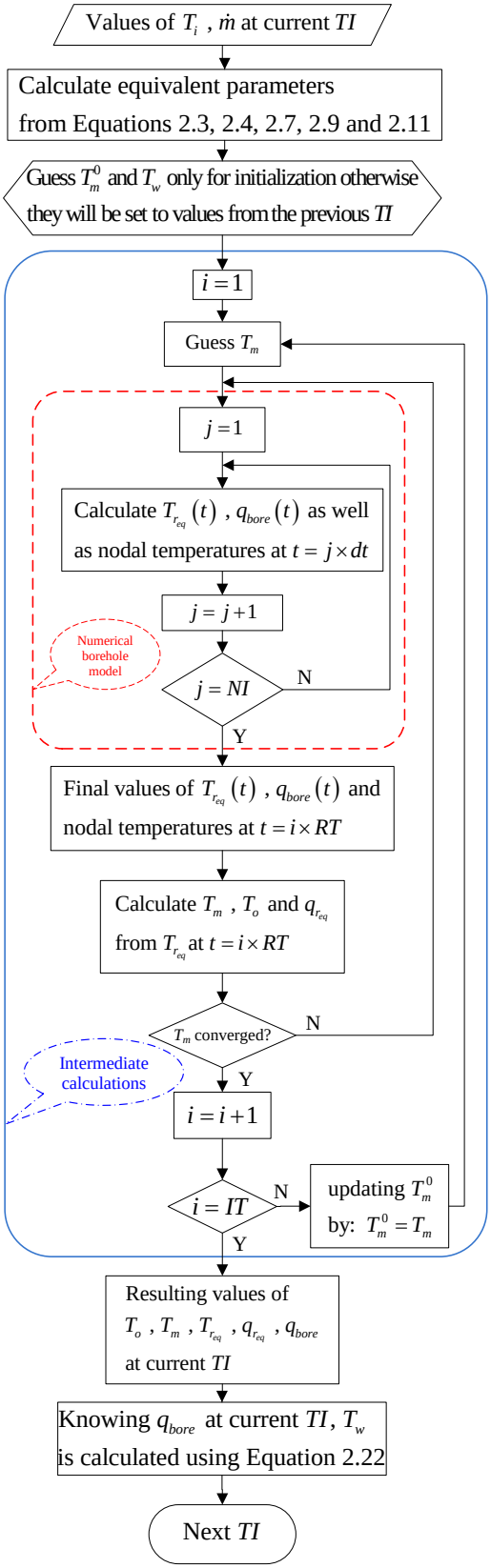

Figure 2.5: Flow chart of the solution procedure.

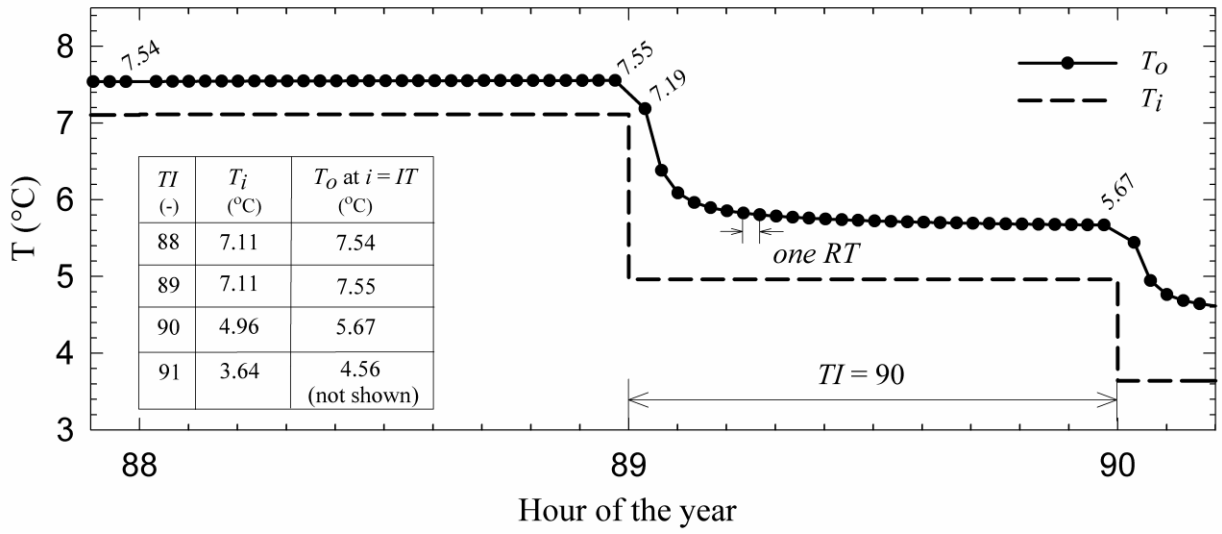

Figure 2.6: Illustration of the calculation process in the proposed model

2.4.6 Verification of the proposed model

In this section the results of the proposed model are compared with results obtained from three sources. First, a comparison is made with analytical solutions of steady state and transient heat transfer in a cylinder then the proposed model is validated with measured field data.

2.4.6.1 Comparison with analytical solutions

The numerical borehole model is first compared with the steady-state solution to heat transfer in a composite cylinder made of three different layers. This solution is presented in Appendix B. Table 2.2 lists the characteristics of each of these layers. Even though the proposed model only requires modeling heat transfer in a one layer cylinder, i.e., in the grout, it was built to handle up to three separate layers and the comparison reported here concerns a case with three layers. The boundary conditions are: i) constant heat flux, $q'' = 100$ W/m^2 at r_0 = 0.022 m; ii) constant temperature of 10 °C at r_3 = 1 m. The initial temperature is set at 10 °C from r = 0.022 to 1 m.

Table 2.2: Characteristics of the composite cylinder used in the verification of the numerical code.

Layer	Inner and outer radii (m)	Thermal conductivity ($W \cdot m^{-1} \cdot K^{-1}$)	Volumetric heat capacity ($MJ \cdot m^{-3} \cdot K^{-1}$)
1	r_0= 0.022 to r_1= 0.025	0.389	1.77
2	r_1= 0.025 to r_2 = 0.075	0.744	3.9
3	r_2=0.075 to r_3= 1.0	2.5	2.5

Figure 2.7 shows the temperature distribution in the calculation domain obtained by the numerical code and the analytical solution. A zoomed portion of the graph (from r =0.02 to 0.08 m) is also provided. The numerical borehole model is solved in transient mode until results reached steady-state. As can be seen in Figure 2.7, the results of the numerical code are in very good agreement with the steady-state analytical solution.

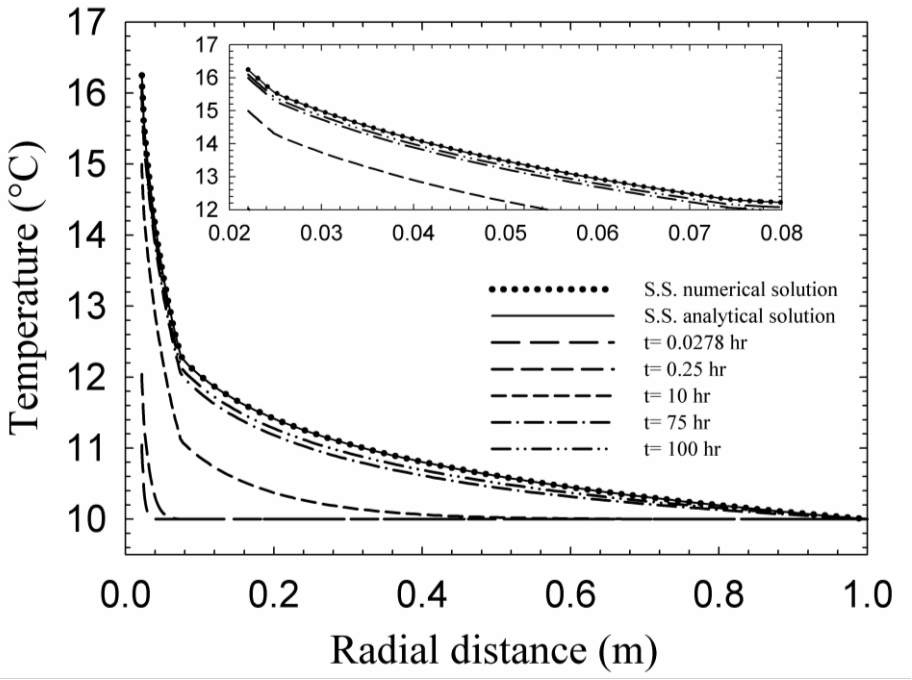

Figure 2.7**:** Comparison of the numerical solution with the steady-state analytical solution to heat transfer in a composite cylinder.

Results from the proposed model are also compared with the analytical solution, provided by Veillon (1972) and Baudoin (1988), to the one-dimensional transient heat transfer in a cylinder subjected to a constant heat transfer rate per unit length on its inner wall and immersed in an infinite medium at a constant far-field temperature (Appendix C). This test case involves the geometry described in Figure 2.2 with identical thermal and physical properties for the grout and ground from r_{eq} to r_{∞}. These properties are given in Table 2.3.

A constant heat transfer rate per unit length of 40.4 W/m is applied at r_{eq}. With a borehole length of 72 m, this corresponds to a heat transfer rate of 2909 W. The initial temperature from r_{eq} to r_{∞} is equal to 10 °C, the far-field temperature.

Table 2.3: Thermal properties and dimensions used for two test cases.

Parameter	Units	Comparison with the transient analytical solution (Figure 2.8)	Comparison with experimental data (Figure 2.9)
$q_{r_{eq}}$		40.4	N/A
L	m	72	74.68
T_{∞}	°C	10	17.3
k_{gt}	$W \cdot m^{-1} \cdot K^{-1}$	0.7443	1.08
k_{gr}	$W \cdot m^{-1} \cdot K^{-1}$	0.7443	2.55
$(\rho c_p)_{gt}$	$MJ \cdot m^{-3} \cdot K^{-1}$	3.9	3.9
$(\rho c_p)_{gr}$	$MJ \cdot m^{-3} \cdot K^{-1}$	3.9	2.11
r_{eq}	m	0.0235	0.0195
r_b	m	0. 057	0.057

The results of this test case are shown in Figure 2.8 where the heat transfer rate at r_b is plotted as a function of time. The results given by the numerical code of the proposed model are in very good agreement with those given by the analytical solution.

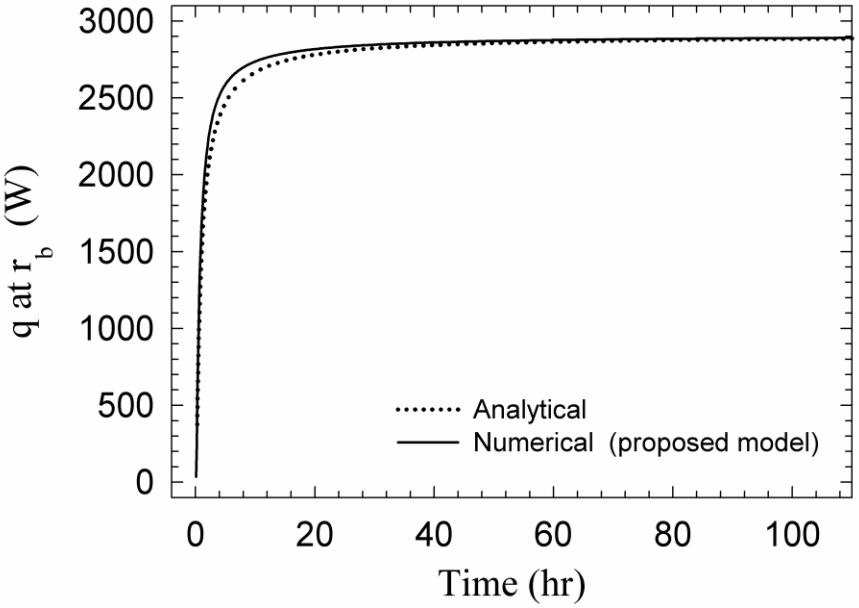

Figure 2.8: Comparison of the numerical solution with the transient analytical solution to heat transfer in a cylinder

2.4.7 Comparison with experiments

Recently, Spitler et al. (2009) performed an inter-model comparison of various ground heat exchanger models using experimental data from a facility located at Oklahoma State University. The data were obtained from three single U-tube boreholes each with a length of 74.68 m and a radius of 0.057 m. These boreholes are used in conjunction with a heat pump. Other relevant parameters are indicated in Table 2.3. Spitler et al. (2009) report a borehole thermal resistance of 0.1622 $m^{-1} \cdot K^{-1} \cdot W$. This value was used as $R_{b,ss}$ (with a proper account for the film coefficient) in Equation (2.3) to obtain the equivalent radius, r_{eq} (= 0.0195 m). Experimental data were gathered over an 18 month period. Results presented in Figure 2.9 are for one particular day, 4585 hours after the start of the test. As shown in Figure 2.9, there is very good agreement between the data and the proposed model with an RMS difference of 0.26°C. The oscillations in temperature, due to the on/off operation of the heat pump, are well reproduced by the proposed model.

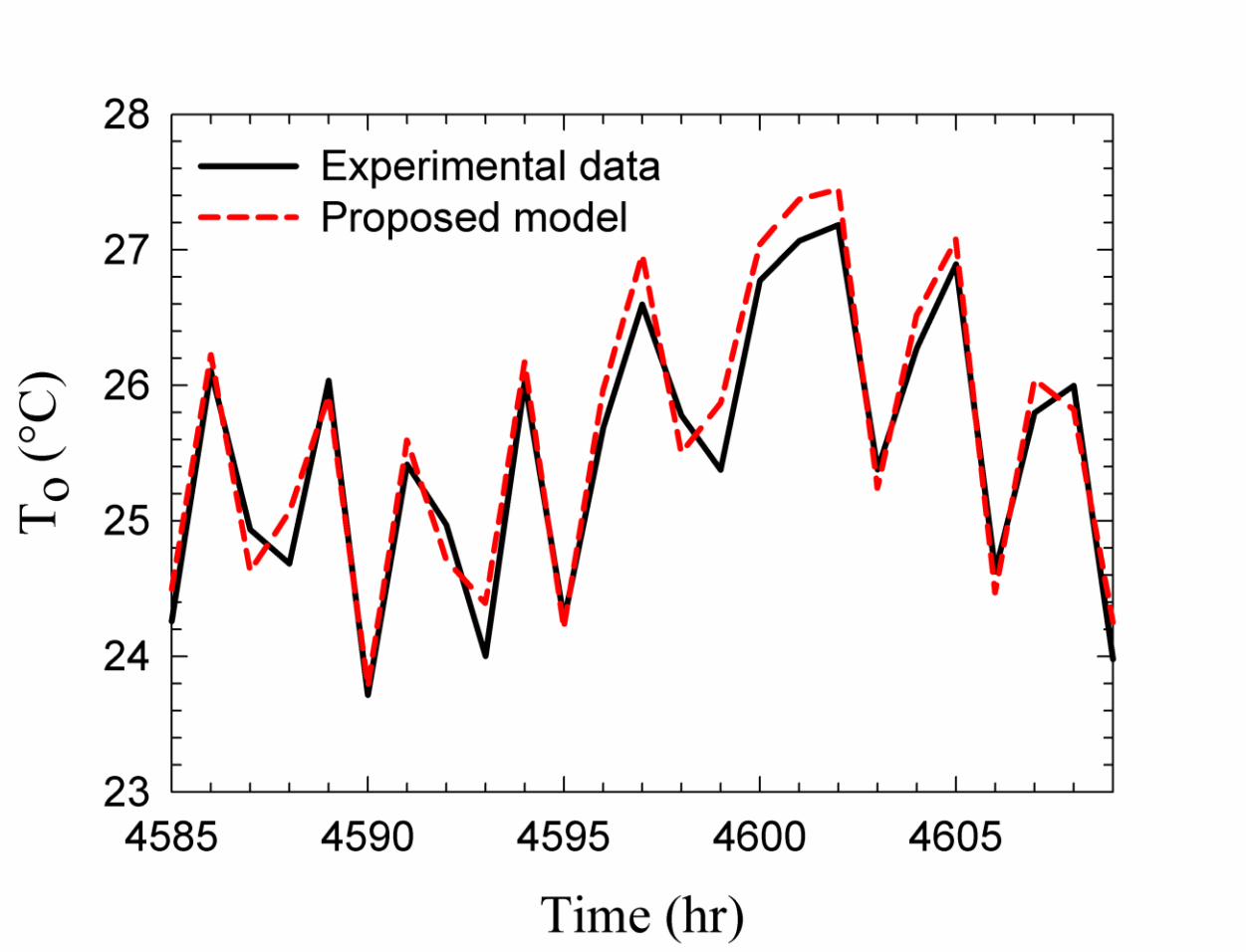

Figure 2.9: Comparison between the proposed model and the experimental data of Spitler et al. (2009).

Based on the three comparisons made in this section, the proposed model can be used with confidence to study borehole thermal capacity effects.

2.5 Applications of the proposed model

In this section, the proposed model is applied to cases of various complexities to show what effect the borehole thermal capacity has on the prediction of ground heat exchanger behavior. The parameters used in each test are given in Table 2.4.

2.5.1 Thermal capacity effects

The first case concerns a comparison among the three typical pipe locations which are often assumed in boreholes. For this test case, the borehole (fluid and grout) and the ground are assumed to be at the same initial temperature, i.e., 12 °C. Then, the inlet temperature is suddenly increased to 40 °C.

Table 2.4: Parameters used in the two test cases of the application section.

Parameter	**Unit**	**Values**	**Annual simulations**
T_∞	°C	12	12
T_i	°C	40	Varying (Figure 2.12)
L	m	75	150
k_{gr}	$W \cdot m^{-1} \cdot K^{-1}$	2.5	2.5
k_{at}	$W \cdot m^{-1} \cdot K^{-1}$	0.74	0.74
$(\rho c_p)_{gr}$	$MJ \cdot m^{-3} \cdot K^{-1}$	2.5	2.5
$(\rho c_p)_{at}$	$MJ \cdot m^{-3} \cdot K^{-1}$	3.9	3.9
D_i	m	0.026	0.026
D_o	m	0.033	0.033
D_b	m	0.15	0.15
$\dot{m}$	$kg \cdot sec^{-1}$	0.664	0.442 (heat pump on) 0.0 (heat pump off)
h	$W \cdot m^{-2} \cdot K^{-1}$	3920	2833 ($\dot{m}$ =0.442) 76 ($\dot{m}$ =0)
h_{eq}	$W \cdot m^{-2} \cdot K^{-1}$	4330	2890 ($\dot{m}$ =0.442) 78 ($\dot{m}$ =0)
TI	sec	360	360
RT	sec	120	360
Pipe		Fig. 2.10: A,B,C	B

The results are shown in Figure 2.10 where the evolution of the outlet temperature is shown for the first 10 hours after the step change. As shown on this figure, the outlet temperature reaches somewhat of a constant value after 10 hours with corresponding outlet temperatures of 37.9, 37.5, and 36.4 °C for configurations A, B, and C, respectively. As expected, configuration C is better, in terms of fluid cooling, than the other two as pipe spacing in configuration C leads to a smaller borehole resistance. Using the left scale in Figure 2.10, it can be seen that the fluid outlet temperature reaches a high percentage of the possible temperature increase in only 0.2 hour after the step change. These percentages are approximately equal to 75%, 87% and 90% for configurations C, B, and A, respectively.

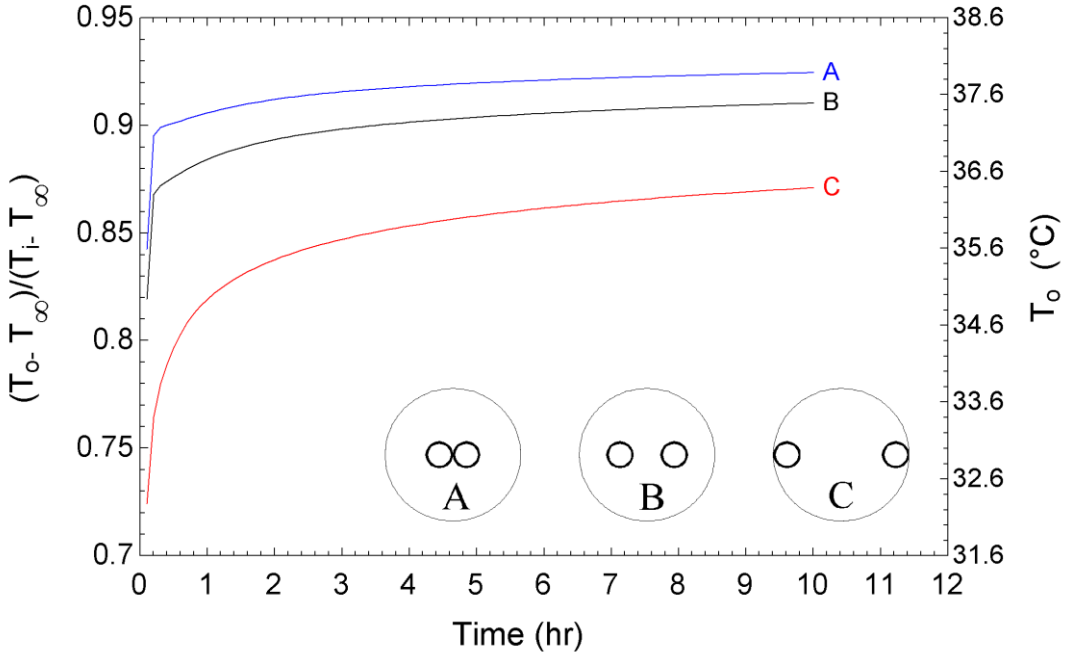

Figure 2.10: Transient behavior of three standard pipe configurations following a step change in inlet temperature.

Figure 2.11 shows the difference in outlet fluid temperature with ($T_{0,W\text{-}TC}$) and without ($T_{0,WO\text{-}TC}$) borehole thermal capacity (grout and fluid) for the B configuration (the curve identified as W-TC corresponds to the B curve in Figure 2.10). The left scale shows the non-dimensional outlet temperature while the right scale presents the non-dimensional temperature difference between the outlet temperatures without and with thermal capacity. As shown on this figure, thermal

capacity effects are significant only in the first few hours after a step change. After that period, the difference becomes negligible. As indicated on the bottom curve, for the case where T_i = 40 °C (with an initial temperature of 12 °C), the differences in outlet temperatures without and with thermal capacity ($T_{0,W0\text{-}TC}$ - $T_{0,W\text{-}TC}$) are 1.4, 0.35, and 0.23 °C after 0.1, 0.2 and 1 hour, respectively.

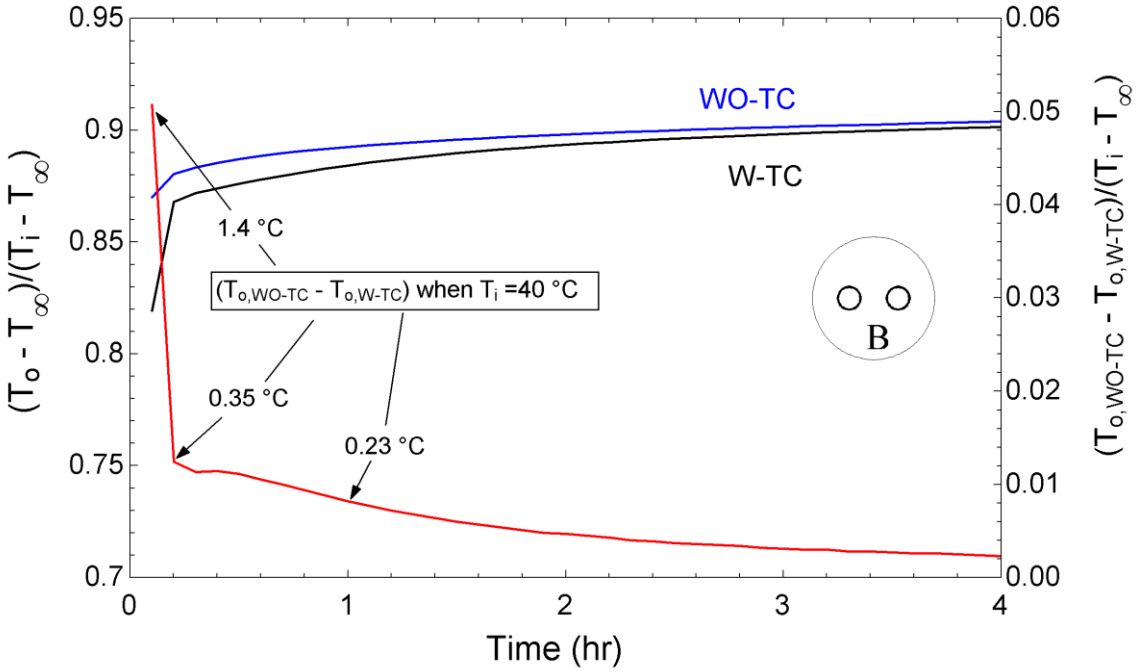

Figure 2.11: Non-dimensional outlet temperatures with and without thermal capacity effects.

2.5.2 Annual simulations

The proposed model was coded in EES (Klein, 2011) so as to enable annual simulations. In this section, annual simulations are performed to determine the impact of the borehole thermal capacity on the annual energy consumption of a heat pump. The characteristics of the borehole used for these simulations are given in Table 2.4. In order to make a fair comparison between cases with and without borehole thermal capacity, the final borehole simulations were decoupled from the building and the heat pump so that both cases would be examined with the same inlet conditions. The procedure to obtain these inlet conditions involves two steps.

First, preliminary simulations were performed in TRNSYS for a well-insulated building in a cold climate (Montreal, Canada). The building heating load was determined by assuming a constant internal temperature. The resulting annual space heating requirement is 11910 kWh with a peak heating load of 5.2 kW. In the summer, the building heating load is zero and the cooling load is assumed to be negligible.

In the second step, a 3-ton (10 kW) heat pump, whose characteristics are given in Figure 2.13, was linked to a borehole with a negligible thermal capacity. Using the building load determined in the first step, a simulation of the combined borehole/heat pump arrangement was performed with a 6 minute time step. This time step was selected as it represents a typical off-time that heat pump manufacturers use to avoid excessive cycling. During a given time step, the heat pump was operating whenever the difference between the cumulative building heat requirement and the cumulative heat injection from the heat pump was positive. The heat pump capacity and compressor power as well as the inlet temperature to the borehole were then determined iteratively as the performance of the heat pump depends on the borehole outlet temperature and vice versa. When the difference between the cumulative building heat requirement and the cumulative heat injection from the heat pump was negative, the heat pump was not operating during that time step and the inlet flow rate to the borehole was set to zero.

The resulting borehole inlet temperature, which varied from -8 °C to 12 °C, is shown in Figure 2.12 for the entire heating season (5600 hours). During that period, the heat pump is operating for a total of about 1450 hours. The flow rate alternates between 0.442 and 0 kg/s corresponding to the on/off operation of the heat pump. These values of inlet temperature and flow rates are then used as inputs to the proposed model and annual simulations are performed with a 6 minute time step. The time required for an annual simulation (56000 time steps) is of the order of 2 to 3 hours on a typical personal computer. The outlet temperature from the borehole is then used to determine heat pump energy consumption, power input and the resulting COP at each time step based on the performance map of a typical 3-ton (10 kW) geothermal heat pump presented in Figure 2.13.

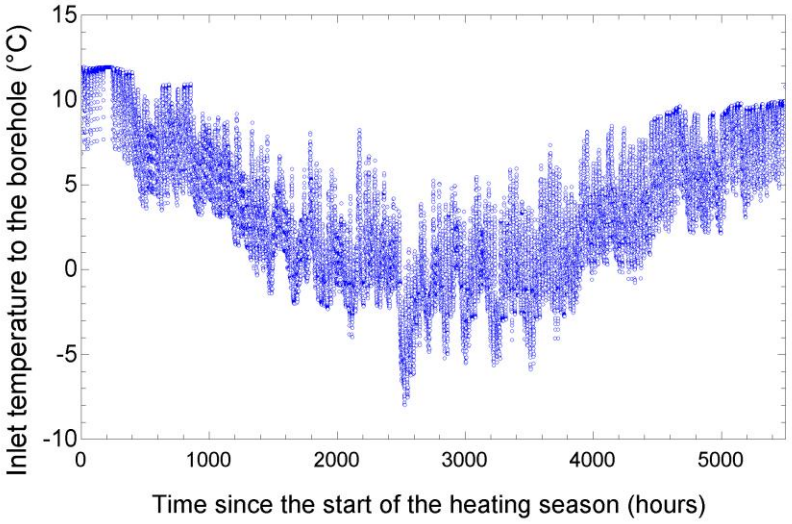

Figure 2.12: Inlet temperatures to the borehole used in annual simulations.

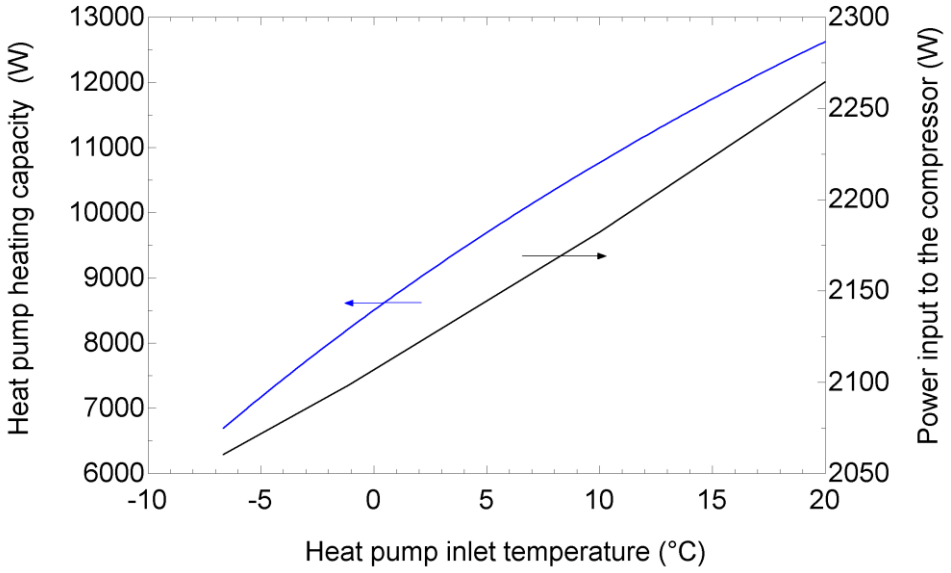

Figure 2.13: Heat pump performance characteristics as a function of the inlet temperature.

The effect of borehole thermal capacity (fluid and ground) is presented in Figure 2.14. These data points represent the borehole outlet temperature when the heat pump is operating. Two cases are presented. The first case are results obtained when borehole thermal capacity is included (W-TC) while the bottom curve (WO-TC) presents results obtained by setting the grout capacity to a very small value and by setting the product of $\rho_{f,eq} c_{f,eq} V_{eq}$ in Equation (2.17) equal to zero.

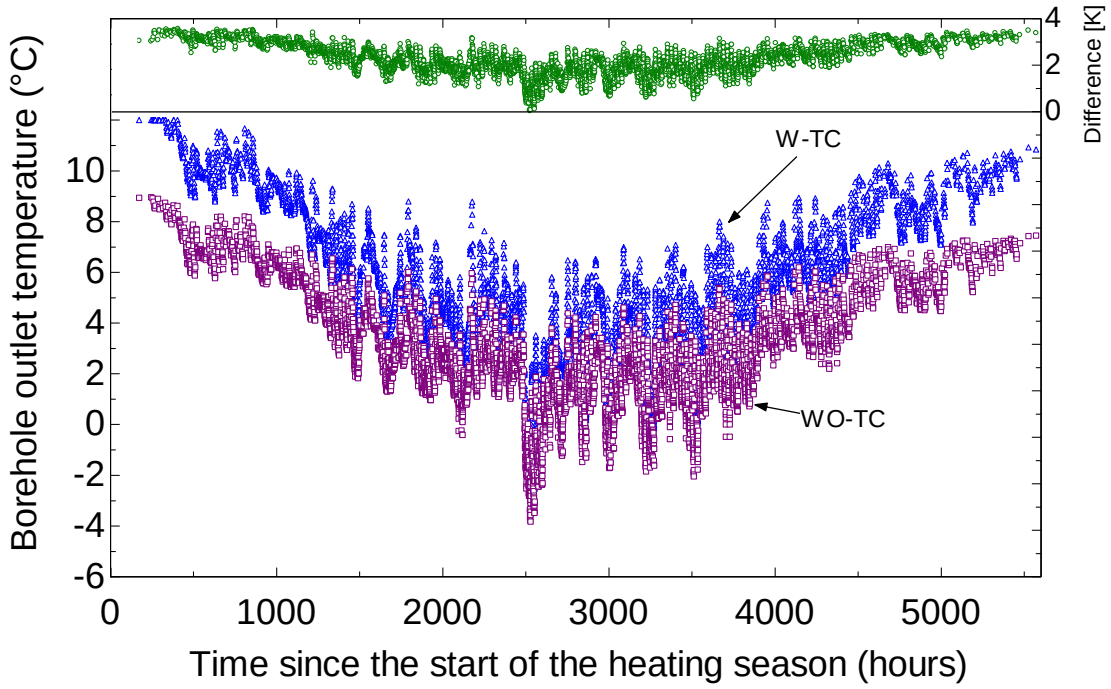

Figure 2.14: Effect of borehole thermal capacity on the borehole outlet temperature.

These two assumptions imply that grout and fluid thermal capacities are excluded and that heat transfer in the borehole is modeled with a steady-state thermal resistance. The top curve in Figure 2.14 shows the temperature difference between both curves.

As shown in Figure 2.14, the effect of including the borehole thermal capacity is relatively important. Throughout the heating season, the borehole outlet temperature is always higher when borehole thermal capacity is included. When the heat pump is operating infrequently (at the beginning and at the end of the heating season) the difference is relatively important and it reaches a maximum value of 3.6 °C. During peak heating, near t = 2551 hours, the heat pump is operating almost continuously and the difference between the two curves diminishes down to a negligible value. These differences can be explained by referring to Figure 2.15 and 2.16 which show temperature profiles for consecutive time steps around t = 5164 and 2551 hours, respectively. The grout region is represented by a grey area and the temperature for $r_{eq} < 0.0255$ m is the mean fluid temperature in the pipe, T_m.

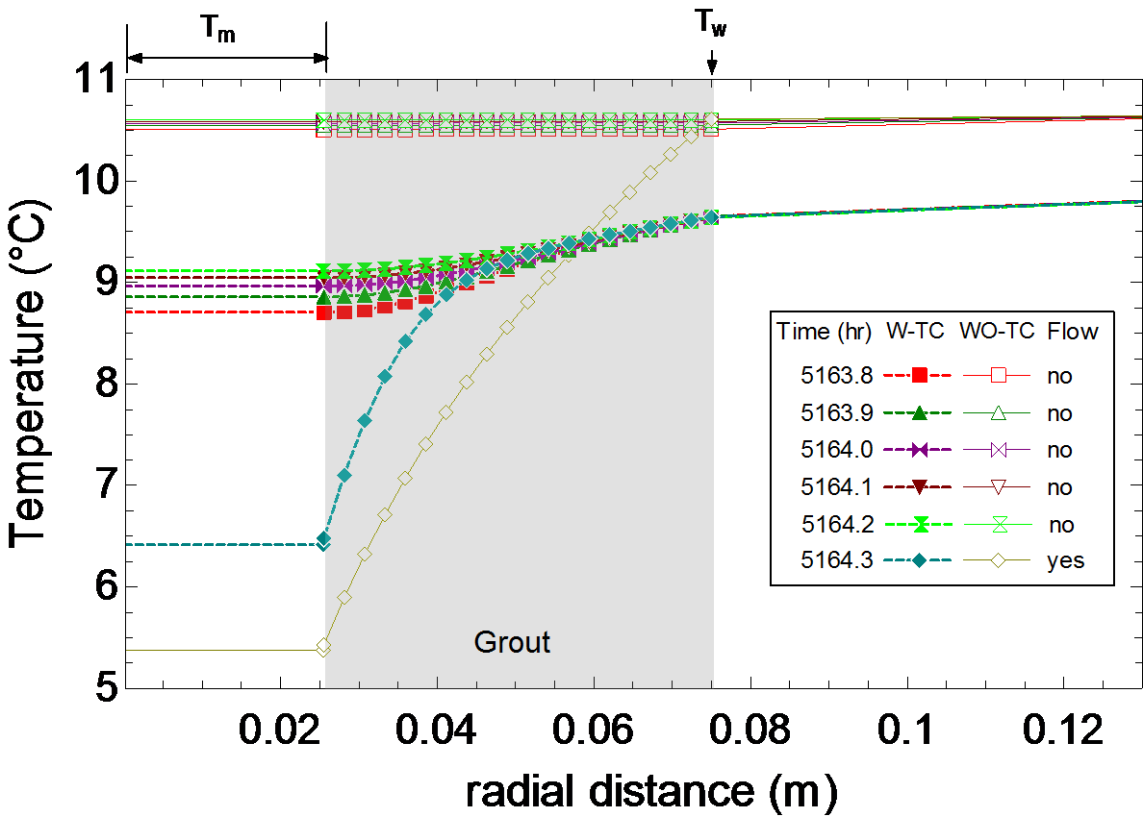

Figure 2.15: Temperature profile for six consecutive time steps.

Figure 2.15 shows the temperature profile change when fluid is introduced in the borehole at t = 5164.3 hr after five consecutive time steps (i.e., 30 minutes) of no flow conditions. For t < 5164.3 hr, there are two distinct behaviors for the W-TC and WO-TC cases. The WO-TC curves are very similar with flat temperature profiles around 10.5 ^{o}C for r_b < 0.075 m. This is to be expected as the proposed model assumes that T_m and T_{req} are equal to the borehole wall temperature T_w when the grout and fluid thermal capacities are neglected. For r_b > 0.075 m, the temperature in the ground increases slightly with time as there is heat conduction from the far-field to the borehole wall.

The W-TC curves show the same trend for t < 5164.3 hr. As time increases, the fluid and grout temperatures increase indicating that there is heat transfer from the ground. It is interesting to note that the borehole wall temperature for the W-TC case is approximately 1 ^{o}C below the WO-TC case. In other words, the cumulative effect, after 5164 hours of operation, of not accounting for grout and fluid thermal capacities results in a borehole wall temperature about 1 ^{o}C higher

than the one predicted by the W-TC case. In effect, when the heat pump is not operating and borehole thermal capacity is neglected, the borehole wall boundary becomes adiabatic which raises the borehole wall temperature. For the W-TC case, the non-circulating fluid acts as a sink which lowers the borehole wall temperature.

At t = 5164.3 hr, flow is reestablished in the borehole with an inlet fluid temperature of 4.5 ^{o}C (not shown on Figure 2.15). For the WO-TC case, the temperature in the grout reaches its steady-state profile instantly with a resulting value of T_m = 5.4 ^{o}C. This profile is logarithmic in nature due to the cylindrical geometry. For the W-TC case, T_m is higher and reaches a value of 6.4 ^{o}C despite the fact that the borehole wall temperature is lower (almost 1°C lower compared to the WO-TC case). This can be explained by looking at the transition from t = 5164.2 to 5164.3 hr. At t = 5164.2 hr, the grout temperature varies from 9.1 ^{o}C to 9.6 ^{o}C from r_{eq} to r_b. At t = 5164.3 hr, the grout is releasing its accumulated heat to the fluid and the grout temperature drops down to 6.5 ^{o}C at r_{eq}. The temperature drop in the grout extends up to about r = 0.055 m. The end result is that the outlet fluid temperature from the borehole (i.e., the heat pump inlet temperature) is higher when the grout and fluid thermal capacities are accounted for. As will be shown shortly, this has an impact on the annual average heat pump COP.

As shown in Figure 2.16, the behavior is slightly different when the heat pump is operating frequently. In this figure, only the temperature profiles up to r = 0.05 m are presented and the profiles for t = 2250.8, 2550.9, and 2551.0 hr have been omitted for clarity. Prior to t = 2550.7 hr, the heat pump had been operating frequently. As a result, the grout temperature profiles are similar for both the W-TC and WO-TC curves at t = 2550.7 hr. However, the W-TC curve is higher resulting in a higher mean fluid temperature of -5.5 ^{o}C compared to -6 ^{o}C for the WO-TC case. A similar behavior is observed for t = 2551.1 hr. In other words, when the heat pump is working frequently, the behavior of the borehole can be suitably approximated using steady-state thermal resistances. Under a no flow condition, at t = 2551.2 hr, the temperature profile changes are relatively important. The WO-TC profile increases to the borehole wall temperature, i.e., 6 ^{o}C. For the W-TC case, the temperature in the grout in the vicinity of r_{eq} increases from -5.5 ^{o}C to -2.7 ^{o}C due to heat conduction form the borehole wall. This increases the mean fluid temperature up to -4.0 ^{o}C. It should be noted that the steep gradient observed for the W-TC case at t = 2551.2 hr is the result of a relatively small natural convection film coefficient when there is no flow. At t = 2551.3 hr, there is flow and the inlet fluid temperature is -6.2 ^{o}C (not shown in Figure 2.16).

Even though the grout was warmed up in the previous 6 minutes, it is insufficient to make a substantial difference in the mean fluid temperature and both mean fluid temperatures are almost identical and equal to -4.3 ^{o}C for t = 2551.3 hr.

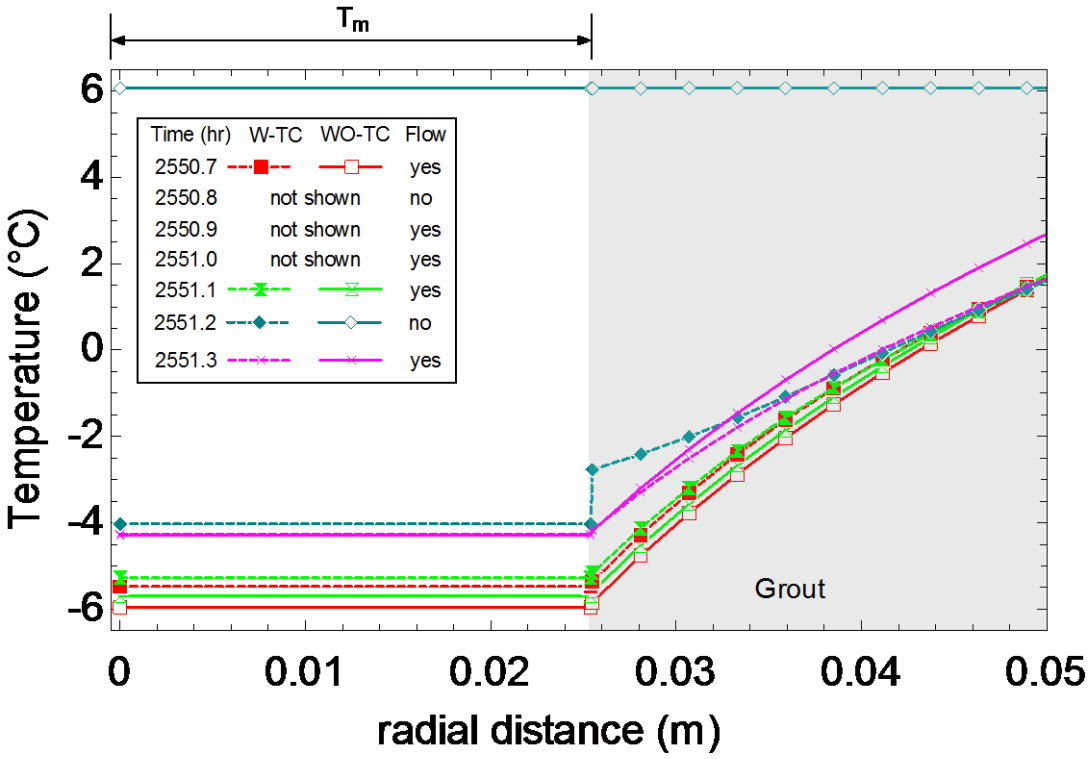

Figure 2.16: The temperature profile for seven consecutive time steps for frequent heat pump operation.

Finally, it is interesting to examine the impact of grout and fluid thermal capacities on the annual heat pump COP. This value is obtained by calculating the ratio of the annual cumulative heat pump capacity over the annual cumulative power input to the heat pump.

As shown in Table 2.5, the impact on the COP is 4.58% for the B configuration (which was used for Figure 2.14 to 2.16). In other words, the heat pump COP is underestimated by 4.58% when the borehole simulations do not account for the grout and fluid thermal capacities. Simulations for the A and C configurations show similar results

Table 2.5: Effect of accounting for thermal capacity on the annual heat pump COP.

	B		A		C	
	WO-TC	W-TC	WO-TC	W-TC	WO-TC	W-TC
Minimum outlet temperature (°C)	-3.9	-2.9	-4.4	-3.4	-2.5	-1.7
COP	3.77	3.96	3.74	3.93	3.86	4.02
% difference in COP	4.58%		4.63%		4.02%	

2.6 Conclusion

A one-dimensional transient borehole model is proposed to account for fluid and grout thermal capacities in borehole ground heat exchangers with the objective of predicting the outlet fluid temperature for varying inlet temperature and flow rate. The standard two-pipe configuration is replaced with an equivalent geometry consisting of a single pipe and a cylinder core filled with grout. Axial variations are neglected and the fluid in the borehole is assumed to be at a mean fluid temperature over the length of the borehole. Transient radial heat transfer in the grout is solved numerically while the ground outside the borehole is treated analytically using the cylindrical heat source method. The proposed model is validated successfully against analytical solutions and experimental results.

The model is used to study the impact of borehole thermal capacity on the prediction of the outlet fluid temperature. For a typical two-pipe B configuration borehole, an initial temperatures of 12 ^{o}C and a sudden increase in fluid temperature to 40 ^{o}C, it is shown that the fluid outlet temperature predicted without and with borehole thermal capacity differ by 1.4, 0.35, and 0.23 °C after 0.1, 0.2 and 1 hour, respectively.

Annual simulations are also performed over an entire heating season (5600 hours) with a 6 minute time step with (W-TC) and without (WO-TC) borehole thermal capacity. The flow rate in the borehole is non-zero only when the heat pump is operating, i.e., for about 1450 hours during the year. Throughout the heating season, the borehole outlet temperature is always higher for the W-TC case. When the heat pump is operating infrequently (at the beginning and at the end of the heating season) the difference in the outlet temperature predictions reaches a maximum value of 3.6 °C. During peak heating, the heat pump is operating almost continuously and the difference between the W-TC and WO-TC cases diminishes down to a negligible value. The annual COP

predicted is approximately 4.58% higher when borehole thermal capacity is included. In other words, the annual heat pump COP is underestimated by 4.58% when the borehole simulations do not account for the grout and fluid thermal capacities. Variations of 4.63% and 4.02% are observed for the A and C pipe configurations, respectively.

The differences observed in the annual COP values and outlet fluid temperatures are specific to the case tested. However, based on the analysis reported here, it is likely that the difference in annual COP values will decrease when the heat pump operates more frequently during a heating season.

CHAPTER 3 NUMERICAL MODELING OF TRANSIENT GROUND HEAT TRANSFER

3.1 Introduction

Following the analysis of thermal capacity effects in boreholes presented in Chapter 2, this chapter examines transient heat transfer from the borehole wall outwards, i.e., in the ground. As shown later in Chapter 5, axial heat transfer effects become important after certain time period of heat injection to the ground. The significance of the axial effects while modeling ground heat exchangers (or sizing a bore field) is stressed by Marcotte et al. (2010) and Claesson and Hellström (2011), particularly for short boreholes. A transient axi-symmetric numerical model is developed to study the two-dimensional radial and axial heat transfer in the ground. Various boundary conditions can be applied to the boundaries of the calculation domain. In the radial direction, the model is capable of handling three distinct layers. This was done so that the borehole could eventually be included in the model by replacing the U-tube geometry by an equivalent diameter much like the approach used in Chapter 2. Thus, the model could eventually account for a series of concentric cylinders composed of a pipe, the grout, and the ground. As shown in Figure 3.1, the model can account for multiple layers of ground in the vertical direction which could prove to be useful for simulating boreholes in grounds composed of different layers.

The numerical model was coded in FORTRAN. Although it would have been possible to use commercially available software tools (e.g., COMSOL) to solve this problem, it was felt that a code developed in-house could be used with the other ground heat exchanger simulation tools developed in the group and that it could eventually be transported to TRNSYS.

This chapter starts with a presentation of the numerical model. Then, the model is compared with a numerical one-dimensional (radial) transient model and the two-dimensional (radial-axial) finite line source analytical solution. A validation with experimental results is presented in Chapter 5.

3.2 Governing equations

As shown in Figure 3.1, the calculation domain can be viewed as a composite cylinder, consisting of a number of vertically stacked disks each with its own set of properties. The overall height of the calculation domain is *H*, and it is delimited by an internal radius r_{in} and a far-field radius r_{∞}.

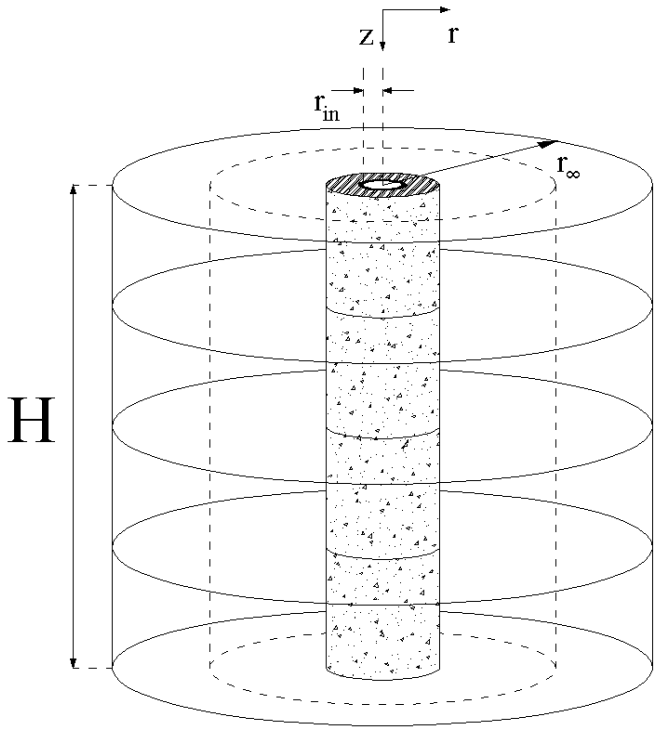

Figure 3.1: Schematic representation of the calculation domain.

3.2.1 Assumptions

The following assumptions are used:

- Each distinct ground layer (as explained above) is a homogeneous medium.
- Thermal properties of each ground layer are constant, isotropic and independent of temperature.
- Phase changes as well as moisture migration and natural convection are ignored and pure conduction is the only heat transfer mode in the ground.

3.2.2 Mathematical formulation

The problem is governed by the unsteady two-dimensional (*r*,*z*) energy equation in cylindrical coordinates:

$$\rho c_p \frac{\partial T}{\partial t} = \frac{1}{r}\frac{\partial}{\partial r}\left(kr \frac{\partial T}{\partial r} \right) + \frac{\partial}{\partial z}\left(k \frac{\partial T}{\partial z} \right) \tag{3.1}$$

where k (W/m-K) stands for thermal conductivity and ρC (J/m^3-K) denotes the volumetric heat capacity.

3.2.3 Boundary conditions

Figure 3.2 shows a schematic of a slice of the calculation domain with the four boundary conditions: at the borehole wall, BC-L (shown here as BCx-L representing different boundary conditions imposed on different segments of the left boundary), at the top, BC-T; at the far-field (or at the right), BC-R; and at the bottom, BC-B.

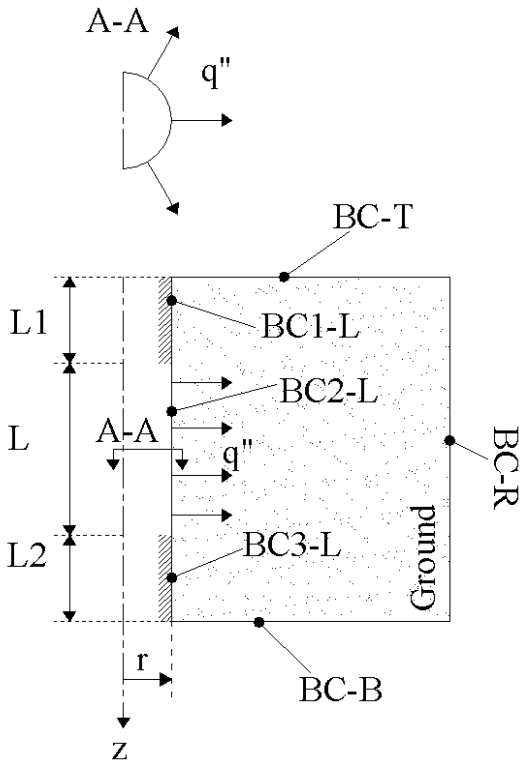

Figure 3.2: Nomenclature used for the boundary conditions.

The boundary condition on each of the four boundaries can be set to any of the classic boundary conditions: i) given temperature; ii) given heat flux; iii) convective heat flux. Furthermore, it is possible to impose different boundary conditions on segments along any of the four boundaries much like what is shown for the BC-L boundary condition. As will be shown shortly, this feature has been used on the BCx-L boundary which is divided into three segments *L1*, *L* and *L2*. The top and bottom segments (i.e., BC1-L and BC3-L) are being subjected to an adiabatic boundary condition while the active borehole length, L, is subjected to a non-zero heat flux boundary condition.

3.2.4 Numerical approach

The problem is solved numerically using the control volume-based finite difference method (CVFDM) of Patankar (1980) with the fully implicit scheme. Using the nomenclature presented in Figure 3.3, the discretization equation for an internal node *P* is given by:

$$a_P T_P = a_E T_E + a_W T_W + a_T T_T + a_B T_B + b \tag{3.2}$$

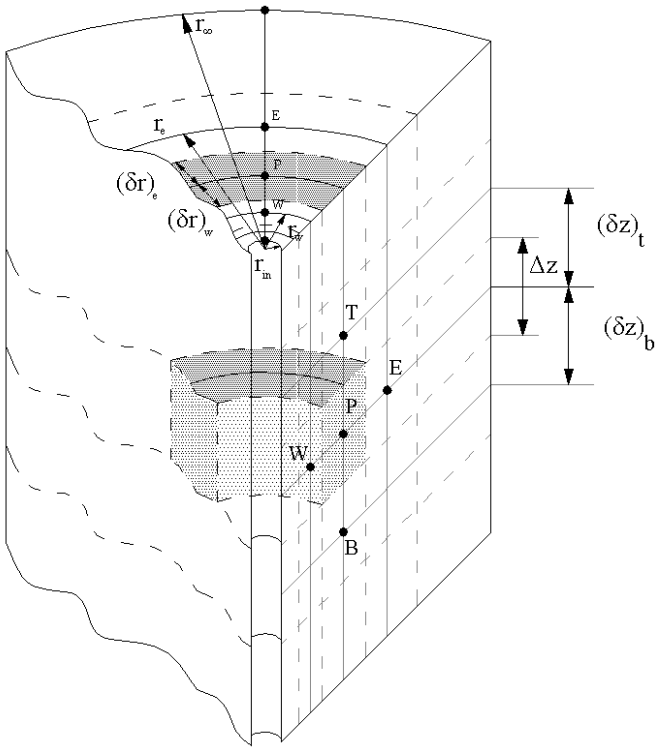

Figure 3.3: Schematic representation of an internal control volume in the calculation domain.

where the coefficients are:

$$
\begin{aligned}
&a_E = r_e.\Delta z \frac{k_e}{(\delta r)_e} \quad , \quad a_W = r_w.\Delta z \frac{k_w}{(\delta r)_w} \\
&a_T = \frac{1}{2}\left(r_e^2 - r_w^2\right)\frac{k_t}{(\delta z)_t} \quad , \quad a_B = \frac{1}{2}\left(r_e^2 - r_w^2\right)\frac{k_b}{(\delta z)_b} \\
&a_P^0 = \frac{\rho c_P}{2\Delta t}\left(r_e^2 - r_w^2\right).\Delta z \quad , \quad b = a_P^0 T_P^0 \\
&a_P = a_P^0 + a_E + a_W + a_T + a_B
\end{aligned}
\tag{3.3}
$$

The superscript " ^{0} " refers to conditions at the end of the previous time step and Δt is the time step. Interface conductivity is calculated at the interfaces of neighboring control volumes, in both the radial and axial directions.

The Type-B grid approach, as described by Patankar (1980) is used. In this approach, the control volumes and their faces are located first; then the nodes are placed at the center of each control volume. The calculation domain is entirely filled with "full" control volumes. At the boundaries, the "interface" of the control volumes coincides with the boundaries and the half control volumes presented in section 2.4.2 shrink to an infinitesimal width. A non-uniform grid structure, in both the radial and axial directions is used. This permits to concentrate grid points in the areas of steep gradients. It should be noted that grid independence checks were performed for each problem reported in this chapter and Chapter 5. At the boundaries, quadratic interpolation is used for calculating the coefficients following the method proposed by Baliga and Atabaki (2006). An iterative line Gauss-Seidel algorithm which is based on a line-by-line application of the TDMA method is used to solve the set of discretization equations.

3.3 Verification of the model

In this section, the numerical model is verified by comparing its results against those of another numerical model (1-D) and the two-dimensional (radial-axial) finite line source analytical solution.

3.3.1 Comparison with another 1-D numerical model

The two-dimensional model proposed here is used in 1-D (radial) mode by imposing adiabatic boundary conditions on the top and bottom boundaries (BC-T and BC-B). The results are

compared with the transient one-dimensional ground model proposed by Eslami Nejad and Bernier (2012). The geometry consists of a 1 m high hollow cylinder (which represents the borehole) with an interior radius of r_{in}=0.01 m (i.e., the borehole radius as used later) and exterior radius of r_{∞} =1 m. The cylinder has a thermal conductivity of 2.5 W/(m.K) and a volumetric heat capacity of 2.5 MJ/(m^3.K). A time step of one second and a grid mesh of 52×52 nodes are used for the proposed 2-D numerical model. The whole domain is initially at T_0 = 50°C and the simulation time is two hours. The comparison is done for two cases representing two different sets of boundary conditions.

Case 1: Imposed heat flux at the borehole wall

For this case, and with reference to Figure 3.2, the values of L1 and L2 are zero. The BC-R, boundary is adiabatic while BC-L is set to a heat flux corresponding to a constant heat transfer rate per unit length of 30W/m. The radial temperature variations over the whole calculation domain after two hours of simulation from both numerical models are shown in Figure 3.4. Excellent agreement can be observed between the two models.

The results from the proposed model are presented using isotherms in Figure 3.5. It can be observed that all the isotherms are vertical and straight which is characteristic of radial heat transfer. It indicates that the top and bottom boundary conditions are implemented correctly.

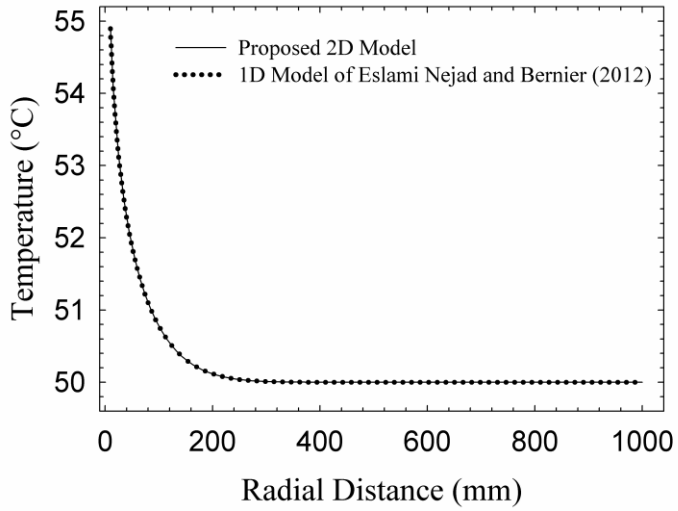

Figure 3.4: Modeling results comparison for case 1, *t*=.7200s.

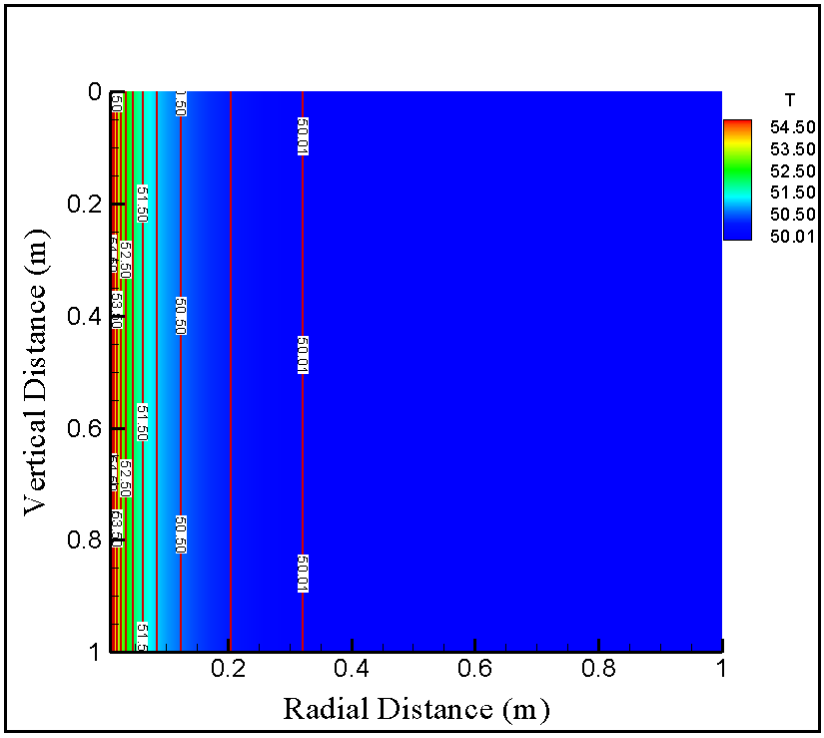

Figure 3.5: Isotherms from the proposed numerical model for case 1 at t =7200s.

Case 2: Imposed heat flux at the borehole wall and fixed temperature at the far-field

This case is similar to Case 1 except that the right boundary, BC-R, is maintained at a constant temperature of 0°C instead of being adiabatic. The comparison between the two models is presented in Figure 3.6. Here again there is excellent agreement between the two numerical models.

3.3.2 Comparison with the FLS solution

In this section, the 2-D capability of the proposed model is tested by comparing its results against the well-known finite line source (FLS) solution. The FLS is an exact solution to the two-dimensional (radial-axial) heat transfer from a finite line source in a semi-infinite homogeneous medium subjected to a constant and uniform heat transfer rate per unit length.

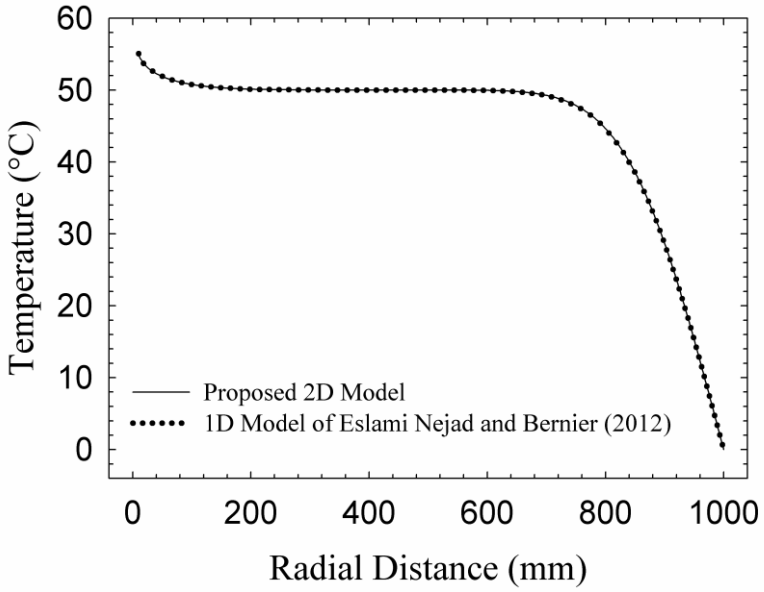

Figure 3.6: Modeling results, comparison for case 2 at t =7200s.

The far-field temperature, as well as the initial temperature are equal to T_0. The extent of the domain is infinite on the right and bottom boundaries as shown in Figure 3.7b. The details of this solution are outside the scope of this thesis; only the final equation, as presented by Zeng et al. (2002) is shown below (Equation 3.4).

$$T(r,z,t)-T_0=\frac{q'}{4\pi k}\int_0^H\left\{\frac{erfc\left(\frac{\sqrt{r^2+(z-h)^2}}{2\sqrt{\alpha t}}\right)}{\sqrt{r^2+(z-h)^2}}-\frac{erfc\left(\frac{\sqrt{r^2+(z+h)^2}}{2\sqrt{\alpha t}}\right)}{\sqrt{r^2+(z+h)^2}}\right\}dh \qquad (3.4)$$

where H is the line source length, t is the time, and h is the integration variable. The other variables have their usual meaning and have been described earlier in the chapter. With Equation 3.4, it is possible to obtain the temperature in the medium (e.g., ground) at a point located at a distance r form the line source and a depth z below the ground surface.

As mentioned earlier, Ingersoll et al. (1954) established that the infinite line source solution is reasonably accurate when the Fourier number ($Fo = \alpha t/r^2$) is greater than 20. Considering that the finite line source solution is also based on a line source it is reasonable to assume that this

criterion applies equally to the FLS solution. Philippe et al. (2009) established that this criterion corresponds to an error of 2.6% when compared to the cylindrical heat source solution where the heat transfer rate is applied at a finite radius. As an example, if Fo = 20, r = 0.01m, and $\alpha = 10^{-6}$ m^2/s, then t = 2000 s. The temperature difference at r = 0.01 m obtained from a finite line of infinitesimal radius subjected to a uniform heat transfer rate per unit length (Equation 3.4) will have an error of 2.6% at t = 2000 s. In the present case, results are examined at t = 86400 s (one day), giving a Fo = 864 which is much greater than the accuracy limit set by Ingersoll et al. Therefore the FLS calculation can be considered to be accurate for t = 86400 s (one day).

The proposed numerical model has a finite radius at the BC-L boundary while the FLS solution is for a line with an infinitesimal radius. Therefore the comparison has to be performed with slightly different geometries which are shown in Figure 3.7.

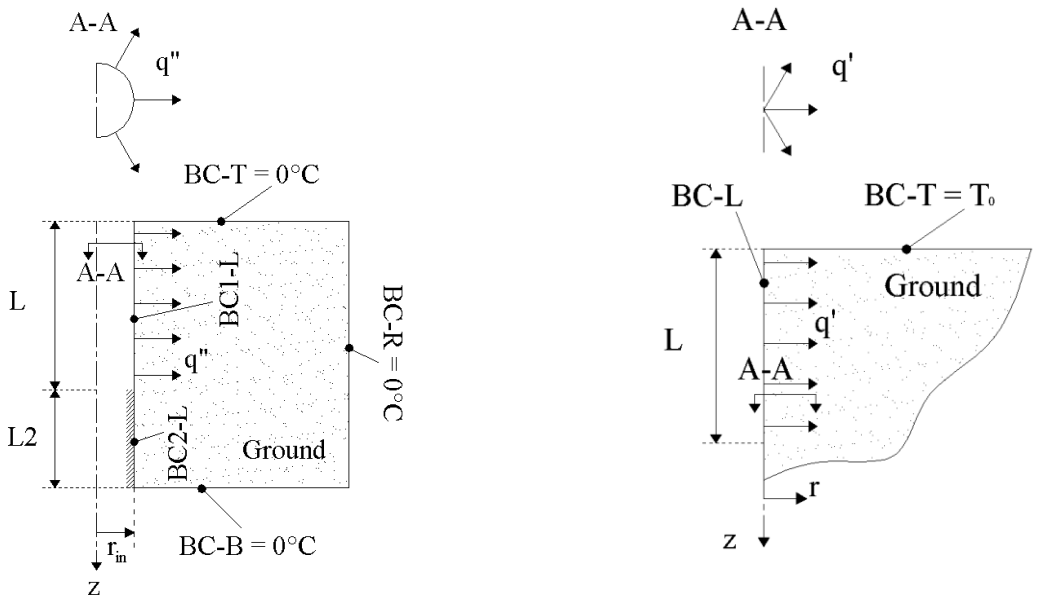

(a) (b)

Figure 3.7: Geometry used for the proposed model (a) and for the FLS geometry (b).

As shown in Figure 3.7a, the geometry used for the proposed model consists of a 10 m long hollow cylinder (which represents the borehole) with an inner radius of r_{in} =0.01 m. This portion of the domain (BC-L) is subjected to a heat flux corresponding to a constant heat transfer rate per

unit length of 50 W/m. From the bottom end of the borehole, the calculation domain extends for another 5 m (denoted by *L2* in Figure 3.7a) with an adiabatic boundary condition at BC2-L. The whole calculation domain is initially at T_0 = 0°C and extends up to r_∞ = 10 m. It should be mentioned that the far-field radial distance as well as the 5 m height of the bottom disk are chosen such that the boundary conditions imposed at the right and bottom of the domain do not affect the results for a simulation lasting one day. The geometry used for the FLS solution is shown in Figure 3.7b. The line source is in the center of a semi-infinite medium and the line has a finite length L of 10 m. The heat transfer rate per unit length is also 50 W/m and the whole calculation domain is initially at T_0=0°C.

The comparison is made using a ground with a thermal conductivity of 2.5 W/(m-K) and a volumetric heat capacity of 2.5 MJ/(m^3.K). Results are presented at the end of a one day simulation. A time step of one second and a relatively fine grid mesh of 902 × 902 nodes are used for the numerical simulation. The FLS calculated from the line source up to a radial distance of 1 m for the same vertical dimension as of the 2-D model at 4500 points formed at the intersections of 30 and 150 points in the radial and axial direction, respectively.

For clarity, the comparison of the resulting isotherms is shown in three parts; in Figure 3.8 for the top part of the domain, in Figure 3.9 for the middle part and in Figure 3.10 for the bottom section of the BC-L boundary condition.

Overall, there is very good agreement between the two sets of results. The isotherms are curved near the top and bottom of the borehole at z = 0 and 10 m indicating, as expected, that there is heat transfer in both the axial and radial directions. In the middle of the borehole (Figure 3.9), the isotherms are essentially vertical indicating that there is only radial heat flow in this area. In Figure 3.10, a small discrepancy exists between the two sets of isotherms in the vicinity of z = 10 m. This might be attributable to two causes. First the grid size is relatively coarse for the FLS solution. It is believed that a finer grid would lead to a better agreement. The second reason for the discrepancy is the difference between the two geometries at z = 10 m (Figure 3.7). For the FLS solution, the heat transfer rate is imposed at r = 0, while it is imposed at r_{in} in the numerical model.

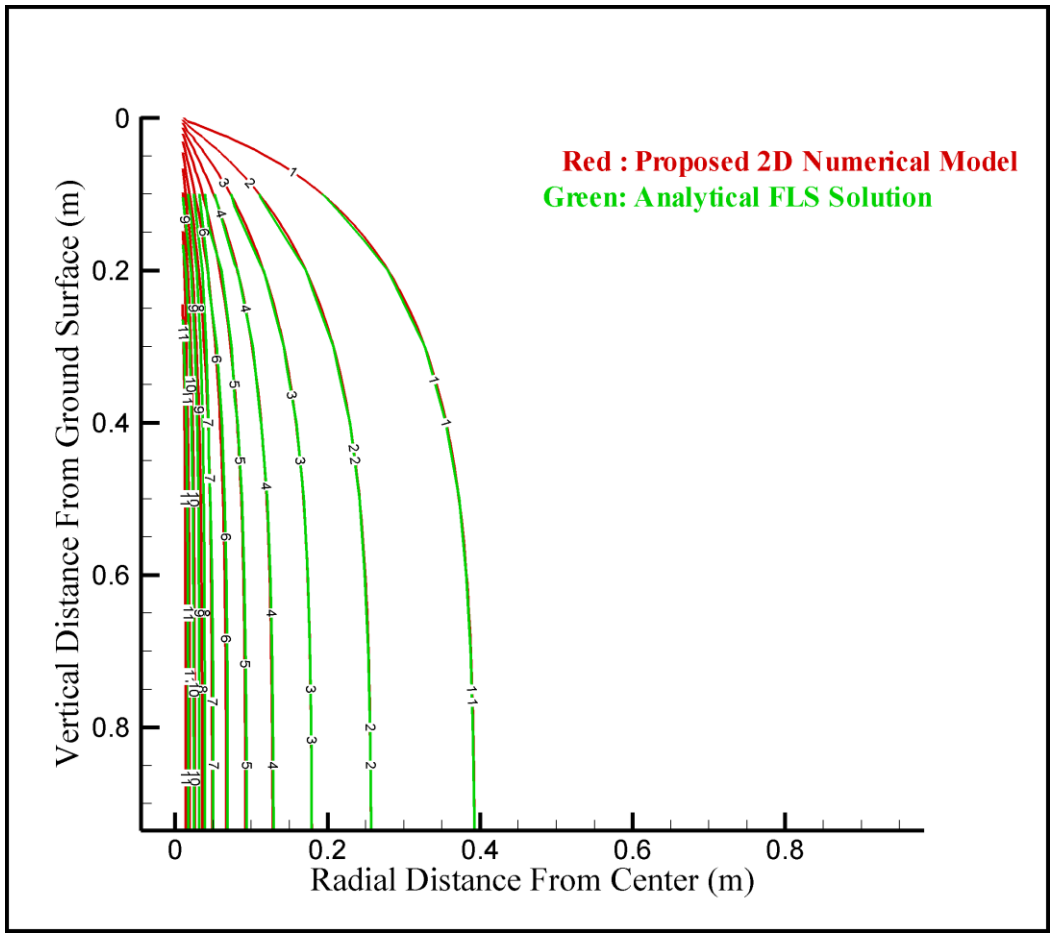

Figure 3.8: Comparison of isotherms/results from the 2-D-model and the FLS solution after one day simulation time at the upper part of the domain/borehole.

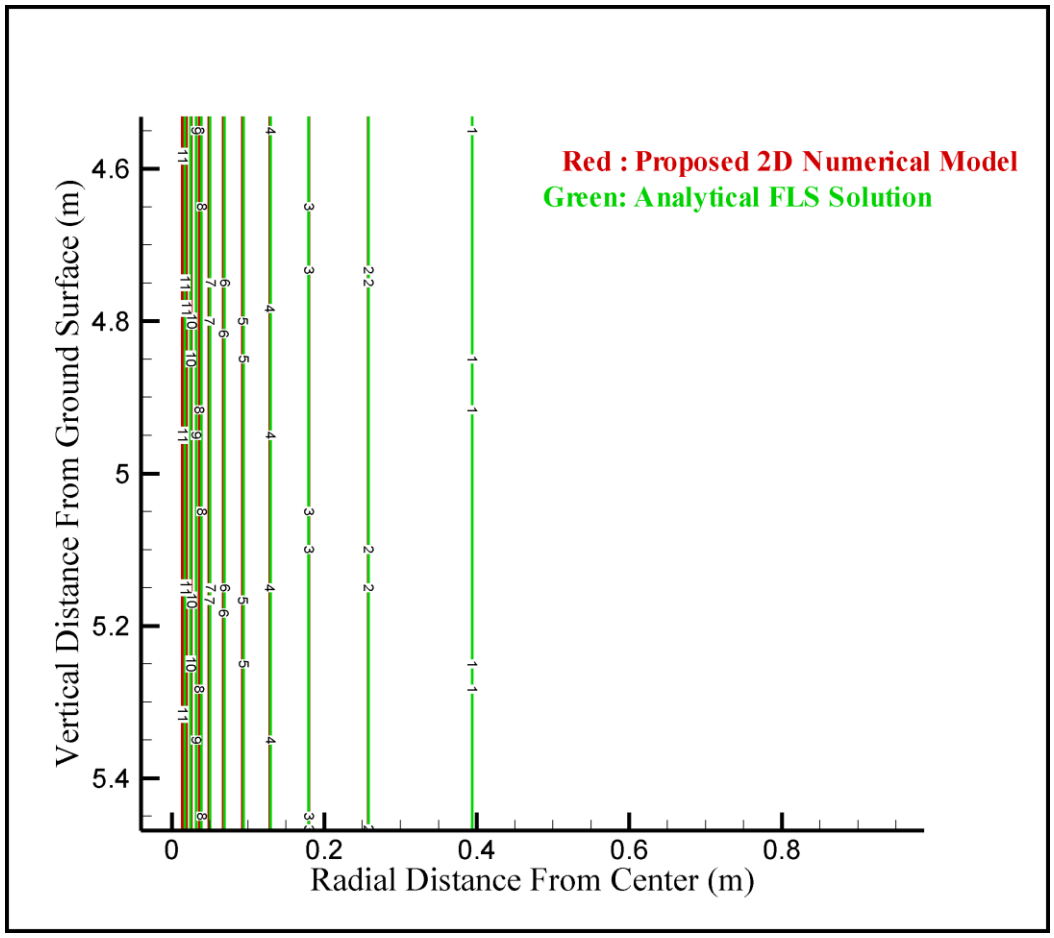

Figure 3.9: Comparison of isotherms/results from the 2-D-model and the FLS solution after one day simulation time at the mid-part of the borehole.

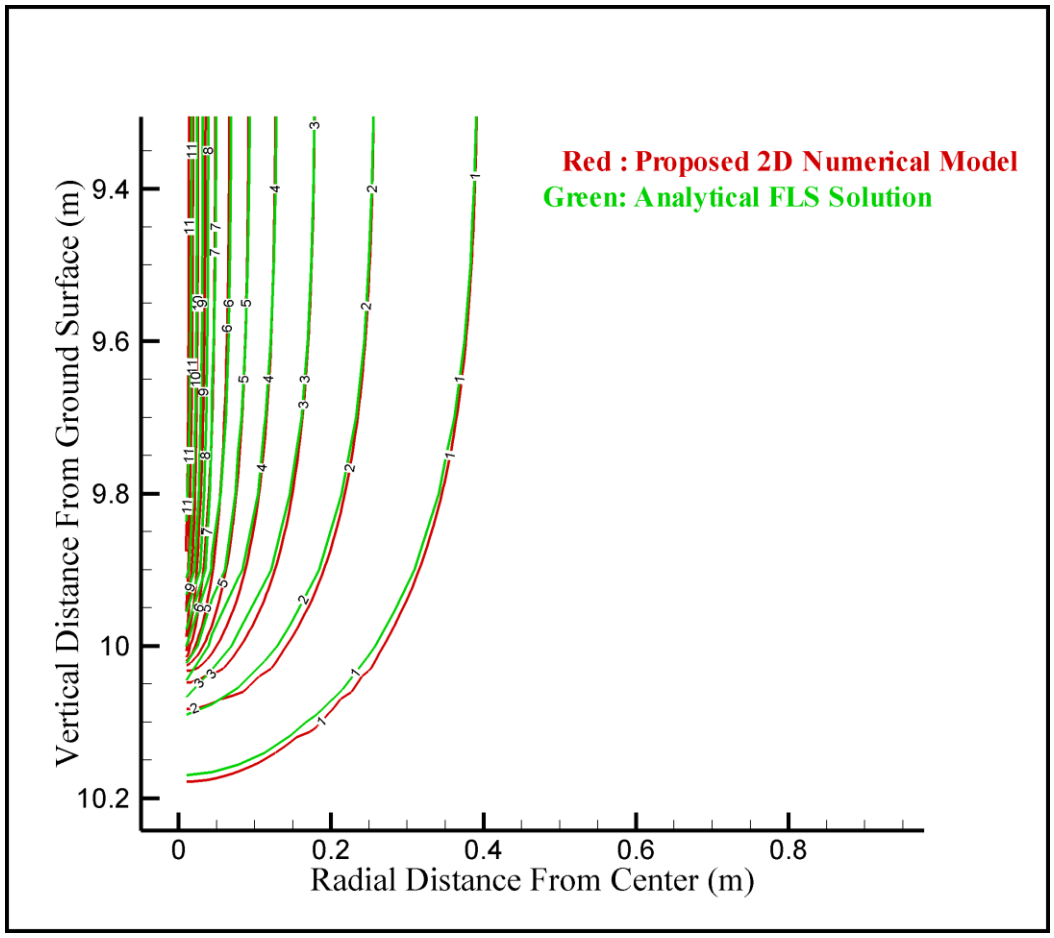

Figure 3.10: Comparison of isotherms/results from the 2-D-model and the FLS solution after one day simulation time at the bottom part of the borehole.

CHAPTER 4 EXPERIMENTAL APPARATUS

4.1 Introduction

A significant part of this research project was devoted to the design, construction and commissioning of an experimental apparatus to study transient heat transfer in geothermal borehole heat exchangers. The main objective is to validate the numerical model presented in Chapter 3 and to provide a data base for future model validations. The borehole length is 1.23 m which is approximately 1/100 the length of typical boreholes.

As shown in Figure 4.1, the heart of the apparatus is a round tank filled with laboratory-grade sand and equipped with a single U-tube borehole at its center. The tank is fully instrumented with temperature probes precisely placed at specific radial, angular and vertical (r,θ,z) positions in the sand. Inlet and outlet fluid temperatures to the borehole are also measured. Experiments can be performed over a wide range of carefully controlled inlet conditions (temperature and flow rate). A computer-based data acquisition system is used to record temperatures as well as the measured fluid flow rate. The tank is located in a laboratory where only outside ventilation is provided. Thus, the lab ambient temperature follows more or less the trend of the outside temperature.

This chapter describes in detail the experimental set-up as well as the experimental procedure used to run an experiment. The results of a preliminary test are presented to highlight some of the difficulties encountered. Calibrations of the temperature probes and the flow meter are presented in Appendices D and E, respectively.

4.2 Description of the experimental apparatus

As shown in Figure 4.1, the experimental apparatus consists of three major groups of components:

1. Fluid conditioning system (identified as numbers 2 to 10 on the top figure)
2. Sand tank with the borehole at its center (number 1)
3. Data acquisition system (number 11)

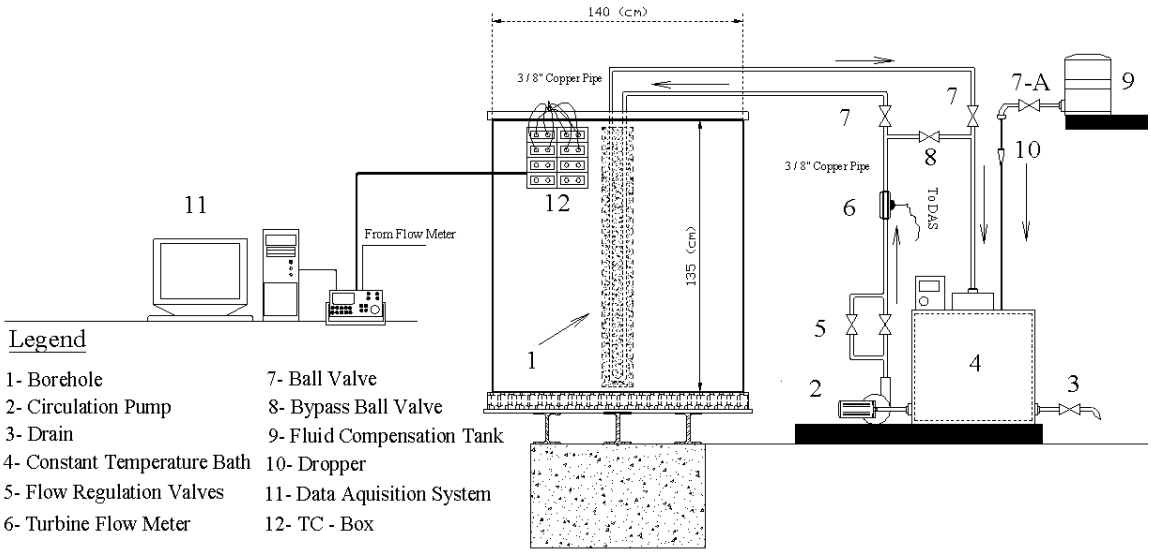

a) Schematic representation of the experimental apparatus.

b) Photo of the experimental apparatus.

Figure 4.1: Experimental apparatus.

4.2.1 Fluid conditioning system

The fluid conditioning system supplies a fluid (water in the present experiments) at specified temperature and flow rate. It consists of the following major elements (numbered from 2 to 10 in Figure 4.1a, respectively):

- Circulation pump (2)

The constant temperature bath is equipped with an external circulating pump. The fluid is pumped from the bath, and then it passes through a filter (not shown on the figure) before going to the borehole via the piping system.

- Drain (3)

The drain is used to empty the constant temperature bath.

- Constant temperature bath (4)

The constant temperature bath (Neslab RTE-220) can maintain the working fluid at temperatures ranging from -23°C to +130°C. In the final experiments reported in Chapter 5, the fluid is maintained at 70°C. The temperature stability of the bath was approximately ± 0.1 ºC.

- Flow regulation valves (5)

Two needle valves are installed on the piping system after the pump and before the turbine flow meter. They are used to set and fine tune the fluid flow rate.

- Turbine flow meter (6)

The flow rate is measured using a turbine flow meter (Omega FTB-1311). It can measure flow rates in the range from 0.3 to 1.5 liters per minute. As shown in Appendix E, the relative global uncertainty on the flow rate measurement given by this flow meter is ±1.5%. Unlike the schematic representation in Figure 4.1a, the flow meter is installed horizontally.

- Bypass valves (7 and 8)

By closing both valves #7 and opening valve #8, the fluid conditioning system is in re-circulation mode. This permits to set the flow rate and inlet temperatures to the desired values without

pumping fluid into the borehole. Thus, conditions can be stabilized prior to testing. When desired conditions are obtained, both valves #7 are opened and valve #8 is closed and fluid is pumped to the borehole. All three valves are adjacent to the borehole (≈ 1m) which means that the borehole experiences an almost immediate jump in inlet conditions when valve #8 is opened.

- Fluid compensation tank (9)

During preliminary testing, it was discovered that fluid evaporation in the constant temperature bath caused changes in the desired inlet conditions with time. With a bath temperature of 70°C, almost 5 liters of water evaporated per day. As will be shown shortly, compensating this water loss with a daily filling was not satisfactory as it perturbed the inlet temperature and flow rate for several minutes. Instead, a fluid compensation tank was designed. It consists of a 25 liters water-filled reservoir equipped with an adjustable dropper (#10) which can supply a small quantity of water (equivalent to a drop) at a constant rate (approximately 3 ml/min which is equivalent to the amount of fluid lost through evaporation from the bath at 70°C). A valve (#7-A) is used to stop the flow from the compensation tank to the bath if required. An air vent (not shown in Figure 4.1a) is installed after the micro-filter at a proper position to remove the air bubbles from the piping system.

The piping system is mainly made of 9 mm (3/8") copper pipes and partly from flexible pipes. Straight 12 mm (1/2") copper pipes are used upstream (25 cm long) and downstream (12 cm long) of the flow meter. These lengths are twice the lengths required by the manufacturer to insure that the flow is fully developed at the entrance of the flow meter. Flexible pipes connect the piping system after the ball valves to the borehole using "push connect" quick fittings. With these quick fittings, the fluid conditioning system can easily be disconnected from the tank for maintenance or other purposes.

It was originally planned to measure the inlet and outlet fluid temperatures with two shielded thermistors (Omega, model TH-44032-1/8NPT-160) However, due to some technical issues, these thermistors could not be used in the final experiment (presented in Chapter 5) and were replaced by two T-type hollow tube thermocouple probes (Omega HTTC36-T-116G-2, TCI-IN and TCI-OUT at inlet and outlet side respectively). For the preliminary experiments reported in the present chapter, the thermistors were still functional and their installation, including the specially made fittings, will now be described. Since the working fluid is pumped to the borehole

at very small flow rates, two mixing sections were designed, machined and installed to mix the fluid upstream of the fluid temperature measurement. The mixing sections consists of a special conical spring (Figure 4.2a) fabricated from a stainless steel wire. The conical spring is inserted inside the copper piece right before the thermistor. In addition to the spring which is situated next to the thermistor's seat, a serpentine path was made by using several 90° elbows which enhances mixing. The serpentine path mixes the fluid before its temperature is measured, first by the thermocouples, and a bit further by the thermistor (Figure 4.2c). Each of the two thermistors is mounted on machined brass pieces which are welded on an 8 cm long piece of 19 mm (3/4") copper pipe (Figure 4.2b and c). The tip of the thermistor reaches the center of the pipe cross section where the fluid temperature is measured.

As shown in Figure 4.2d, the temperature measurement section is insulated with a 1.3 cm thick layer of Armaflex-type insulation. On the inlet side, the thermistor and the thermocouple are located 5.5 and 21.5 cm from the actual borehole inlet. For the outlet, the corresponding lengths are 8.5 cm and 22.5 cm, respectively. It is estimated that for the final experiments, where the mean fluid temperatures to and from the borehole are approximately 67.5 ºC and 66.9°C, the heat losses from the actual borehole inlet and outlet to the temperature measurement section induce a temperature difference of 0.030°C. Finally, two T-type thermocouples are glued at mid-height of the two tubes inside the borehole (not shown) to measure surface temperature and to give an indication of the local fluid temperature.

4.2.2 Sand tank

The sand tank consists of a round Polyethylene tank (1.4 m in diameter and 1.35 m high) filled with laboratory-grade sand. An instrumented borehole is positioned in the center of the tank. A total of 64 Type-T thermocouples are carefully positioned in the sand to measure the evolution of the sand temperature during the experiments.

a) Conical spring machined for the mixing section.

b) Outlet (left) and inlet (right) thermistors and their fittings.

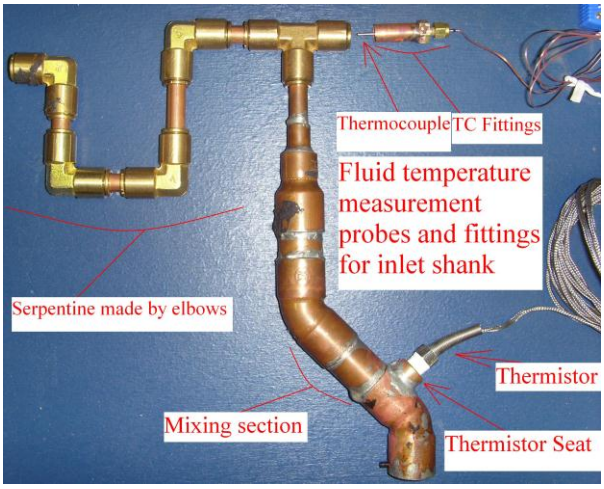

c) Thermistor and inserted thermocouple along with their associated fittings and mixing sections (inlet).

d) Insulated inlet and outlet temperature fluid measurement sections.

Figure 4.2: Photos showing the assembly of the inlet and outlet temperatures measurement sections.

4.2.2.1 Installation of the sand tank

In order to support the mass of the tank (about 5000 kg), the floor of the laboratory had to be reinforced. As shown in Figure 4.3, a steel frame was fabricated and positioned over the floor so that the weight of the tank would be taken by the underground beam and columns.

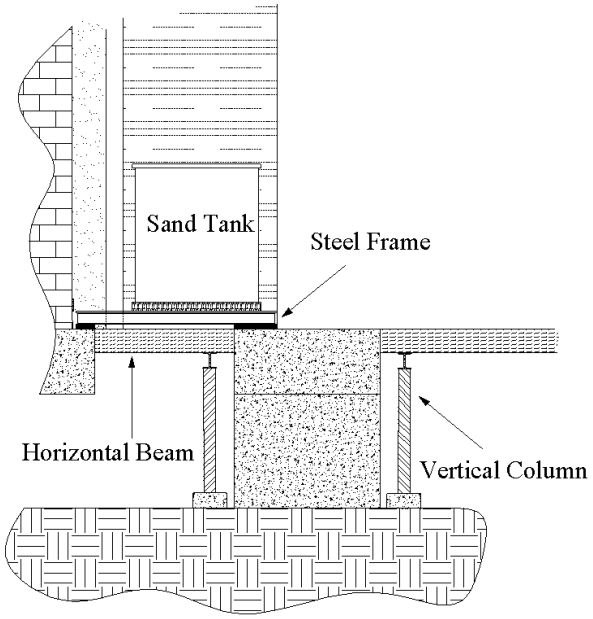

a) Position of the tank over the supporting beam and columns.

b) Steel frame

Figure 4.3: Laboratory floor reinforcement to accommodate the sand tank.

Because of its curvature, the bottom of the tank had to be solidified by pouring a concrete base (Figure 4.4). As shown in Figure 4.4b, the resulting solid "cake" was placed on top of a 5 cm thick layer of rigid insulation (Celfort 200, RSI = 1.76 m^2-K/W) before repositioning the tank on it. As shown in Figure 4.1b, the tank is insulated along its circumference with 25 mm (1") of Armaflex insulation. In addition, the top of the sand below the tank cover is insulated with 25 mm (1") of Armaflex insulation (Figure 4.2d).

4.2.2.2 Thermocouple and borehole positioning rack

A special string rack was designed and constructed to mount the thermocouples and to provide a means of centering and supporting the borehole. Figure 4.5 shows the string rack before its insertion in the tank. It consists of a PVC structure in which fishing wires are tightened to serve as guides for thermocouples.

a) Concrete poured to fill the curvature of the bottom of the tank.

b) Concrete “cake” on top of bottom insulation.

Figure 4.4: Concrete “cake” to fill the bottom curvature of the tank.

Figure 4.5: String rack.

The top and bottom portions of the rack (Figure 4.6a and b, respectively) are machined from 19 mm (3/4”) thick PVC plates in the form of a cross. The plates are held in place by four vertical posts made of PVC tubes (Figure 4.6-c).

a) Top of the string rack.

b) Bottom of the string rack with the borehole seat.

c) Vertical posts and their junctions.

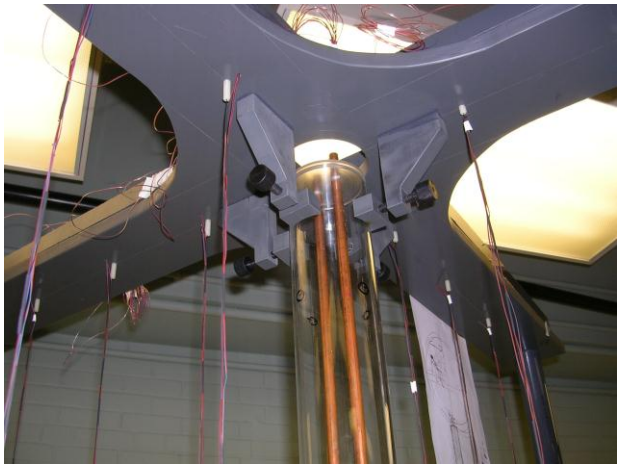

d) Top of the string rack showing the machined pegs to center and hold the borehole from the top.

Figure 4.6: Photos of the string rack construction.

Special joints were designed to make the connections strong enough to avoid twisting or swinging of the rack. The posts are located close to the tank outside diameter so as to avoid

a) String rack in the partially-filled sand tank.

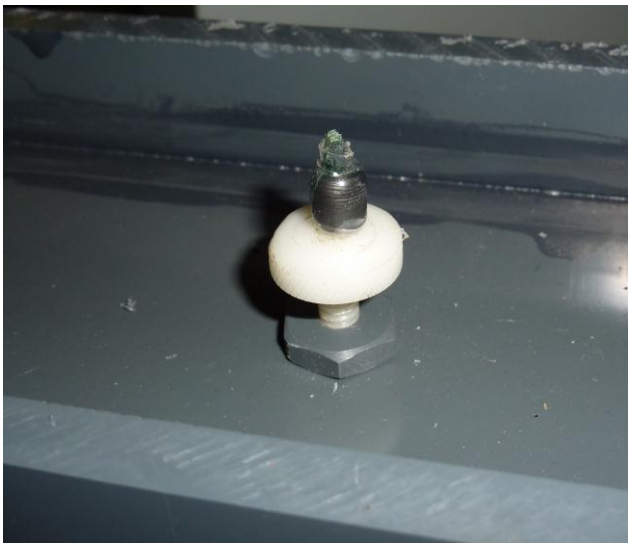

b) Tension peg for the fishing wires.

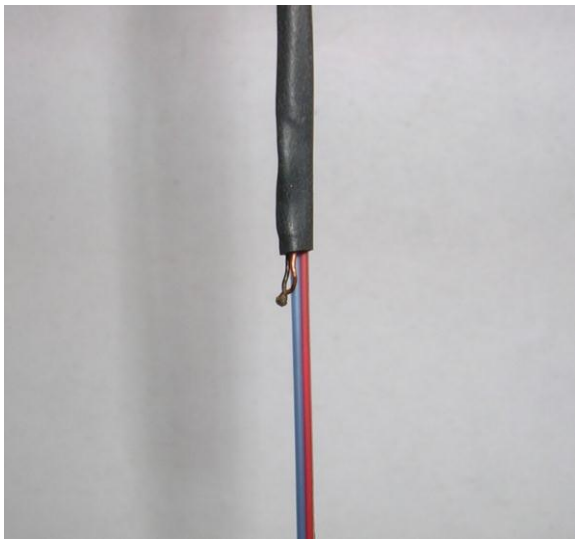

c) Thermocouple fixed on the fishing wire with a shrink tube.

Figure 4.7: Photos showing the fishing wires, a tension peg and the thermocouple fastening method.

thermal interference from the PVC tubes which have a slightly different thermal conductivity (0.19 W/m-K) than the sand (Figure 4.6-c).

The fishing wires are solidly fixed on the bottom of the string rack. The amount of tension can be controlled by tuning specially made tension pegs. These tension pegs can be seen on the top cross in Figure 4.7a and in a close-up photo in Figure 4.7b. As shown in Figure 4.7c, thermocouples are fixed to the fishing wires using shrink tubes which enables an accurate positioning of the thermocouples. With this set-up, it is estimated that the uncertainty in the position of the measuring tip of the thermocouple is ±1 mm. As shown in Figure 4.7a. there are a total of 12 vertical fishing wires (i.e., three radial positions in each of the four cross wings). In addition, thermocouples are also positioned on the borehole wall in the same plane as the fishing wires. On each fishing wire, there are four thermocouples located at four different vertical levels. From top to bottom, the first vertical row of thermocouples is at 10 percent (12.3 cm), the second row at 30 percent (36.9 cm), the third row at 50 percent (61.5 cm) and the last one at 90 percent (110.7 cm) of the active borehole length (123 cm). As shown in Figure 4.8e, the radial positions are as follows: the first one is on the borehole wall, i.e., at 3.81 cm from the borehole center, the second one at 15 cm and the third and fourth ones at 30 and 45 cm from the borehole center.

A three dimensional polar coordinates coding system, *R, θ, Z,* is used to specify the thermocouples and their positions. There are *R1* (on the borehole wall), *R2*, *R3* and *R4* as well as *Z1* (the first vertical row from top), *Z2*, *Z3* and *Z4*. The 0° wing is positioned at the same azimuthal angle as the inlet tube of the borehole. Thus, the 180° wing is located on the same azimuthal angle as the outlet tube and the 90° and 270° wings are perpendicular to the 0°-180° plane. More details on the position of the thermocouples are provided in Figure 4.8 as well as in Table 4.1.

Three Type-T thermocouples are fixed to the inner side of the tank as shown on the far right side of Figure 4.7a. Two of these thermocouples are located on the top and bottom while the third thermocouple is installed on the tank wall at mid-height. This last thermocouple is used to measure the so-called “far-field” temperature. Another Type-T thermocouple measures the ambient temperature. It is located on the blue cap on top of the tank (Figure 4.1b).

All thermocouples (except the *R3-270-Z3* which did not work properly at first but was fixed after calibration) were calibrated. The calibration procedure is presented in Appendix D. The calibration reveals that the uncertainty in the temperature measurement is ±0.35ºC.

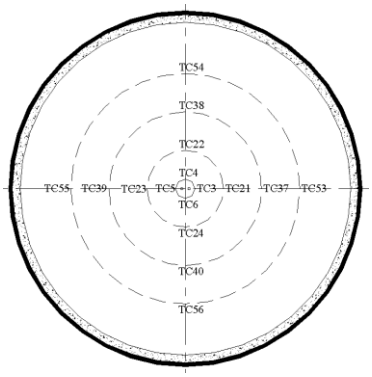

(a) Thermocouples at *Z1* for all radial distances.

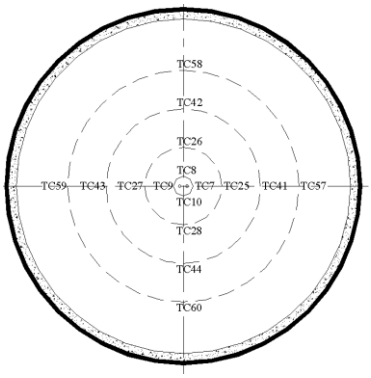

(b) Thermocouples at *Z2* for all radial distances.

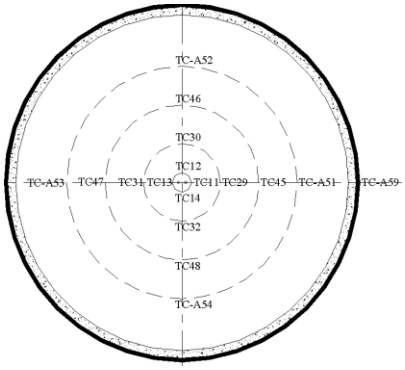

(c) Thermocouples at *Z3* for all radial distances.

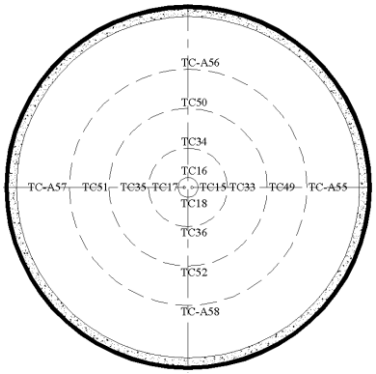

(a) Thermocouples at *Z4* for all radial distances.

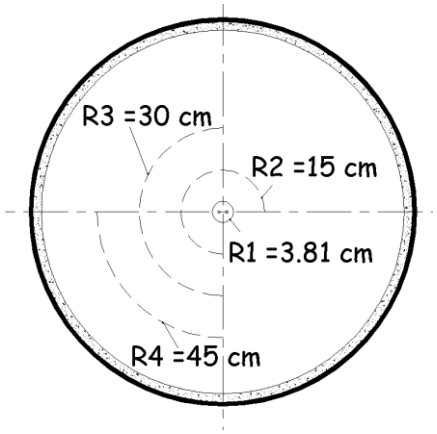

(e) Position of the radial distances (from the tank center).

Figure 4.8: Thermocouple numbering system.

Table 4.1: Coding system for all thermocouples.

Number	Channel Number HP 34970A		Reference Number
1	101		Thermistor#1
2	102		Thermistor#2
3	103		R1-0-Z1
4	104		R1-90-Z1
5	105		R1-180-Z1
6	106		R1-270-Z1
7	107		R1-0-Z2
8	108		R1-90-Z2
9	109		R1-180-Z2
10	110		R1-270-Z2
11	111		R1-0-Z3
12	112		R1-90-Z3
13	113		R1-180-Z3
14	114		R1-270-Z3
15	115		R1-0-Z4
16	116		R1-90-Z4
17	117		R1-180-Z4
18	118		R1-270-Z4
19	119		TC-U1
20	120		TC-U2

Number	Channel Number HP 34970A		Reference Number
21	201		R2-0-Z1
22	202		R2-90-Z1
23	203		R2-180-Z1
24	204		R2-270-Z1
25	205		R2-0-Z2
26	206		R2-90-Z2
27	207		R2-180-Z2
28	208		R2-270-Z2
29	209		R2-0-Z3
30	210		R2-90-Z3
31	211		R2-180-Z3
32	212		R2-270-Z3
33	213		R2-0-Z4
34	214		R2-90-Z4
35	215		R2-180-Z4
36	216		R2-270-Z4
37	217		R3-0-Z1
38	218		R3-90-Z1
39	219		R3-180-Z1
40	220		R3-270-Z1

Number	Channel Number HP 34970A		Reference Number
41	301		R3-0-Z2
42	302		R3-90-Z2
43	303		R3-180-Z2
44	304		R3-270-Z2
45	305		R3-0-Z3
46	306		R3-90-Z3
47	307		R3-180-Z3
48	308		R3-270-Z3
49	309		TC-FF at 0°
50	310		TC-TOP at 0°
51	311		R3-180-Z4
52	312		R3-270-Z4
53	313		R4-0-Z1
54	314		R4-90-Z1
55	315		R4-180-Z1
56	316		R4-270-Z1
57	317		R4-90-Z2
58	318		R4-180-Z2
59	319		R4-270-Z2
60	320		R4-0-Z2

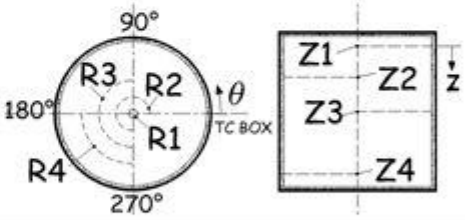

Auxiliary

Number	Channel Number HP 34970A		Reference Number
A-51	311		R3-0-Z4
A-52	312		R3-90-Z4
A-53	313		R4-0-Z3
A-54	314		R4-90-Z3
A-55	315		R4-180-Z3
A-56	316		R4-270-Z3
A-57	317		R4-0-Z4
A-58	318		R4-90-Z4
A-59	319		R4-270-Z4
A-60	320		TC-BT at 0°

4.2.2.3 Borehole

As mentioned earlier, the active length of the borehole is 1.23 m, about 1/100 the length of a real borehole. The same scale reduction could not be applied in the radial direction as this would have meant the use of a 1.5 mm (0.06 ”) diameter borehole. Instead it was decided to build a borehole as small as possible but large enough to be fabricated and instrumented properly. The borehole is a B-type borehole (i.e., there is the same distance of 19.05 mm between the pipes as between the pipes and the borehole wall as shown in Figure 4.9) made from a 76 mm (3”) outside diameter plexi-glass pipe in which a U-tube is inserted. The U-tube is made using a 9 mm (3/8” nominal) copper pipe with a 180º turn on the bottom. Details on the borehole construction can be found in Figure 4.9, Figure 4.10 and Figure 4.11. The U-tube is centered using the top and bottom caps (Figure 4.10b and c). Special spacers were designed and machined to keep a fixed distance between the downward and upward legs (Figure 4.10a). The verticality of the borehole was maintained using four centering pegs near the top of the borehole (Figure 4.10c). According to the nomenclature used in Figure 3.2, the borehole was installed in the tank such that $L1=L2$=6cm.

The choice of the filling material for the inside of the borehole proved to be challenging. Unlike real boreholes which are backfilled with grout after drilling and after the U-tube has been put in place, the present boreholes had to be prefabricated and then installed in the sand tank. Initially, it was decided to fill the borehole with a typical grout found in real boreholes which consists of a mixture of bentonite, sand and water. Grouts with higher bentonite content are harder while those with a higher sand content are more fragile but have higher thermal conductivity A series of preliminary tests for fabricating the borehole were performed using four different common grout recipes which contained different relative percentages of the three grout ingredients. Borehole prototypes were casted in waxed cardboard tubes. After a drying period of six to eight weeks, the cardboard tubes were removed. Unfortunately, none of these four prototypes proved to be satisfactory as most of them had several cracks which compromised the grout uniformity. Finally, a decision was made not to fill the borehole with a regular grout but to use fine glass beads (Figure 4.11b) which provided an homogeneous filling material, albeit, as shown in Table 4.2, with a relatively small thermal conductivity. Table 4.2 summarizes the thermal conductivities of the various materials composing the borehole. Based on the procedure proposed by Remund, it can be shown that the effective borehole thermal resistance is 0.61 m-K/W. With a heat transfer rate of 22.5 W/m (see Chapter 5) this leads to a temperature difference between the mean fluid

temperature and the borehole wall inside diameter of 13.75 K. This borehole thermal resistance value is higher than what is expected in a regular borehole (from 0.05 to 0.2 m-K/W). It is attributable to the relatively low thermal conductivities of the glass beads.

Table 4.2: Thermal conductivities of the main components of the borehole.

Material	Thermal conductivity (W/m-K)
Plexi-glass	0.2
Copper	400
Glass beads (dry at 61ºC)	0.35

On the borehole wall (at *R1*) a total of 16 T-type thermocouples are installed, four at each azimuthal orientation (Figure 4.11a). To install the thermocouples on the borehole wall, the thermocouples tips were inserted inside tiny holes and then fixed permanently using Epoxy glue. During the installation of these thermocouples, the ones installed at *R1-0-Z3* and *R1-270-Z4* broke. They were re-welded and re-glued but could not be recalibrated. Before insertion of the string rack in the sand tank, the borehole is installed on its seat (Figure 4.11c).

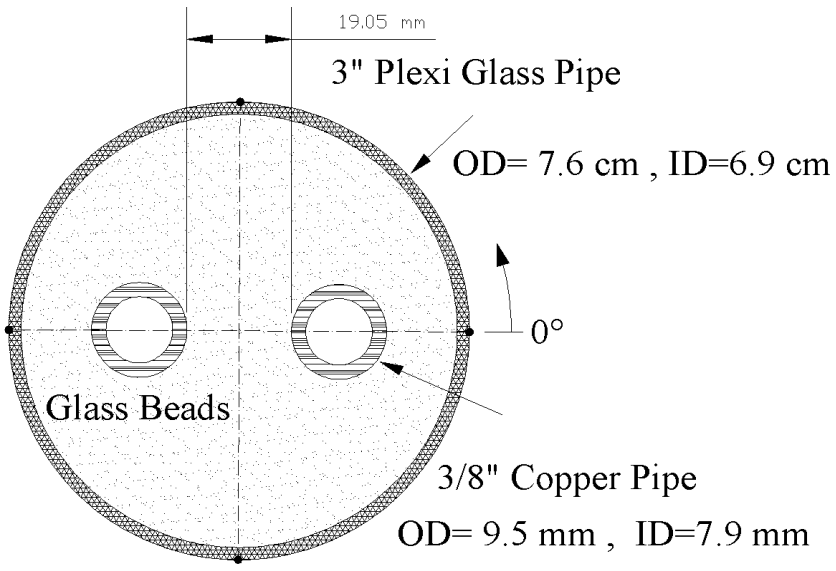

Figure 4.9: Cross-section of the borehole used in the sand tank.

a) U-tube with spacer.

b) Top cap of the borehole which positions the U-tubes properly.

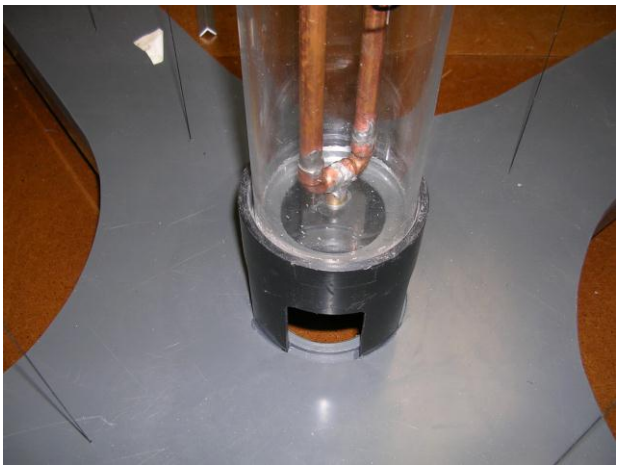

c) Seat of the borehole and the bottom cap on which the U-tube is centered from bottom.

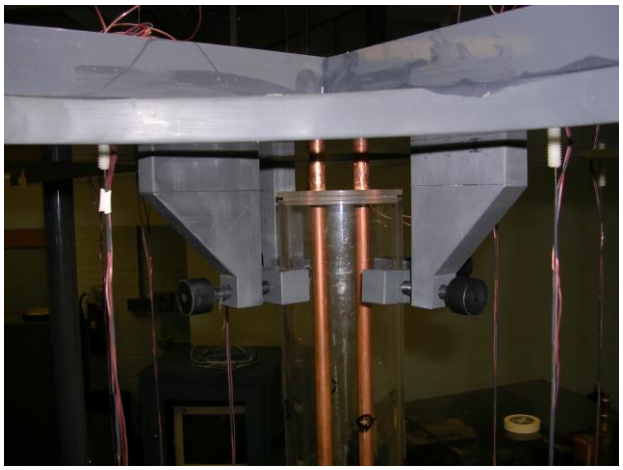

d) Centering the borehole from top, using four centering pegs.

Figure 4.10: Photos showing various parts of the borehole.

a) Borehole with surface thermocouples, ready to be filled with glass beads.

b) Borehole filled with glass beads, ready to be installed on the string rack.

c) Borehole positioned in the center of the string rack.

Figure 4.11: Photos from the borehole and string rack.

4.2.2.4 Tank filling

The tank had to be filled with a homogeneous material with known (or easily measureable) thermo-physical properties. The choice of this substance had to be realistic and not far from common ground/soil materials found in nature. Besides minerals and organic matter, typical soils contain moisture which is difficult to maintain constant during experiments. Uniform compactness of the soil was another concern. Finally laboratory-grade sand, known as Ottawa sand type C-109, was chosen to act as the "ground". It is almost entirely composed of natural silica (SiO_2). The particles are fine and uniform in size and shape. The thermal properties and physical characteristics of the Ottawa sand have been documented by Tarnawski et al. (2009, 2011). These properties, such as thermal conductivity and density, depend on the porosity (i.e., volume of voids over the total volume) of the sample as reported by Farouki (1981). According to Tarnawski et al. (2009), the porosity of the Ottawa sand may vary from 0.32 to 0.4. The porosity of the sand sample used in this study was determined to be 0.36. The corresponding thermal properties are presented in Table 4.3. The thermal conductivity is relatively small which means that high fluid temperatures in the borehole are required to have a significant amount of heat transfer and have a measurable temperature difference between the inlet and outlet fluid temperatures.

Table 4.3: Thermal properties of the Ottawa sand (C-109) for a porosity of 0.36.

	Thermal conductivity W/m-K	Thermal diffusivity m^2/day
Dry sand	0.29	0.0198

The experiments reported here were conducted with dry sand. However, it would be possible to fully saturate the sand with water in future experiments.

4.2.3 Data Acquisition System

An *Hp-34970A* data acquisition system is used. It is equipped with three module cards (*HP-34901A*) which provide 20 inlet channels each. The system is connected to a personal computer having a GPIB card (*HP-82350 PCI*) for transferring the data. A computer program for the data acquisition system was developed based on the Agilent BenchLink Data Logger Pro Software Version 1.0. The number of available channels is 60 while the total number of measurements is 70. Therefore, less crucial measurements, identified as "auxiliary" in Table 4.1, were left aside in most experiments, but could be reactivated by switching the measurements (at the TC junction box shown in Figure 4.1) from 51 to 60 for the auxiliary measurements (A-51 to A-60). The measuring chain from the thermocouple tip to the module cards was kept intact from the calibration to the final experiments. The recording rate is every 10 seconds and the data is used as is without further averaging. It should be mentioned that each card has a built-in thermocouple reference junction called *isothermal block* which is an electrical insulator but a good heat conductor. Accurate temperature measurements can be made once the temperature of the isothermal block is known. A temperature sensor mounted to the isothermal block measures its temperature.

4.3 Preliminary experiments

Some preliminary experiments were performed to examine the overall performance of the experimental apparatus and to verify its thermal response. In this section, the experimental data from one such preliminary experiment are presented. The objectives of this preliminary experiment were:

a) To verify the functionality of the whole experimental apparatus under regular/expected experimental situation;

b) To spot and possibly fix the probes that did not function properly;

c) To test the data acquisition system under a long duration of experiment;

d) To verify the response of the experimental apparatus to transient effects such as non-constant inlet fluid temperature and variable flow rate;

e) To observe the transient heat transfer effects and the radial heat front penetration depth;

f) To verify the evolution of the ambient temperature in the lab during a typical test and examine the diurnal variations.

One early finding was that heat losses from the bath and the connected pipes and filter was significant and translated into a significant temperature drop from the bath to the borehole. Insulation was added to the equipment to reduce these heat losses.

As shown in Figure 4.12, this experiment ran for a total 91 hours with 24.63 hours of heat injection followed by heat recovery period which lasted until the end of the test. During the heat injection period, the target outlet temperature from the bath and volumetric flow rate were 70°C and 0.005 L/s, respectively. For reasons which will be explained shortly, the flow decreased gradually until reaching a value close to zero and then the flow rate was increased manually up to 0.013 L/s at t = 20.33 hr.

Figure 4.12 shows the temporal evolution of the inlet and outlet fluid temperature (thermistors were still functional at this stage), the sand temperature at 0° and *Z2* for all the four radial distances as well as the volumetric flow rate. Although the target (i.e., bath) temperature is set at 70°C for the whole heat injection period, it can be seen that the inlet fluid temperature and flow rate are continuously decreasing until t = 20.33 hr. This is due to the presence of air bubbles in the piping system which have blocked the fluid passage and gradually reduced the fluid flow to the borehole. This malfunction prompted the use of an air vent on the piping system which solved this problem. It should be noted that as the flow rate decreases, the fluid residence time increases as well as the heat losses from the piping system.

As mentioned earlier, the constant temperature bath worked at a relatively high temperature (≈70°C) which meant that there was significant evaporation from the bath and that it had to be refilled during testing. After starting the experiment, at t = 2.33 hr, one liter of water at room temperature was added to the constant temperature bath which caused a slight temperature drop of the inlet and outlet fluid temperatures. It took the constant temperature bath about 5 minutes to stabilize at the set point temperature (a zoomed portion of the figure at t = 2.33 hr would show this effect). After the overnight period, four liters of water were gradually poured into the bath to compensate evaporation without interrupting the test. Adding water to the bath using this batch technique was found to be problematic as an operator has to be present in the lab to add water to the bath during the experiments which is not feasible for long experiments which last days and

run overnight. Clearly, there was a need to install a device that could compensate the lost fluid at the same pace it evaporated. The fluid compensation tank with its regulating dropper was designed and added to the experimental apparatus to solve this issue.

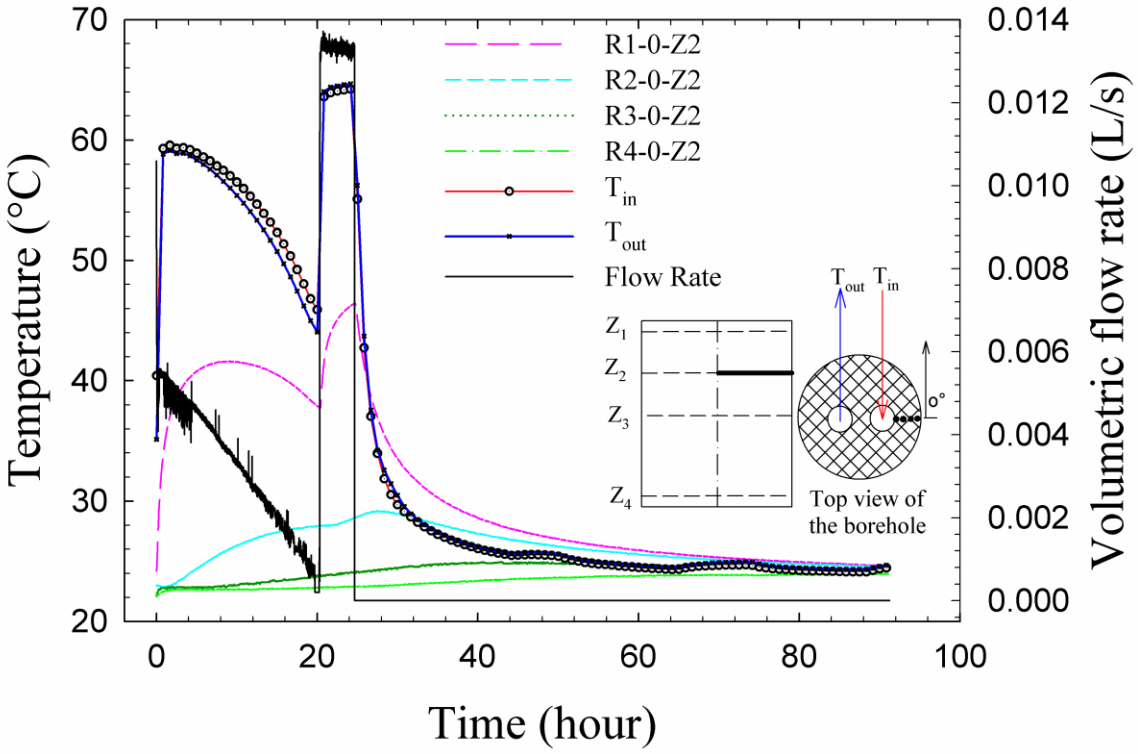

Figure 4.12: Various temperatures and volumetric flow rate obtained during a preliminary experiment.

One general observation from Figure 4.12 is that when the inlet fluid temperature varies, the same trend is observed in the other temperature measurement spots with some time delay depending on the radial distance; the closer the thermocouple to the borehole, the faster its response. At t = 20.33 hr, the flow rate was suddenly increased from an almost no flow condition to a flow rate of 0.013 L/s. This leads to a sudden change in the inlet-outlet fluid temperatures. The response of the *R1-0-Z2* thermocouple to this change is relatively fast, however the response of the thermocouple located at *R2-0-Z2* is observed with some delay as a result of the small sand thermal diffusivity. The temperatures keeps increasing from t = 20.33 hr to the end of the heat injection period (t = 24.63 hr). The difference between the borehole wall temperature (measured

on the outside wall) and the mean fluid temperature is approximately 20 ºC just before the end of the heat injection period. This shows that the borehole thermal resistance is relatively high as mentioned earlier.

The *R1-0-Z2* measurement reaches its peak a few minutes after the end of the heat injection period which indicates that the heat front takes some time to travel from the fluid to the borehole wall and the fact that the borehole has not reached steady state yet. The *R2-0-Z2* temperature reaches a peak about 3-4 hours after the heat injection has stopped. This is a significant outcome of this preliminary experiment as it shows that the heat front takes 3-4 hours to travel the 11.2 cm separating *R1* from *R2*. Also interesting are the evolutions of the temperatures measured at *R3-0-Z2* and *R4-0-Z2* which show mild steady increases and no significant peaks. One major conclusion drawn from this test is that the heat injection period would have to last several days in order to see significant temperature changes at *R3* and *R4*.

Towards the end of the test, after a recovery period of close to 67 hours, the temperatures at *R1*, *R2*, *R3*, and *R4* tend towards the same value indicating the approximate amount of time required to reach an equilibrium temperature after a heat injection period.

During the heat recovery period, the measurements of T_{in} and T_{out} tend towards the ambient temperature as there is no flow in the pipes. One can see that the ambient temperature is not constant as these two temperatures experience small bumps. As will be shown in the next chapter, ambient temperature fluctuations also influence the boundary conditions on the tank wall.

CHAPTER 5 EXPERIMENTAL VALIDATION

5.1 Introduction

Following the preliminary experiments presented in Chapter 4, this chapter presents the results of the final experimental test which is characterized by a 73 hour heat injection period followed by a 5 day recovery period without any fluid flow to the borehole. This chapter is divided into two main parts. First, the experimental results are presented and analyzed. Then, these results are compared to numerical results obtained from the two-dimensional model presented in Chapter 3. It is also hoped that the experimental data could be used by other researchers to validate their borehole or ground models.

5.2 Experimental results

The sand tank was first allowed to reach an equilibrium conditions before the actual start of the test. This initial condition was measured and is presented in Figure 5.1 in the form of isotherms obtained from temperature measurements in the 90° plane. As shown in this figure, the temperature inside the tank is relatively uniform with an average value of 23.65 ± 0.3 °C. There is a slight stratification which is probably caused by the stratification in the ambient air surrounding the tank.

The actual test started on June 14, 2011 at 14:37 and lasted eight days with 73 hours of heat injection followed by a 5 day recovery period during which no fluid was pumped in the borehole. The test was to be performed with a constant inlet temperature and a constant flow rate through the heat injection period. The volumetric flow rate was set to a value that would ensure close to a 1°C temperature drop between the inlet and outlet fluid temperatures. Thus, if required, the amount of power injected in the borehole could be evaluated with a reasonable accuracy. The inlet temperature was set to a relatively high temperature (nominal value of 67.5°C with a corresponding bath temperature of 70°C) to ensure that a maximum amount of heat would be transferred throughout the heat injection period. Figure 5.2 presents the values of the inlet and outlet fluid temperatures, the volumetric flow rate, and the far field as well as the ambient temperatures during the heat injection period.

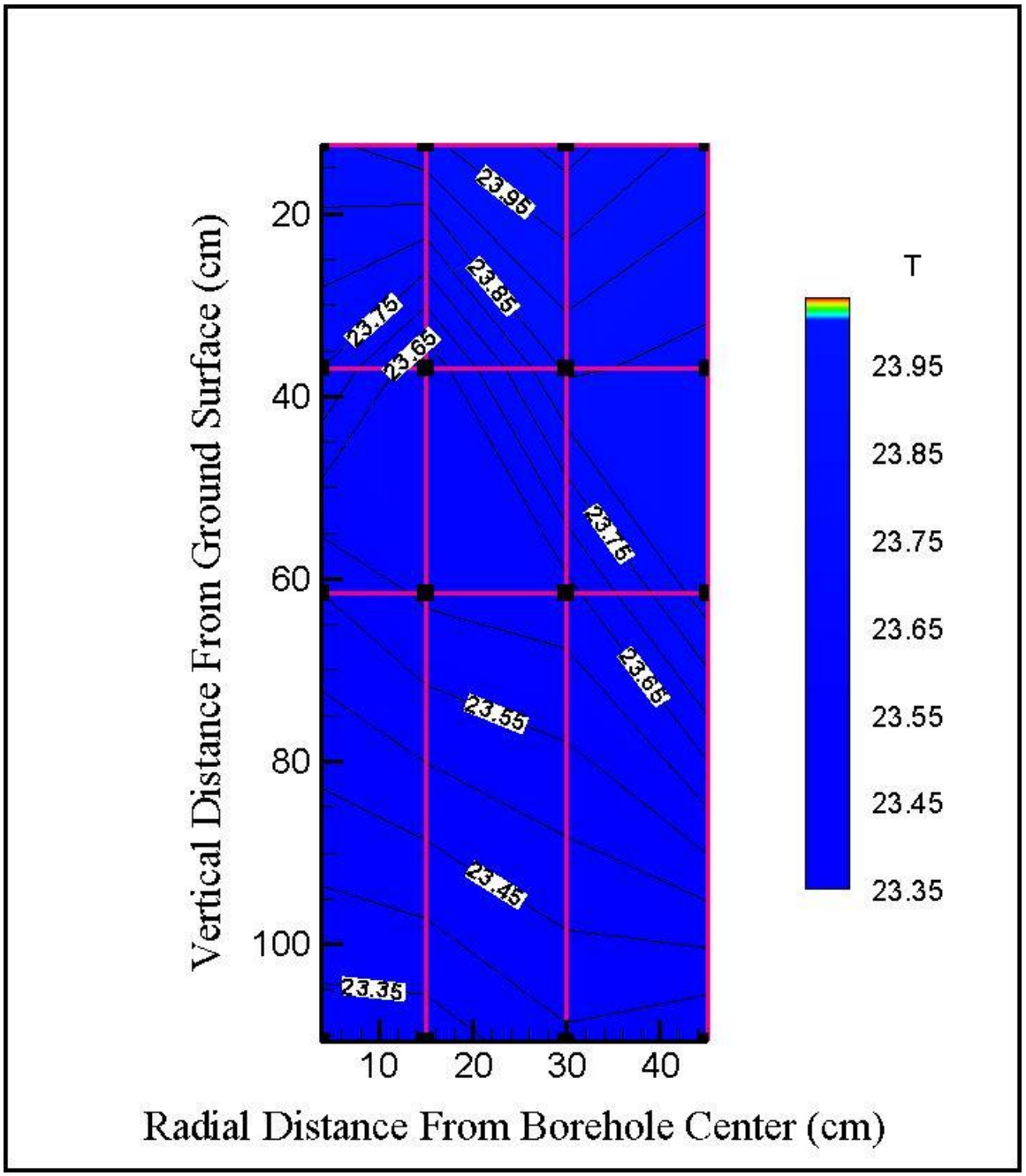

Figure 5.1: Isotherms showing the initial state of the temperature in the sand tank.

As shown in Figure 5.2, the inlet temperature (TCI-IN) remains somewhat constant at around 67.5°C with a slight temperature increase (approximately 0.2°C over the 73 hour heat injection period). This temperature increase is probably due to an increase in ambient temperature which reduces the amount of piping heat losses from the constant temperature bath to the actual inlet to the borehole. During the first few minutes of the heat injection period, the measured outlet fluid

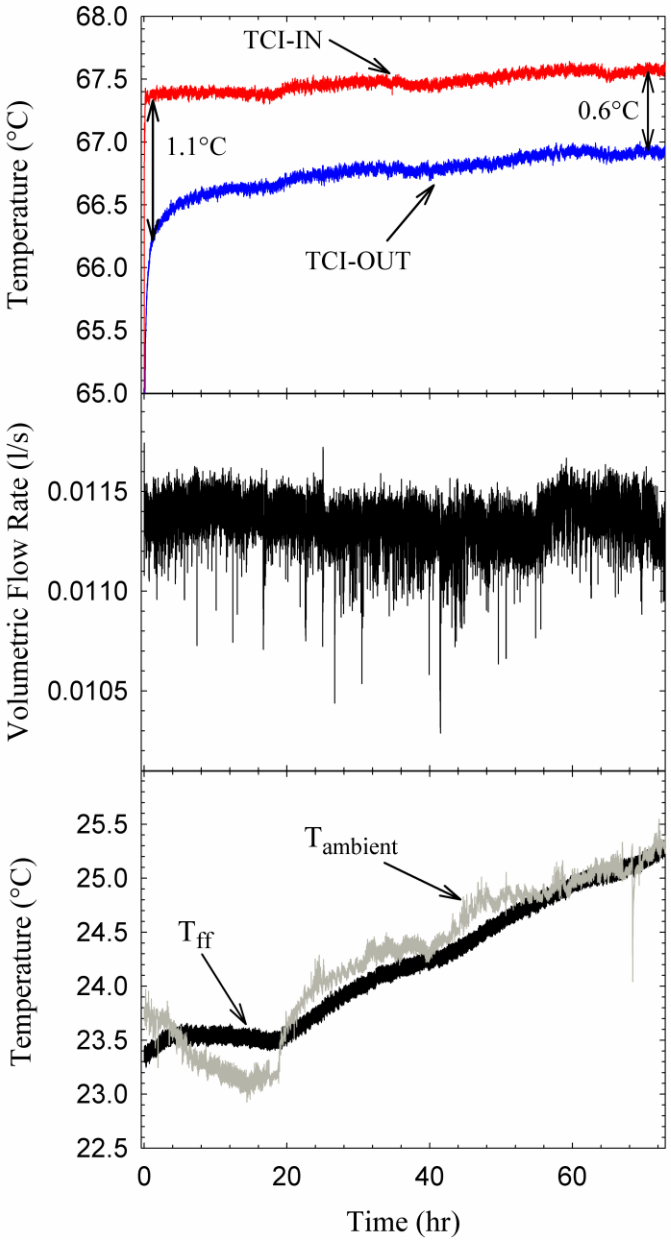

Figure 5.2: Measurements during the heat injection period. Inlet and outlet fluid temperature (top); volumetric flow rate (middle); ambient and far-filed temperatures (bottom).

temperature (TCI-OUT) increases significantly from the initial tank temperature to a value around 66.5°C.

As mentioned in Chapter 4, this indicates that the borehole thermal resistance as well as the relatively poor sand thermal conductivity lead to poor heat transfer from the fluid to the sand. As

indicated in the figure, the difference between the inlet and outlet fluid temperatures is approximately 1.1°C after ninety minutes. This difference diminishes to a value around 0.6°C towards the end of the test. Assuming a mass flow rate of 0.011 kg/s and a specific heat of 4.2 kJ/kg-K, this leads to a variable (declining) heat transfer rate of 50.8 and 27.7 Watts after 90 minutes and 73 hours, respectively. The corresponding heat transfer rates per unit length are 41.3 and 22.5 W/m.

As shown in the middle graph in Figure 5.2, the measured volumetric flow rate was relatively constant throughout the test period. The average value over the 73 hour period is 0.0114 L/s. The fluctuations can be quantified using the standard deviation which is 0.00011 L/s in the present case. Thus, the flow rate fluctuations are of the order of ± 1%.

The bottom part of Figure 5.2 presents the measured ambient temperature as well as the so-called far-field ground temperature. Recall that the far-field temperature is measured at the mid-height of the tank on the inside tank wall while the ambient temperature is measured near the tank as shown in Chapter 4. As shown on the figure, the ambient temperature increased by about 2 °C over the 73 hour test period. The far-field temperature shows the same upward trend. These unwanted variations result from the fact that the lab is not conditioned and, therefore, its temperature cannot be maintained constant. This has implication when comparisons are made with numerical simulations with constant boundary conditions. This will be discussed further later in this chapter. Overall the test conditions are judged to be satisfactory.

5.3 Experimental results

Figure 5.3 and Figure 5.4 show the temporal evolution of the temperature at all the measuring points inside the sand tank over the eight day period. Each column contains four graphs each for a specific azimuthal orientation. On each of these four figures, the top graph shows the temporal evolution of the temperature on the borehole wall, at *R1*, for all values of *Z*, while the bottom graph shows the same type of curves at the radial distance *R4*. The two middle graphs show values at radial distances *R2* and *R3*, respectively. The reader should refer to the top graph in Figure 5.4d for an indication of the temperature measurement positions. As indicated in chapter 4, due to limitations on the available channels on the data acquisition system, there are no recorded temperature measurements at *R4-270-Z1*, *R4-270-Z2*, *R4-270-Z3*, *R4-270-Z4* and *R3-270-Z4*. It should also be noted that thermocouple *R2-90-Z2* is faulty (Figure 5.4a)

Colors and line types have been used in those figures to distinguish the various curves. As shown in the legend, the solid black lines with a diamond symbol (the symbol itself is positioned at t = 50 hours) represent the temperature curves for the thermocouples positioned at *Z1*, the long dash grey lines with a circle symbol (positioned at t = 80 hours) are for *Z2*, the short dash red lines with a star (positioned at t = 80 hours) are for *Z3* and the dotted blue lines with a cross symbol (positioned at t = 90 hours) are for *Z4*.

The first observation is that even after 73 hours of heat injection the sand temperatures are still increasing even though the fluid temperature is more or less constant. Steady-state has not been reached. From Figure 5.3 and Figure 5.4 it can be seen that at a certain radial distance, regardless of the azimuthal orientation or the vertical height, the shape of the temperature curves are similar. For example, one can notice from the top graphs in Figure 5.3a and Figure 5.4a (i.e., at *R1* for all vertical positions and angles), that the curves exhibit an exponential-like temperature rise at the beginning of the heat injection period followed by a relatively linear temperature increase reaching a sharp peak almost at the end of the heat injection period. This is followed by a steep decrease in temperature almost immediately after the end heat injection period and then by a relatively smooth temperature decrease towards the end of the recovery period.

At *R2*, (the second row of graphs from the top) the curves show a less steep temperature increase at the beginning of the heat injection period. However, right before reaching the peak, the curves show a steeper temperature increase than for *R1*. Similar to the curves for *R1*, the peaks have a pointed shape regardless of the azimuthal orientation or vertical height.

The curves for *R3* and *R4* show a small plateau of constant temperature at the beginning of the test. This is to be expected as the injected heat takes time to reach the radial distances *R3* and *R4*. After this plateau, the temperature shows a gradual increase but not as steep as for the *R1* and *R2* cases. The peak temperature occurs a few hours after the end of the injection period, again because the heat front takes several hours to reach *R3* and *R4*. The peak is also rounder than for *R1* and *R2*.

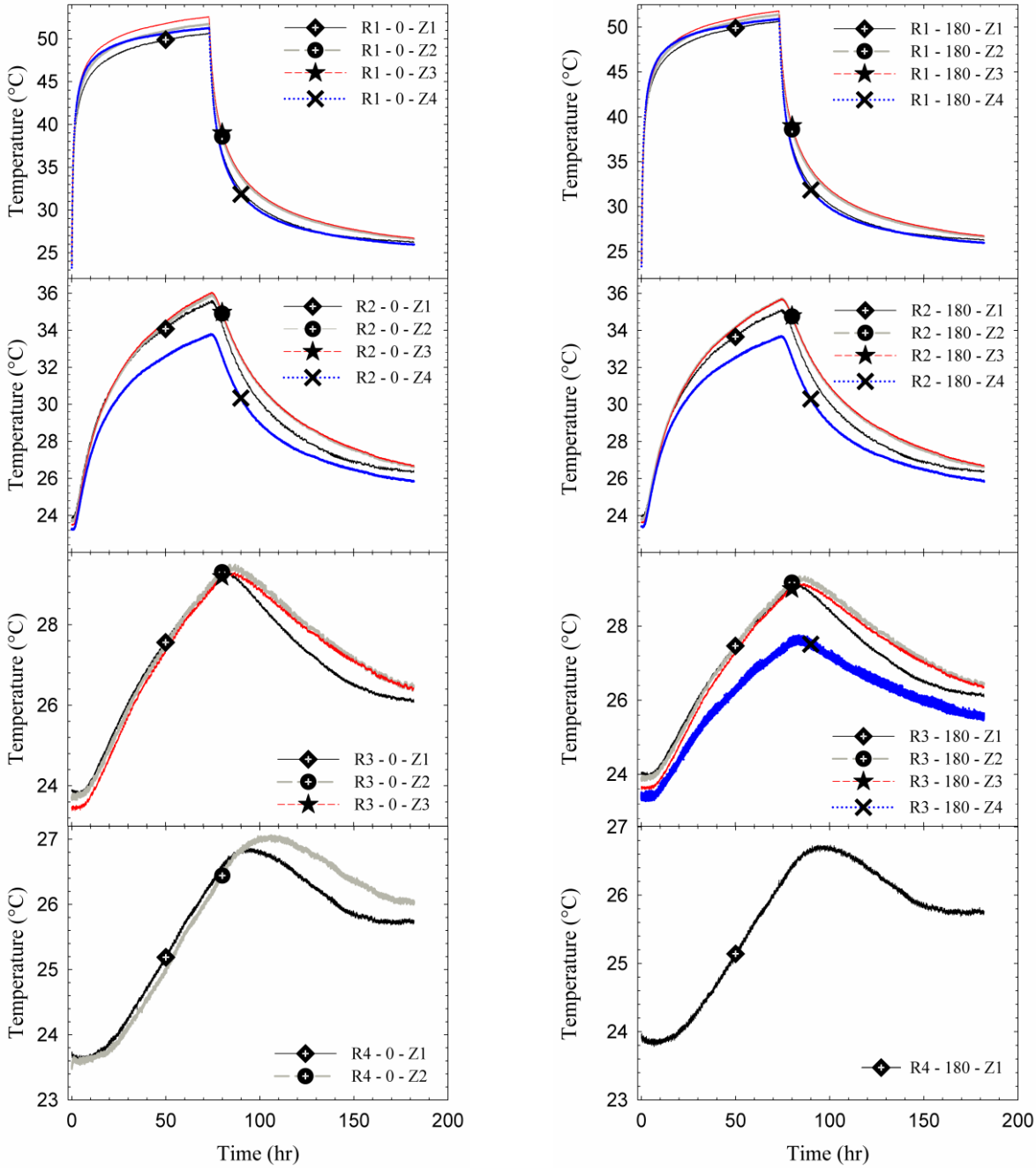

(a) 0° (b) 180°

Figure 5.3: Temporal evolution of temperature for azimuthal angles 0° and 180°

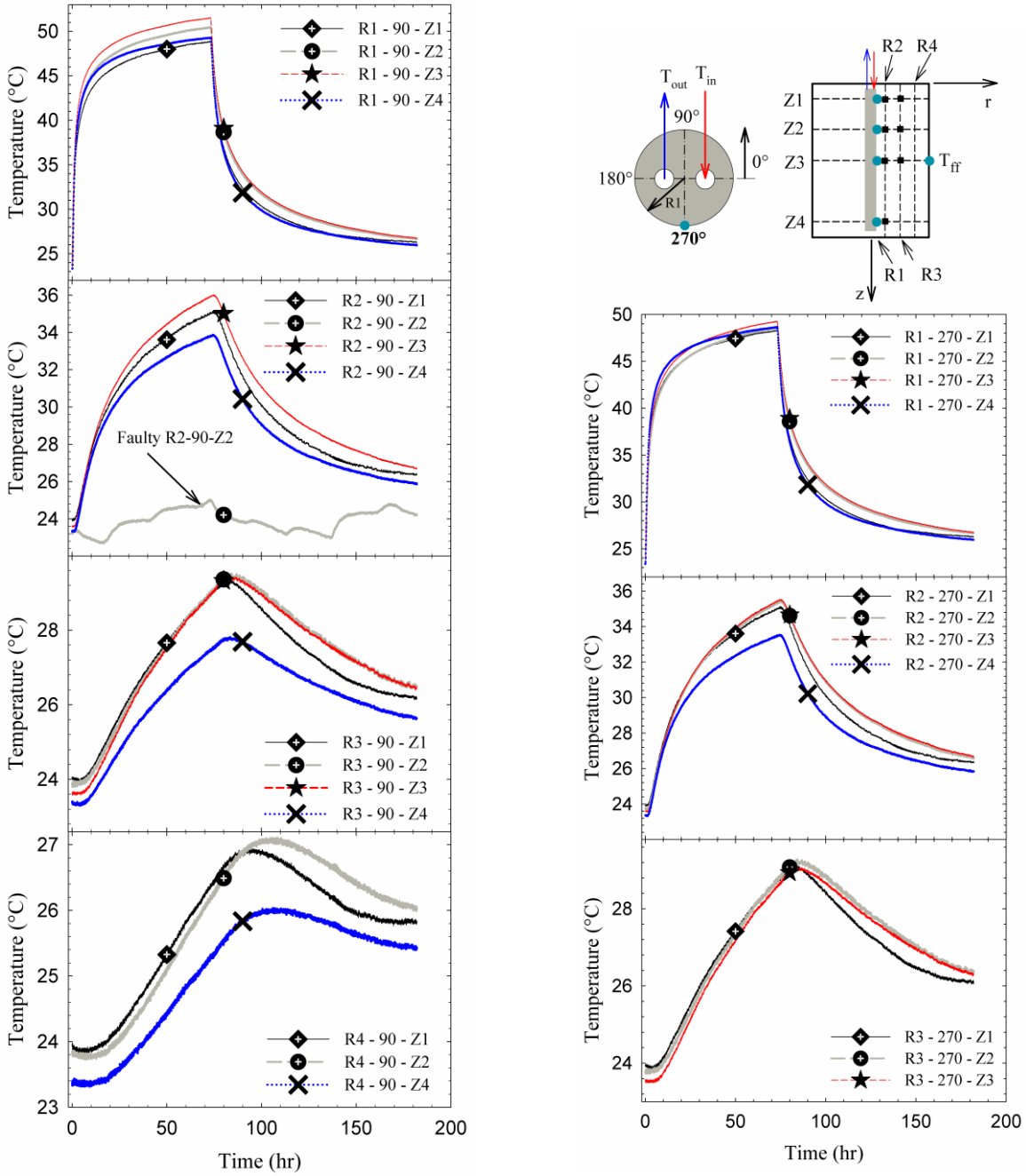

(a) 90° (b) 270°

Figure 5.4: Temporal evolution of temperature for azimuthal angles 90° and 270°

Not surprisingly, the highest temperatures occur on the borehole wall (*R1).* At *R1* and for a given axial position (*Z*), there are some differences among the four azimuthal temperatures. These differences will be explored later in this chapter. At *R1* and for a given azimuthal position, the maximum temperature occurs at the mid-height of the tank (i.e., at *Z3*) with slightly lower temperatures towards the ends of the borehole at *Z1* and *Z4*. This is to be expected as the temperature measurements at *Z1* and *Z4* are influenced by the top and bottom boundary conditions. In other words, heat is trapped in the middle height of the sand tank as it is far from the top and bottom boundaries through which heat is lost.

It can also be observed that at the end of the experiment during the recovery period, the measured temperatures at different radial and vertical distances are gradually converging towards a certain value indicating an equalization of the tank temperature at a temperature higher than the initial sand temperature (23.65 ± 0.3 °C).

The same experimental data can also be presented in the form of two-dimensional (*z-r*) plots with isotherms at different times. Such plots are presented in Figure 5.5 to 5.8 for t = 1, 72, 80, and 182 hours, respectively. The isotherms were drawn based on 16 temperature measurements which are identified by small solid black squares located at the intersection of the grid lines. The 16 temperature measurements are taken in the 90 º plane with two exceptions at *R4-90-Z3* and at *R2-90-Z2*. In the first case, the *R4-90-Z2* measurement was used instead of the *R4-90-Z3* measurement. This can be justified by looking at Figure 5.3 and Figure 5.4 which show that temperature measurements at *Z2* and *Z3* are nearly identical. For the same reason, it is logical to replace the readings of the faulty thermocouple located at *R2-90-Z2* by the *R2-90-Z3* measurement.

In general, the measurements show a regular behavior. After one hour of heat injection (Figure 5.5), the heat front has barely reached the thermocouples positioned at *R2* as the temperature has increased from an initial temperature of 23.65 °C to a value of approximately 24 °C. As the test progresses the heat front is moving towards the outer radius of the tank. After 3 days (Figure 5.6), the isotherm lines show an elliptic-like curvature which is characteristic of a radial-axial heat transfer from a cylinder. This will be studied further later in this chapter. In general, the highest temperatures are measured in the middle of the tank away from the top and bottom tank boundaries.

Figure 5.7 and Figure 5.8 show the isotherms during the heat recovery period at t = 80 and 182 hours, respectively. During the heat recovery period, the injected heat dissipates in the tank and the temperature tends towards the same temperature at all measuring points. At t = 182 hours, the sand tank temperature is relatively uniform but has reached a temperature higher than the initial sand temperature.

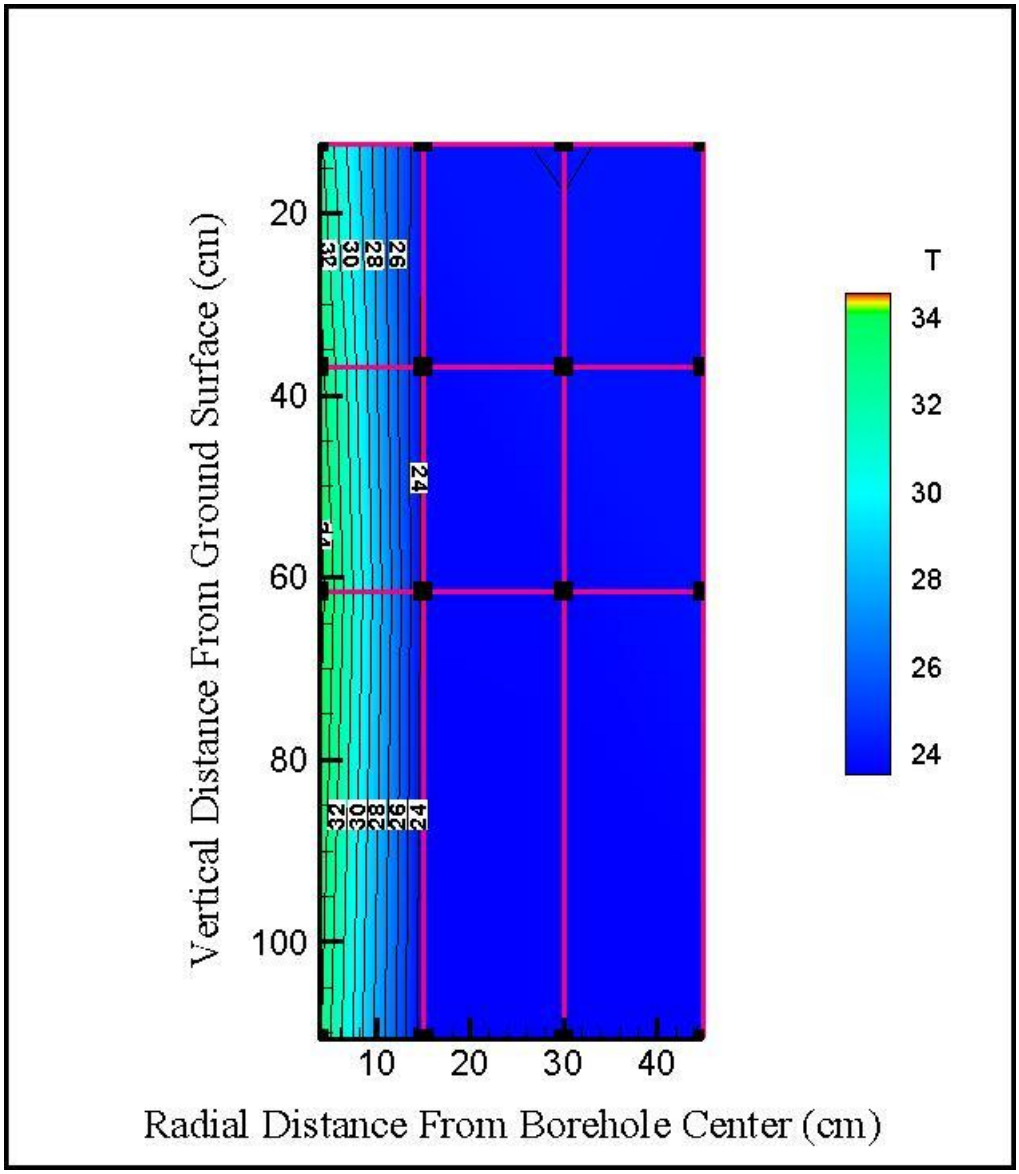

Figure 5.5: Isotherms at t = 1 hour.

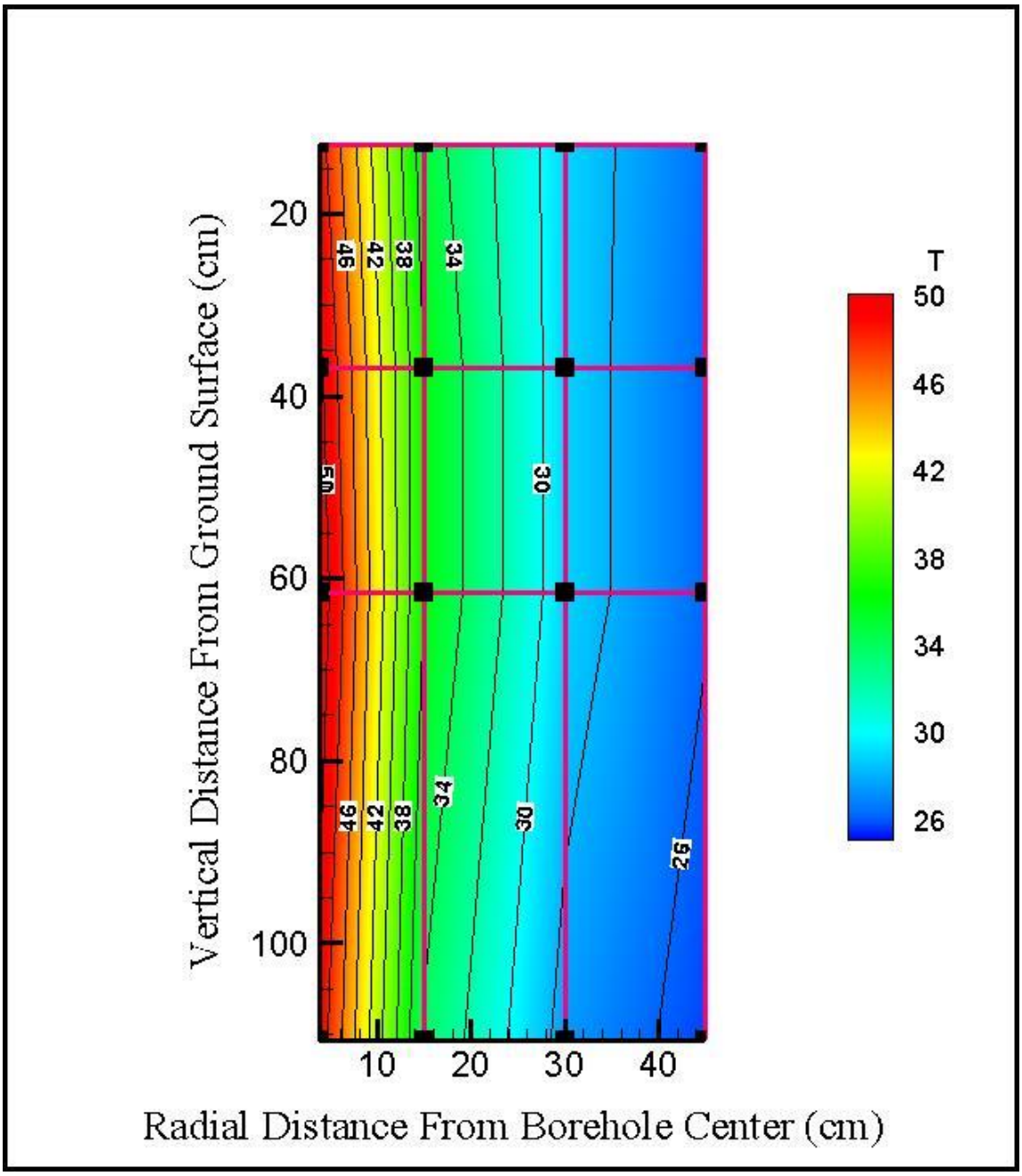

Figure 5.6: Isotherms at t = 72 hours.

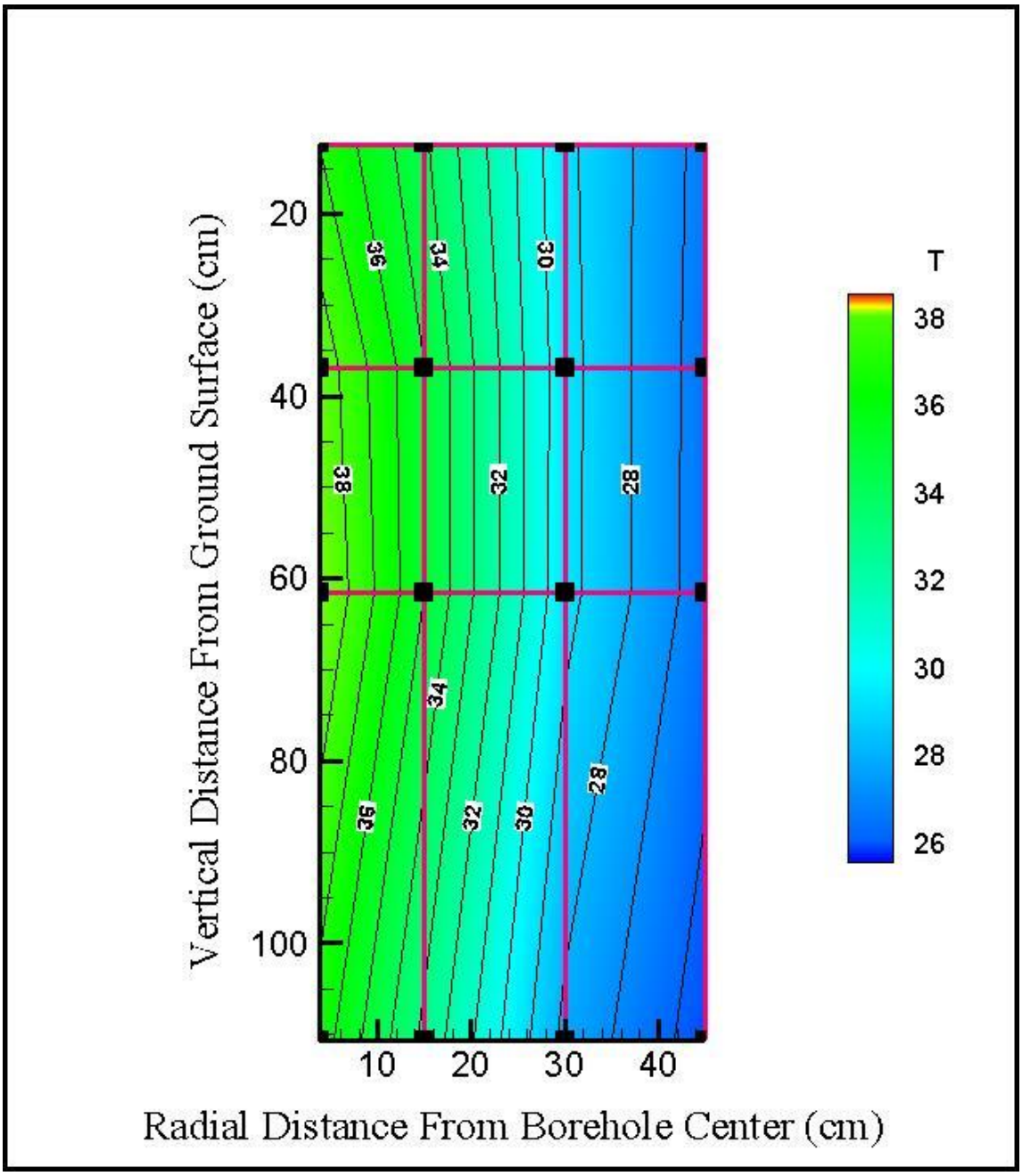

Figure 5.7: Isotherms at t = 80 hours (7 hours after the end of the injection period).

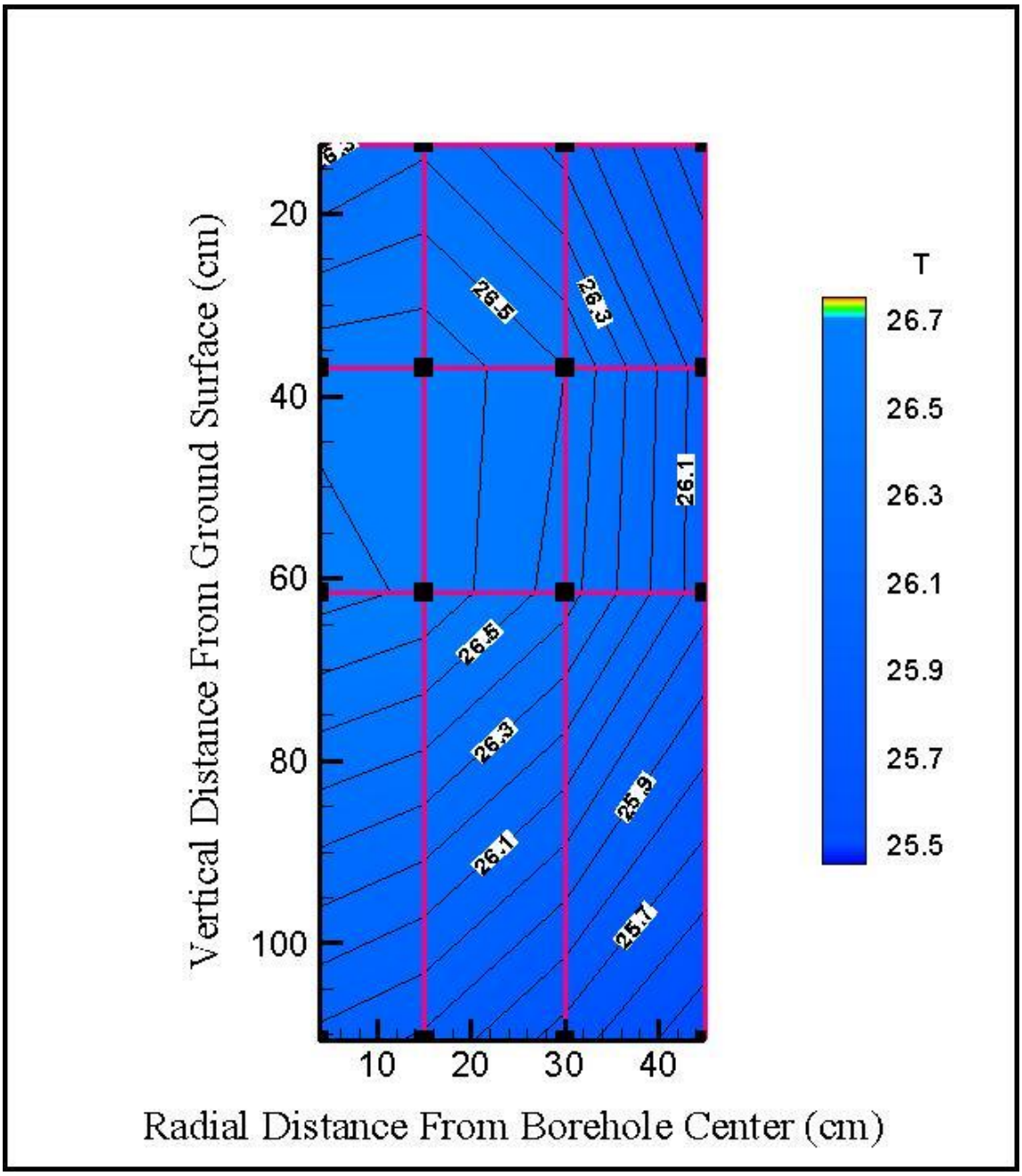

Figure 5.8: Isotherms at t = 182 hours.

The azimuthal variation of temperature at the borehole wall, *R1*, is presented in Figure 5.9a for different heights and specific times from the start of the heat injection period (15, 30, 45, 60 and 120 minutes). There are 5 data points in each of these figures; the 0° and 360° data points are the same. These points have been connected to each other by a spline fit.

Figure 5.9a shows that there are significant azimuthal temperature variations at the borehole wall with a difference of the order of 5 K between the highest and lowest temperatures. The highest temperatures are always at 0° followed by those at 180°. This is to be expected as the inlet pipe is closer to the 0° measurement while the 180° measurement is close to the outlet pipe as shown in the top drawing of Figure 5.9-b. It is to be noted that the temperature profiles exhibit a relatively good symmetry for *Z1* and *Z4*. For *Z2* and *Z3*, the symmetry is not as good with temperatures at 270° lower (by about 1 ºC) than on the opposite side at 90°. In a recent article, Claesson and Hellström (2011), revised the multipole method and determined the borehole wall azimuthal temperatures. They proposed that the temperature field induced by the heat rate from the pipes is not identical around the borehole wall perimeter. They also stated that the magnitude of these variations decreases at farther radial distances from the borehole. Even though the conditions are different, they showed a similar "double-wave" azimuthal profile and the results presented in Figure 5.9 are in qualitative agreement with theirs findings. In Figure 5.9-b, the temperature profiles are presented at the end of the heat injection period (i.e., at t =73 hours) for all vertical heights and angles for *R1*, *R2* and *R3*. From this figure, it can be seen that the azimuthal variation of the measured temperature is less significant further away from the borehole. For example, at *R3*, the temperature difference among the four data points is less than 0.5 °C for a particular value of *Z*.

Figure 5.9b shows that the highest temperature at the end of the heat injection period at *R1* and *R2* is reached at the mid-height of the sand tank (i.e., *Z3*) at 0°. For these two radial distances, this observation can be generalized to all corresponding points at other angles as well. At *R3*, the profiles show uniform (less sinusoidal-shape and more linear) temperatures. Surprisingly, for *R2* and particularly *R3* (i.e., the middle and bottom figures), the trend is not in agreement with that of *R1*. For example, at 90°, *R1* profiles show valleys (i.e., relative minimums) while peaks can be seen for *R2* and *R3*. The temperature range shown on the vertical axis of Figure 5.9b should also be taken into account. For instance, at *R3* (bottom figure), the *Z1, Z2* and *Z3* profiles show very small temperature differences at all angles. In other words, at *R3*, the profiles show more uniform (less sinusoidal-shape and more linear) temperatures.

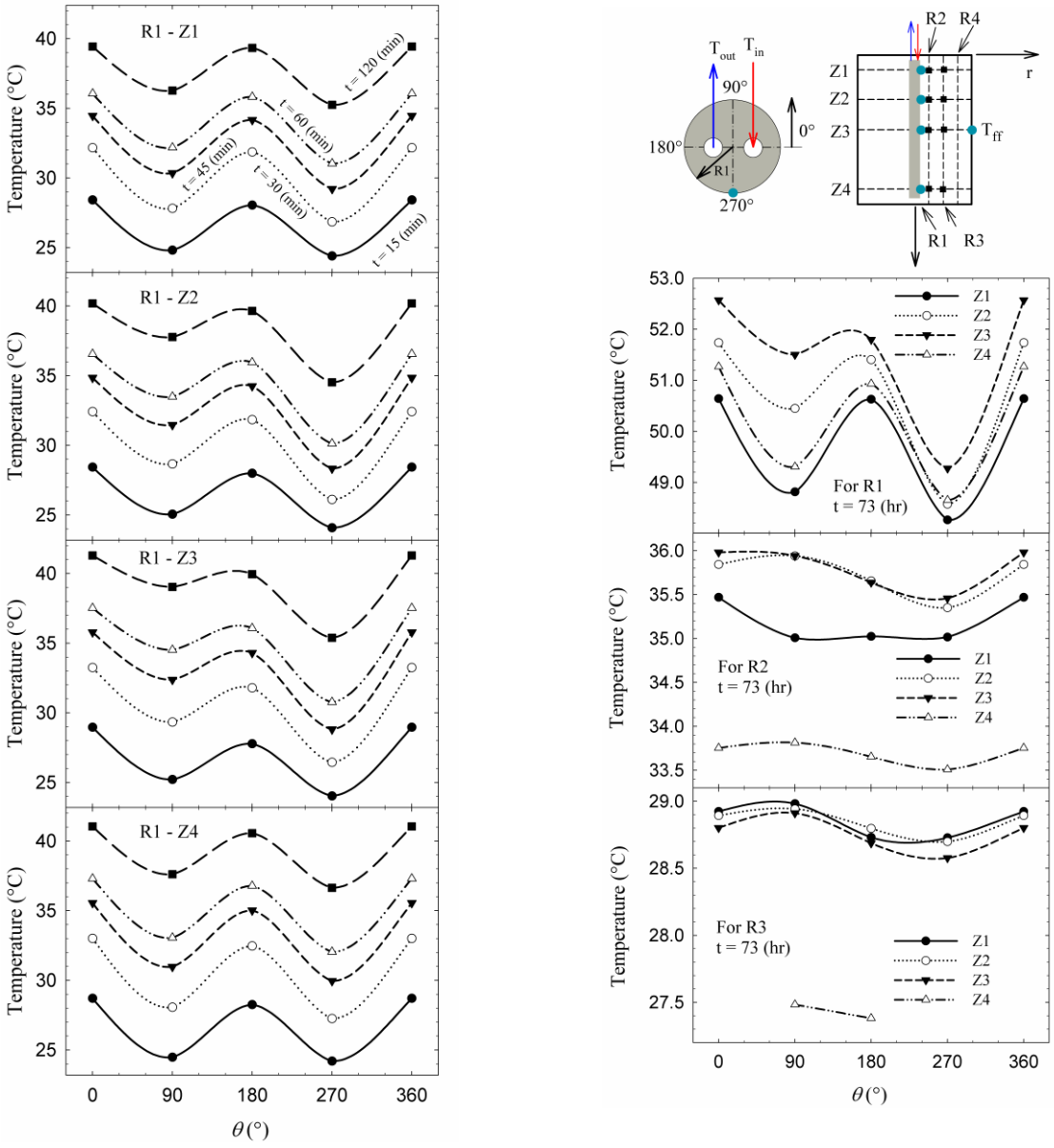

(a) Temperatures at *R1* for four azimuthal orientations and for different heights during the first two hours of heat injection.

(b) Temperatures at *R1*, *R2* and *R3* for different azimuthal orientations and at the end of the heat injection period.

Figure 5.9: Temperatures at various azimuthal orientations during the heat injection period.

At *Z4*, for *R2* and *R3*, the temperature profiles show significantly lower temperatures compared to those of the other vertical elevations.

5.4 Comparison with numerical results

In this section, experimental results are compared against results from the two-dimensional numerical model described in Chapter 3. This comparison exercise is best performed by presenting the data in several formats: temperature as a function of time in section 5.4.2; radial temperature profiles (i.e., temperature as a function of the radial distance) in section 5.4.3; vertical temperature profiles in section 5.4.4. However, before presenting the comparison exercise, it is important to present the various input conditions to the numerical model.

5.4.1 Inputs to the numerical model

Two types of boundary conditions are required: on the outside boundary of the calculation domain and on the outside diameter of the borehole wall (the inside of the borehole from the fluid to the borehole wall is not modeled). The following boundary conditions on the outside of the tank are used: adiabatic boundary condition on top (BC-T) and measured far-field temperature on the tank bottom and circumference (BC-B and BC-R, respectively).

At the borehole wall, the 16 measured temperatures are used as boundary conditions. As shown earlier, there is a large azimuthal variation in temperature at the borehole wall. Therefore, it was decided to use different borehole wall temperatures for each quadrant. In each quadrant, a vertical temperature profile was calculated using linear interpolation with the four measured temperatures. This profile was then used as the boundary condition at the borehole wall. The whole numerical domain is initially assumed to be at a uniform temperature of 23.5°C. A 202×202 grid was used in the numerical model with a time step of 10 seconds which is identical to the time interval at which the experimental data are acquired.

5.4.2 Temperature evolution with time

Measuring points which are implemented in the numerical model as boundary conditions are shown by solid green circles in the schematic on top of Figure 5.10 and Figure 5.13. The comparison is presented at positions which are indicated by solid black squares. As mentioned

earlier, due to the limitation of available channels, there are no measurements at *R3-0-Z4*, *R4-0-Z3*, *R4-0-Z4* and *R4-90-Z3*. There is also one faulty thermocouple at *R2-90-Z2*.

The comparison of the temperature evolution in time at different radial and vertical distances is shown in Figure 5.10 to Figure 5.12 for 0° and in Figure 5.13 at 90°. At 0° (Figure 5.10 to Figure 5.12) there is a very good agreement between the experimental data and the numerical results both in the heat injection and recovery periods. The numerical model has successfully predicted the sharp increases and decreases of temperature, the peak temperatures and the global trend of the experimental curves. At *Z2* and *Z3*, the comparison shows very good agreement. Near the top and bottom of the tank (*Z1* and *Z4)*, the comparison is not as good as the boundary conditions imposed in the numerical model may not correspond exactly to those experienced during the measurement. Also, for the temperature measured close to the top and bottom boundaries (*Z1* and *Z4*), the data might have been affected by the presence of the PVC crosses which have different thermal properties than the sand.

From Figure 5.11 it can be seen that the heat front reaches *R2* at different vertical heights less than two hours after the heat injection started. However it takes significantly more time for the heat front to reach *R3* and *R4*. This can be attributed to the relatively low thermal diffusivity of the sand which means that the injected heat is stored more easily than it is conducted. At the very beginning of the test, there is a slight difference between the experimental and numerical curves which is due to the fact that the initial temperature was set at uniform value of 23.5°C in the numerical model while in reality there are differences in the initial tank temperature as shown in Figure 5.1.

The whole injection period lasted 73 hours. However it can be observed from Figure 5.10 and Figure 5.12 , that the peak temperature reaches *R2* slightly after the heat injection period ends and later for the *R3* and *R4* positions. It is also interesting to note that the peak temperature at *R2* for the mid-height of the tank is about 32 °C lower than the temperature of the circulating fluid which is close to 68°C. This indicates the borehole itself and the sand offer a good thermal resistance and that the relatively high thermal mass of the sand serves as heat storage.

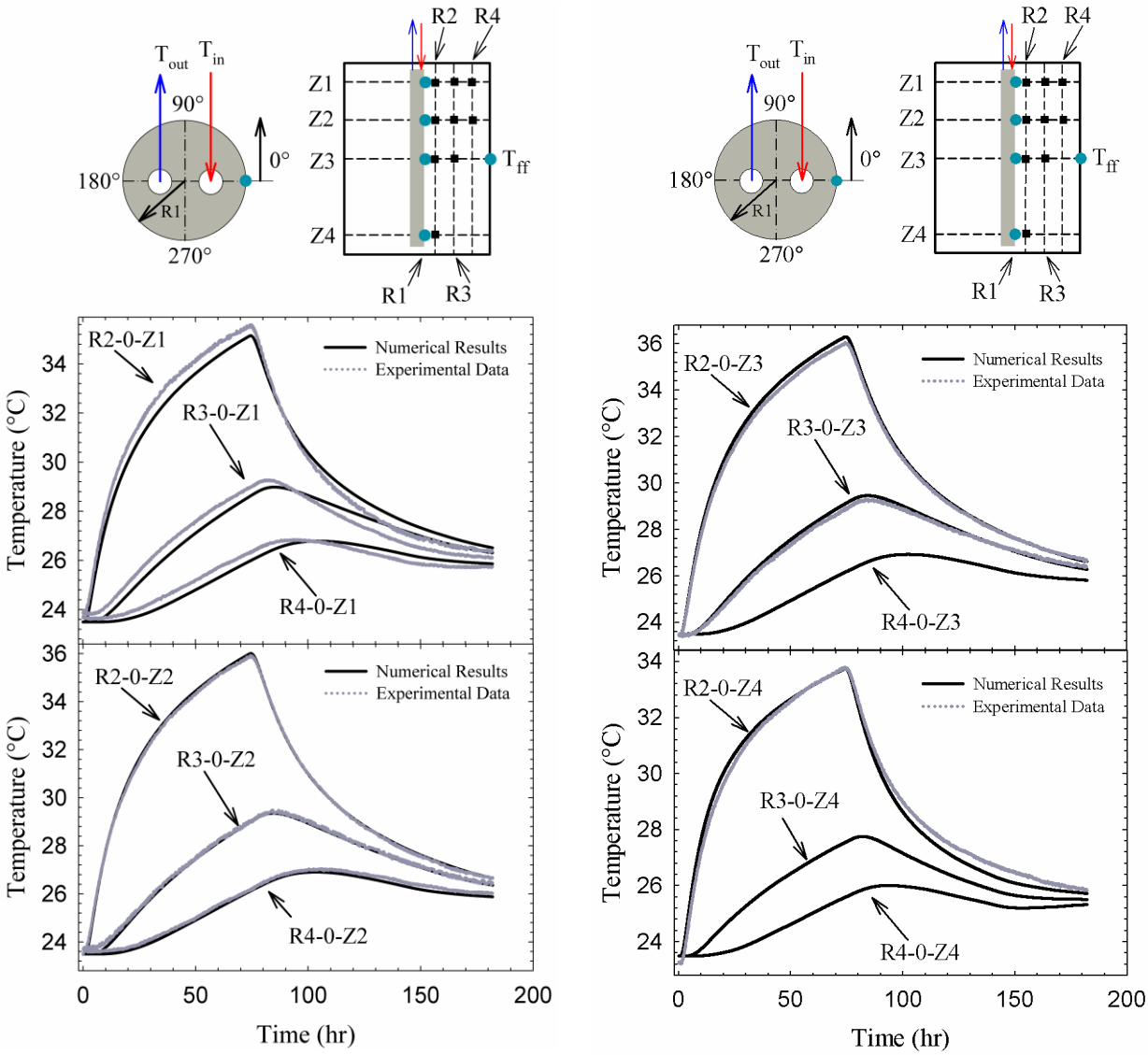

a) temperature evolution for *R2*, *R3* and *R4* at *Z1* and *Z2*.

b) temperature evolution for *R2*, *R3* and *R4* at *Z3* and *Z4*.

Figure 5.10: Comparison between experimental and numerical results at angle 0°.

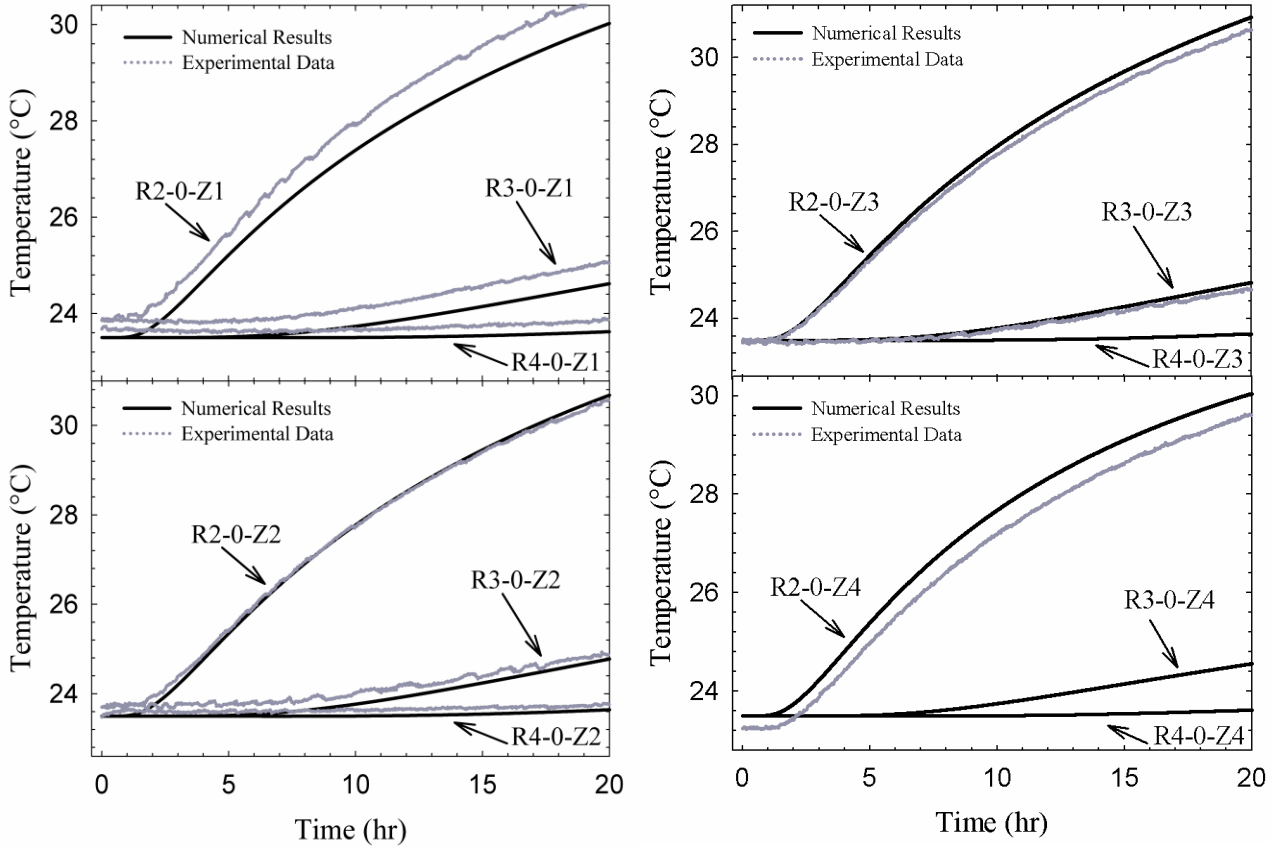

a) temperature evolution for *R2*, *R3* and *R4* at *Z1* and *Z2*.

b) temperature evolution for *R2*, *R3* and *R4* at *Z3* and *Z4*.

Figure 5.11: Temperature evolution in time at angle 0° for *R2*, *R3*, and *R4* for the first 20 hours of test.

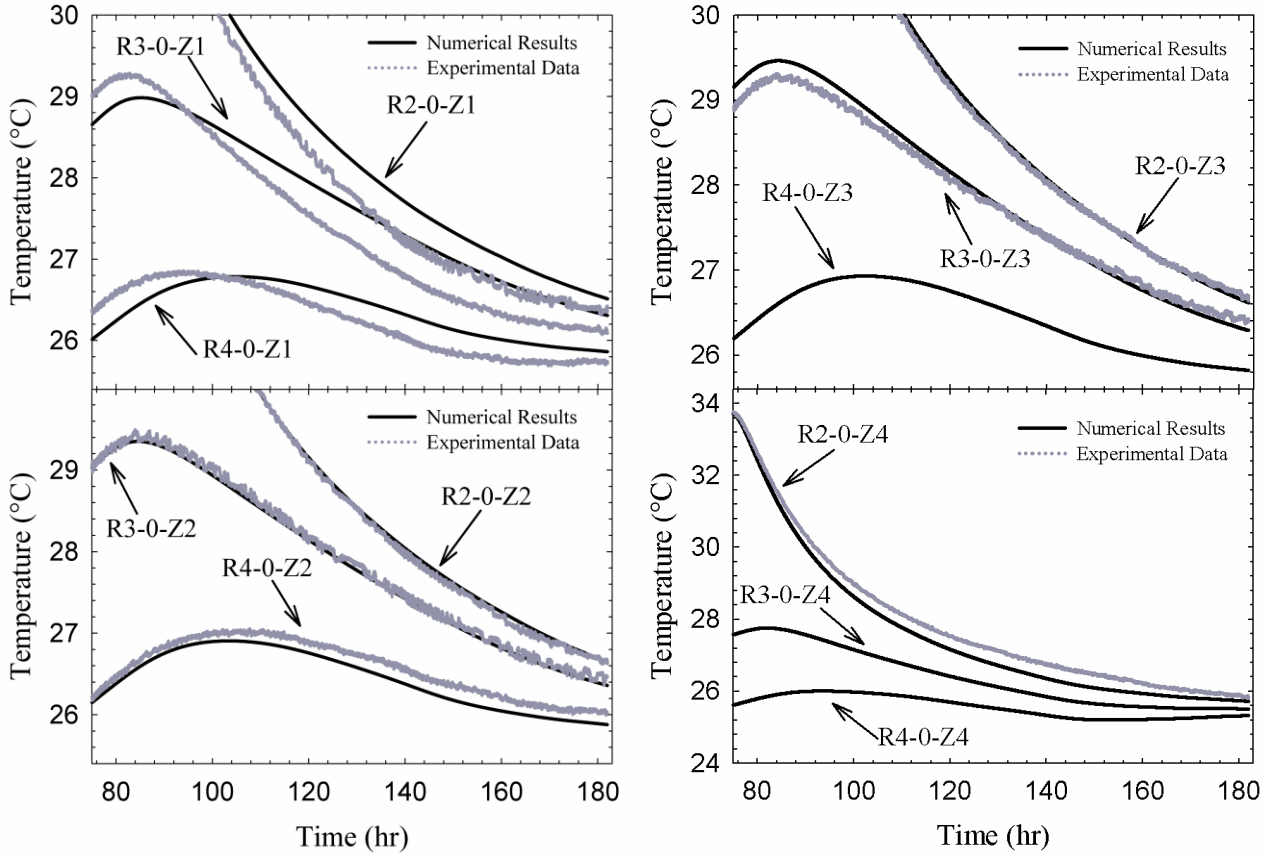

a) temperature evolution for *R2*, *R3* and *R4* at *Z1* and *Z2*.

b) temperature evolution for *R2*, *R3* and *R4* at *Z3* and *Z4*.

Figure 5.12: Temperature evolution in time at angle 0° for *R2*, *R3* and *R4* during the recovery period as shown in Figure 5.10.

From Figure 5.12 one can notice that the numerically predicted peak temperature at *R4-0-Z1* is slightly delayed compared to the experimentally measured peak temperature. It can be attributed to the imprecision of the position of the thermocouple installed at that point. At *R4-0-Z4*, It can be observe that towards the end of the recovery period the numerically predicted temperature curves are slowly increasing. This is due to the fact that the far-field temperature, which was imposed at BC-B and BC-R (i.e., boundary condition at the bottom and on the circumference), is also increasing. This means that there is heat transfer from the ambient to the inside of the tank.

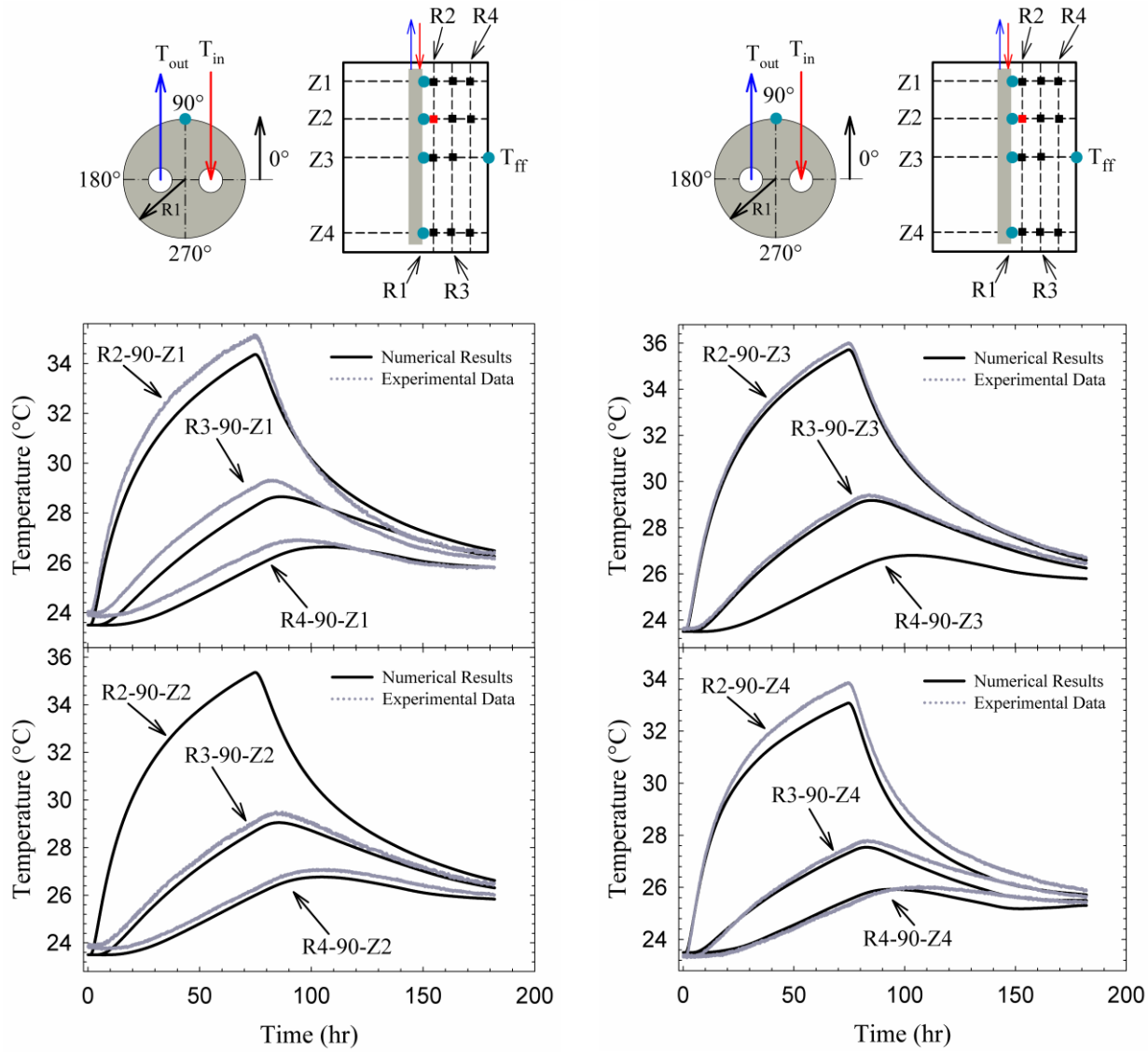

a) temperature evolution in time for *R2*, *R3* and *R4* at *Z1* and *Z2*.

b) temperature evolution in time for *R2*, *R3* and *R4* at *Z3* and *Z4*.

Figure 5.13: Comparison between experimental and numerical results at angle 90°.

For the 90° quadrant (Figure 5.13) the maximum number of measuring points is available with only one missing and one faulty thermocouple. Similar to the results for the 0° quadrant, there is good agreement between the experimental and numerical results. The best agreement exists at the interior/mid-height points (*Z2* and *Z3*) while the agreement is not as good for *Z1* and *Z4*. In general, the explanations mentioned in regards to the 0° quadrant are valid for 90° quadrant as

well. Decision was made to limit the analysis of the comparison of results to the 0° and 90° quadrant although similar results could be presented for 180° and 270° quadrants.

5.4.3 Radial temperature profiles

Temperature profiles as a function of the radial distance at Z2 and angle 0° for several times are shown in Figure 5.14 for the heat injection and recovery period. Numerically predicted temperature profiles are shown as lines. Experimental data are shown with their uncertainty (± 0.35 °C) at *R2, R3,* and *R4*. Excellent agreement can be observed as the numerical results lay within the uncertainty range for each numerical result.

Due to the very small thermal diffusivity of the sand, the heat front has barely reached the mid-radial distance of the experimental apparatus after 24 hours of continuous heat injection as one can observe from the top part of Figure 5.14. The bottom figure shows that during the recovery period, as the injected heat dissipates within the sand volume, the peak temperatures shift towards farther radial distances while the temperature profiles are getting flattened.

It should be reminded that the right-side boundary condition for the numerical simulation is set to the measured far-field temperature which varies in time. These variations can be seen at the farthest radial distance (i.e., which corresponds to the radius of the experimental apparatus) in Figure 5.14.

5.4.4 Vertical temperature profiles

Vertical temperature profiles at *R2* and angle 0° for several times are shown in Figure 5.15, for the heat injection and recovery periods. Aside from a few exceptions, the numerical predictions are all within the uncertainty range of the experimental results. Thus, based on these results and those presented earlier, it is felt that the numerical code can be used with confidence to study transient heat transfer in the ground with a known borehole wall temperature boundary condition.

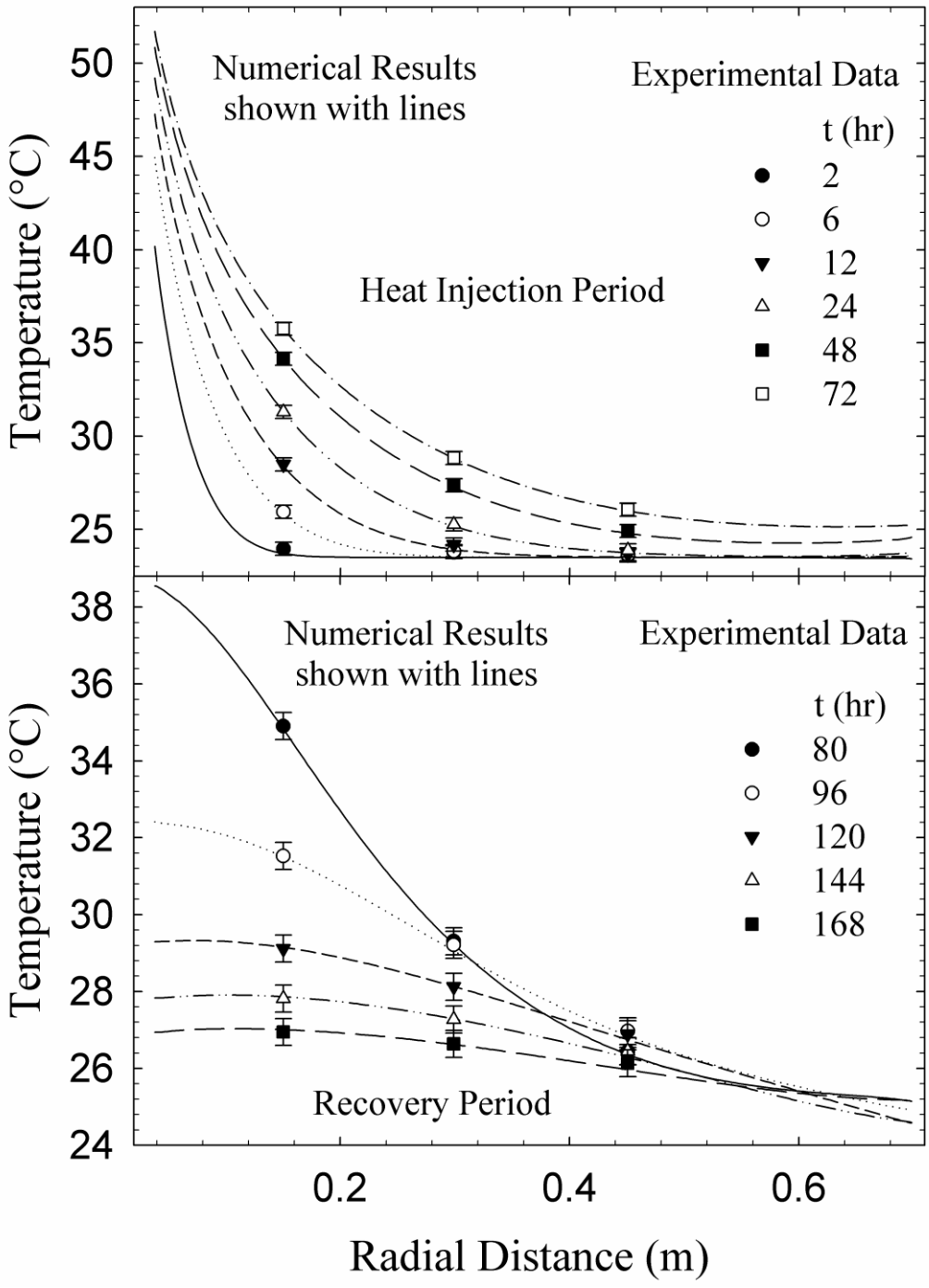

Figure 5.14: Temperature profile at angle 0° and height of *Z2* for heat injection period (top) and recovery period (bottom).

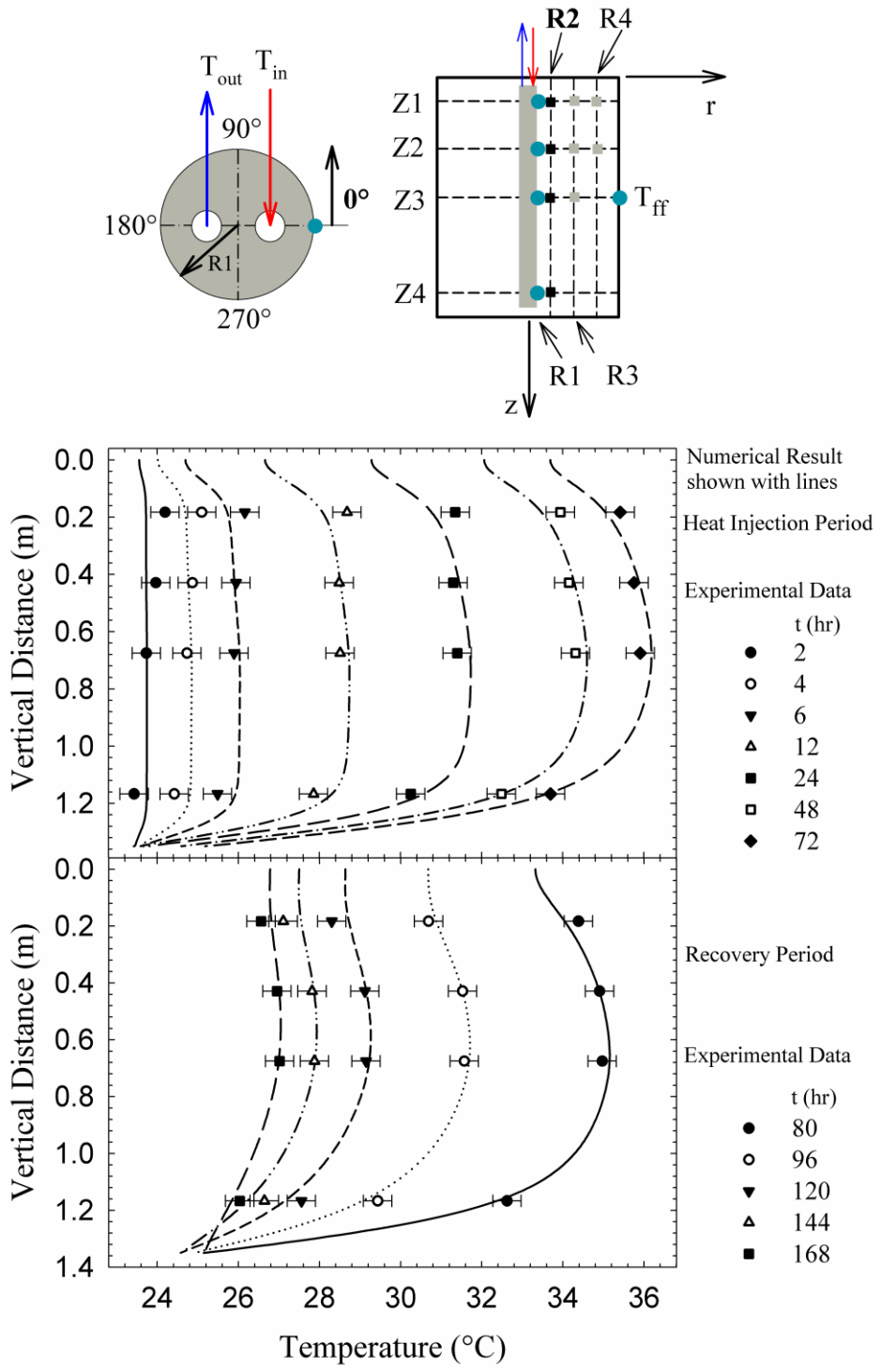

Figure 5.15: Temperature profile at angle 0° and *R2* radial distance for heat injection period (top) and recovery period (bottom).

During the first few hours of the heat injection period, the temperature profiles are almost vertical indicating that heat transfer is mostly one dimensional in the radial direction. After a certain amount of time, axial heat transfer effects become significant and the temperature varies in both the radial and axial directions.

It is interesting to make a parallel with the work of Eskilson (1987) which was reported in the literature review. In his proposed model, Eskilson assumed an infinite ground volume and the dimensions of the numerical domain were defined such that the heat front could neither reach the far-field radial distance nor the bottom extent of the domain. Furthermore, the borehole wall has a uniform temperature along the whole borehole length. Obviously, these are not the same conditions that prevailed here. However, a qualitative comparison is interesting. In his work, Eskilson introduced a characteristic time, t_s (= $H^2/9\alpha$), and proposed that after a time equal to $t_s/10$, axial heat transfer effects becomes significant. In this equation, H is the borehole length and α is the thermal diffusivity. For the experimental apparatus presented here, H = 1.23 m and α = 2.29×10^{-7} m^2/s which translates into a value of $t_s \approx$ 204 hr. Thus, according to Eskilson, the time after which the axial effects become important is approximately equal to 20.4 hours. One can observe from Figure 5.15 that the curves for t = 2, 4, and 6 hours, are somewhat like straight vertical lines and that curves for the t = 24, 48 and 72 hours show ellipse-like profiles which are characteristic of two-dimensional heat transfer around boreholes as shown earlier in section 3.3.2. Thus, it can be said that the behavior of the vertical profiles is in qualitative agreement with the theory presented by Eskilson.

In general, following the analysis presented in this chapter, the two-dimensional numerical code developed in Chapter 3 can be considered to be validated. Furthermore, despite the difficulties inherent in the construction and commissioning of an experimental facility of this size, the facility proved to be invaluable for validation.

CONCLUSION

Review of the objectives

Transient heat transfer inside and in the vicinity of vertical ground heat exchangers (GHE) is the main focus of the present thesis. A paucity of information in the literature has been identified in two areas. First, the effects of borehole thermal capacity on the annual coefficient of performance (COP) of heat pumps have not been studied extensively. Second, field-monitored data are usually inadequate for precise model validation and there is a lack of good experimental data obtained in controlled conditions. Given these gaps in the literature, this work was undertaken with the following objectives: i) develop a computationally efficient transient one-dimensional model that accounts for borehole thermal capacity that could be incorporated in energy simulation programs; ii) develop a two-dimensional numerical model of the ground in the vicinity of the borehole; iii) design and construct a small-scale experimental apparatus to validate the current models and to provide a database for future works.

Summary of the main contributions

Transient heat transfer inside the borehole is examined in Chapter 2. A hybrid analytical-numerical one-dimensional model is presented where heat transfer in the borehole is treated numerically and ground heat transfer is handled with the classic cylindrical heat source analytical solution. With this approach it is possible to study efficiently the effect of borehole thermal capacity. Borehole thermal capacity has been studied in the past but often times the thermal response of the borehole is predicted for a single and constant step change in temperature. The approach developed in Chapter 2 is more general but requires careful treatment of the various time periods from the residence time of the fluid in the borehole to the energy simulation time and including the time steps of the numerical simulation. A flow chart describing the relationship between these various time periods is presented in Figure 2.5 and constitutes an interesting contribution of the present work. With this procedure it is possible to predict the outlet fluid temperature from the borehole for varying inlet fluid temperature and flow rate conditions while doing annual simulations using a transient borehole model which very few models including TYPE451 (which is for double U-tube borehole heat exchangers), can do.

The one-dimensional approach imposes several assumptions which are rigorously presented. In particular, Equations (2.3) to (2.11) clearly show how the passage from a real two pipes (one U-tube) geometry to an equivalent one-pipe geometry is proceeded by keeping intact the important governing parameters notably the grout thermal capacity. The hybrid one-dimensional model is validated successfully against analytical solutions and experimental field data. In this last case, the agreement is very good with an RMS difference of 0.26 °C as reported in conjunction with Figure 2.9. Furthermore, the sudden temperature variations, associated with the on/off operation of the heat pump, are well captured by the proposed hybrid model.

After this validation phase, the hybrid model is used in simulations over an entire heating season with a single-stage geothermal heat pump linked to a borehole. The real on-off operation of the heat pump is simulated with a 6 minute time step. Two sets of simulations are performed: with and without borehole thermal capacity. Results show that for the B configuration, the annual heat pump coefficient of performance (COP) can be underestimated by 4.58 % when the borehole simulations do not account for the grout and fluid thermal capacities. When pipes are touching the borehole wall (C configuration), the COP is underestimated by 4.02% and when pipes are touching each other in the borehole center (A configuration), the COP is underestimated by 4.63%.

A detailed analysis of the results show that when the heat pump is operating infrequently (at the beginning and at the end of the heating season) the outlet temperature prediction when borehole thermal capacity is included can be 3.6 °C higher than when it is not included. During peak heating, the heat pump is operating almost continuously and the difference between the outlet temperature predictions diminishes to a negligible value. The results showing the impact of borehole thermal capacity on the annual coefficient of performance (COP) of heat pumps represent, with the exception of the work of Kim et al. (2010a), a new contribution to this field.

The next logical step in model development is to expand into a transient two-dimensional axi-symmetric model which is presented in Chapter 3. The model uses the classic finite volume approach. It is versatile enough to handle the three standard boundary conditions on any boundary. Furthermore, it is possible to impose different boundary conditions on segments along any of the four boundaries. This will prove useful when the two-dimensional borehole model under development is attached to this ground model. The model is successfully verified first

against a one-dimensional numerical model and then with the two-dimensional finite line source analytical solution. This is followed, in Chapter 5, by a successful validation against experimental data obtained from the experimental apparatus introduced in the present work.

One of the major contributions of this thesis is the experimental apparatus developed for the study of transient heat transfer in geothermal borehole heat exchangers. A significant level of effort went into the design, construction, and commissioning of this unique sand tank. The main features of the facility, which is described in Chapter 4, include: i) an instrumented 1.23 m long borehole with a carefully positioned U-tube and filled with well-characterized glass beads which act as the grout; ii) a string rack instrumented with some 60 precisely located thermocouples for ground temperature measurement; iii) laboratory-grade sand with known thermal properties; iv) fluid conditioning equipment that allows to feed the facility with user-specified inlet temperature and flow rate.

The facility proved to be extremely useful in the validation of the two-dimensional model. Results presented in Chapter 5 show that the numerical results are in very good agreement with the experimental results with most of the results lying within the experimental uncertainty. Such comparisons are extremely rare in the literature and the data presented in Chapter 5 could certainly be used by other researchers to validate their models. The time evolution of the vertical temperature profiles clearly show the passage from a radial-only heat transfer for small times to a ellipse-like profile characteristic of the axial-radial heat transfer occurring after long period of heat injection. Furthermore, the measured azimuthal temperature variation at the borehole wall seems to corroborate recent findings obtained using the improved analytical multipole method.

Recommendations for future work

The significance of the borehole thermal capacity on the annual heat pump energy consumption has been established in this work for one particular case. More work is required to cover the full spectrum of parameters including various building loads, different grout and ground thermal properties and heat pumps characteristics.

Implementation of the one-dimensional hybrid model in commercially available simulation software tools such as TRNSYS would make it readily available to a larger community and in particular to design engineers.

Work has started on the incorporation of a two-dimensional version of the borehole model presented in Chapter 2. Time constraints did not permit its completion. However, its addition to the existing two-dimensional axi-symmetric numerical model can prove to be useful for quantifying the impact of the one-dimensional assumptions used for the hybrid model and corroborate the findings on the effects of borehole thermal capacity.

With its capability of handling various ground layers the two-dimensional model could be exploited to study, for example, the impact of performing a thermal conductivity test in grounds made of layers with different properties.

Three-dimensional numerical modeling should also be envisioned in parallel with an experimental validation using the sand tank which measures the three-dimensional temperature field.

The experimental facility could be improved in four areas. First, more temperature measurements are required inside the borehole and on the borehole wall to validate two- and three-dimensional borehole models. Second, the ambient conditions surrounding the sand tank need to be better controlled either by conditioning the lab or by more insulation on the tank boundaries. The fluid conditioning system could be modified to accommodate a constant power source so as to add the capability to perform thermal conductivity tests. Finally, a higher thermal conductivity sand would be an asset as the sand used in this work has a fairly low thermal conductivity which increases the fluid temperature required to have a significant level of heat transfer. The same can be said for the glass beads inside the borehole.

The availability of an experimental facility such as the one developed for the present work opens up interesting possibilities for model validation. Other innovative experiments can also be envisioned. For example, extensive borehole wall temperature measurements could provide insight into the azimuthal and axial variation of temperature in order to ascertain whether the borehole wall approaches a condition of constant and uniform heat flux or constant and uniform borehole wall temperature. The sand inside the tank could be saturated with water. This would increase the thermal conductivity but would also enable ground freezing experiments.

The experimental apparatus as along with the proposed axi-symmetric ground model can be used to validate the *g-functions* of Eskilson.

REFERENCES

Anderson, J.D. (1996). *An introduction to computational fluid dynamics* (2nd ed.). Berlin: Springer.

ASHRAE/ANSI (1986). Guide for engineering analysis of experimental data. American Society of Heating Refrigeration and Air-Conditioning Engineers/American National Standards Institute.

Baliga, B. R., Atabaki, N. (2006). Control-volume-based finite difference and finite element methods. In Minkowycz, W. J., Sparrow, E. M., and Murthy, J. Y. (eds.), *Handbook of Numerical Heat Transfer* (2nd ed.). New York: John Wiley & Sons.

Bandyopadhyay, G., Kulkarni, M., Mann, M. (2008a). A new approach to modeling ground heat exchangers in the initial phase of heat-flux build up. *ASHRAE Transactions, 114*(2), 428-439.

Bandyopadhyay, G., Gosnold, W., Mann, M. (2008b). Analytical and semi-analytical solutions for short-time transient response of ground heat exchangers. *Energy and Buildings, 40*(10), 1816-1824.

Baudoin A. (1988). *Stockage intersaisonnier de chaleur dans le sol par batterie d'échangeurs baionnette verticaux : modèle de prédimensionnement.* Thèse de doctorat. Université de Reims, France.

Bauer, D., Heidemann, W., Muller-Steinhagen, H., Diersch, H.J.G. (2011). Thermal resistance and capacity models for borehole heat exchangers. *International Journal of Energy Research, 35*(4) , 312-320.

Beier, R.A. (2010). Vertical temperature profile in ground heat exchanger during in-situ test. *Renewable Energy, 36*(5), 1578-1587.

Beier, R. A., Smith, M. D., Spitler, J. D. (2011). Reference data sets for vertical borehole ground heat exchanger models and thermal response test analysis. *Geothermics, 40*(1), 79-85.

Bennet, J., Claesson, J., Hellström, G. (1987). Multipole method to compute the conductive heat flows to and between pipes in a composite cylinder. Technical Report, Department of Building Technology and Mathematical Physics, University of Lund, Lund, Sweden.

Bernier, M. (2000). *A review of the cylindrical heat source method for the design and analysis of vertical ground-coupled heat pump systems*. 4th International Conference of Heat Pumps in Cold Climates, 14 pages.

Bernier, M. (2001). Ground-coupled heat pump system simulation. *ASHRAE Transactions*, *106*(1), 605-616.

Bernier, M., Labib, R., Pinel, P., Paillot, R. (2004). A multiple load aggregation algorithm for annual hourly simulations of GCHP systems. *HVAC&R Research*, *10*(4), 471-487.

Bernier, M., Kummert, M., Bertagnolio. S. (2007). *Development and application of test cases for comparing vertical ground heat exchanger models*. 10th International IBPSA Conference, Beijing, 1462-1468.

Bernier, M., Salim Shirazi, A. (2007). *Solar heat injection into boreholes: a preliminary analysis*. Proceeding of 2nd Canadian Solar Building Conference, T1-1-1, 8 pages.

Carslaw, H. S., Jaeger, J. C. (1947). *Conduction of heat in solids* (1st ed). Oxford, U.K.: Claremore Press.

Chapuis, S. (2009). *Stockage Thermiuque saisonnier dans un champ de puits géothermiques verticaux en boucle fermée*. M.Sc.A., École Polytechnique de Montréal, Montreal, Qc., Canada.

Chapuis, S., Bernier, M. (2009). *Seasonal storage of solar energy in boreholes*. 11th International IBPSA conference, Glasgow, pp.599-606.

Claesson, J., Hellström, G. (2011). Multipole method to calculate borehole thermal resistances in a borehole heat exchanger. *HVAC & R Research*, *17*, 895-911.

Coleman, H.W., Steele, W.G. (1999). *Experimentation and uncertainty analysis for engineers* (2nd ed.). New York: Wiley.

Cooper, L.Y. (1976). Heating of a Cylindrical Cavity. *International Journal of Heat and Mass Transfer*, *19*, 575-577.

Cui, P., Yang, H., Fang, Z. (2008). Numerical analysis and experimental validation of heat transfer in ground heat exchangers in alternative operation modes. *Energy and Buildings, 40*(6), 1060-1066.

De Carli, M., Tonon, M., Zarrella, A., Zecchin, R. (2010). A computational capacity resistance model (CaRM) for vertical ground-coupled heat exchangers. *Renewable Energy, 35*(7), 1537-1550.

Deerman, J. D., Kavanaugh, S.P. (1991). Simulation of vertical U-Tube ground-coupled heat pump systems using the cylindrical heat source solution. *ASHRAE Transactions, 97*(1), 287-295.

Diao, N. R., Zeng, H. Y., Fang, Z. H. (2004). Improvement in modeling of heat transfer in vertical ground heat exchangers. *HVAC&R Research*, *10*(4), 459-470.

Du, C. Y., Chen, Y. M. (2011). An average fluid temperature to estimate borehole thermal resistance of ground heat exchanger. *Renewable Energy, 36*(6), 1880-1885.

Eskilson, P. (1987). *Thermal analysis of heat extraction boreholes.* Doctoral Thesis, University of Lund, Sweden.

Eslami Nejad, P. (2011). *Double U-tube geothermal borehole operation under phase change conditions*. Doctoral Thesis, École Polytechnique de Montréal, Montreal, Qc., Canada.

Eslami Nejad, P., Bernier, M. (2012). Freezing of geothermal borehole surroundings: A numerical and experimental assessment with application. *Applied Energy*, *98*, 333-345.

Farouki, O. T. (1981). *Thermal properties of soils*. Monograph 81-I, U.S. Army cold regions research and engineering laboratory.

Gu, Y., O'Neal, D.L. (1998). Modeling the effect of backfills on U-tube ground coil performance. *ASHRAE Transactions*, *104*(2), 356-365.

He, M., Rees, S.J., Shao, L. (2009). *Applications of a dynamic three-dimensional numerical model for borehole heat exchangers*. Effstock 2009, Stockholm, paper #90, 8 pages.

He, M., Rees, S.J., Shao, L. (2011). Simulation of a domestic ground source heat pump system using a three-dimensional numerical borehole heat exchanger model. *Journal of Building Performance Simulation*, *4*(2), 141-155.

Hellström, G. (1991). *Ground heat storage: Thermal analysis of duct storage systems.* Doctoral Thesis, University of Lund, Sweden.

Hellström, G., Mazzarella, L., Pahud, D. (1996). Duct ground storage model – TRNSYS version. Department of Mathematical Physics, University Of Lund, Sweden.

Holman, J. P. (2002). *Heat transfer* (9th ed.). Boston: McGraw-Hill.

Incropera, F.P., Dewitt, D.P. (2004). *Fundamentals of heat and mass transfer* (5th ed.). New York: Wiley.

Ingersoll, L. R., Zobel, O. J., Ingersoll, A. C. (1954). *Heat conduction with engineering geological and other applications* (2nd ed). New York: McGraw-Hill.

Javed, S., Claesson, J., Fahlén, P. (2010). *Analytical modelling of short-term response of ground heat exchangers in ground source heat pump systems.* Proceedings of the 10th REHVA World Congress, Clima 2010, Antalya, Turkey.

Kandula, M. (2010). Transient conduction in a hollow cylinder with variable thermal conductivity. *Journal of Heat Transfer, 132*(5), 1-3.

Kavanaugh, S. (1985). *Simulation and experimental verification of vertical ground-coupled heat pump systems.* Doctoral Thesis, Oklahoma State University, USA.

Kim, E.J., Roux, J.J, Bernier, M., Cauret, O. (2010a). *A new borehole heat exchanger (BHE) model based on state reduction techniques analysis*. 10th REHVA World Congress – Clima 2010, paper #R4-TS44-OP06, 8 pages.

Kim, E.J., Roux, J.J., Rusaouen, G., Kuznik, F. (2010b). Numerical modeling of geothermal vertical heat exchangers for the short time analysis using the state model size reduction technique. *Applied Thermal Engineering, 30*(6–7), 706–714.

Klein, S.A. (2011). EES, Engineering Equation Solver, F-chart software, Middleton, Wisconsin.

Klein, S.A. (2006). TRNSYS, A transient simulation program. Solar Energy Laboratory, University of Wisconsin, Madison, USA.

Kummert, M., Bernier, M. (2008). Analysis of a combined photovoltaic-geothermal gas-fired absorption heat pump system in a Canadian climate. *Journal of Building Performance Simulation, 1*(4), 245-256.

Lamarche, L., Beauchamp, B. (2007). New solutions for the short-time analysis of geothermal vertical boreholes. *International Journal of Heat and Mass Transfer*, *50*(7-8), 1408-1419.

Lamarche, L., Kajl, S., Beauchamp, B. (2010). A review of methods to evaluate borehole thermal resistances in geothermal heat-pump systems. *Geothermics*, *39*(1), 187-200.

Lee, C. K., Lam, H. N. (2008). Computer simulation of borehole ground heat exchangers for geothermal heat pump systems. *Renewable Energy*, *33*(6), 1286-1296.

Li, Z. J., Zheng, M. Y. (2009). Development of a numerical model for the simulation of vertical U-tube ground heat exchangers. *Applied Thermal Engineering*, *29*(5-6), 920-924.

Liu, X., Hellström.G. (2006). *Enhancements of an integrated simulation tool for ground-source heat pump system design and energy analysis*. Proceedings of Ecostock 2006, the 10th International Conference on Thermal Energy Storage, The Richard Stockton College of New Jersey.

Man, Y., Yang, H., Diao, N., Liu, J., Fang, Z. (2010). A new model and analytical solutions for borehole and pile ground heat exchangers. *International Journal of Heat and Mass Transfer*, *53* (13-14), 2593-2601.

Marcotte, D., Pasquier, P. (2008). On the estimation of thermal resistance in borehole thermal conductivity test. *Renewable Energy*, 33 (11), 2407-2415.

Marcotte, D., Pasquier, P., Sheriff, F., Bernier M. (2010). The importance of axial effects for borehole design of geothermal heat-pump systems. *Renewable Energy*, *35*(4), 763-770.

Moffat, R. J. (1982). Contributions to the theory of single-sample uncertainty analysis. *Journal of Fluids Engineering Transaction ASME*, *104*(2), 250-260.

Muraya, N. K., O'Neal, D. L., Heffington, W. M. (1996). Thermal interference in adjacent legs in a vertical U-tube heat exchanger for a ground coupled heat pump. *ASHRAE Transactions*, *102*(2), 12-21.

Ndiaye, D. (2007). *Étude numérique et expérimentale de la performance en régime transitoire de pompes à chaleur eau-air en cyclage.* Doctoral Thesis, École Polytechnique de Montréal, Montreal, Qc., Canada.

Nouanegue, H.F., Salim Shirazi, A., Bernier, M. (2009). *Extracted heat from geothermal boreholes : where does the energy come from*. 4th Annual Canadian Solar Buildings Conference : Plug into the sun, p. 227-236.

NRCan. (2006). Energy Use Data Handbook, 1990 and 1998 to 2004. (Consulted in May 2011). http://oee.nrcan.gc.ca/Publications/statistics/handbook06/chapter1.cfm?attr=0.

Oppelt, T., Riehl, I., Gross, U. (2010). Modelling of the borehole filling of double U-pipe heat exchangers. *Geothermics, 39*(3), 270-276.

Pasquier, P., Marcotte, D. (2012). Short-Term Simulation of Ground Heat Exchanger with an Improved TRCM. *Renewable Energy*. *46*, 92-99.

Patankar, S. V. (1980). *Numerical heat transfer and fluid flow* (2nd ed.). New York: McGraw-Hill.

Philippe, M., Bernier, M., Marchio, D. (2009). Validity ranges of three analytical solutions to heat transfer in the vicinity of single boreholes. *Geothermics, 38*(4), 407-413.

Remund, C. P. (1999). Borehole thermal resistance: laboratory and field studies. *ASHRAE Transaction*s, *105*(1), 439-445.

Rottmayer, S. P., Beckman, W. A., Mitchell, J. W. (1997). Simulation of a single vertical U-tube ground heat exchanger in an infinite medium. *ASHRAE Transaction*s, *103*(2), 651- 659.

Salim Shirazi A., Bernier, M. (2012). Thermal capacity effects in borehole ground heat exchangers", submitted to *Energy and Buildings*, March 2012.

Sherrif, F. (2007). *Génération de facteurs de réponse pour champs de puits géothermiques verticaux.* M.Sc.A., École Polytechnique de Montréal, Montreal, Qc., Canada.

Shonder, J.A., Beck, J.V. (1999). Determining effective soil formation thermal properties from field data using a parameter estimation technique. *ASHRAE Transactions*, *105*(1), 458-466.

Spitler, J. D., Bernier, M., Kummert, M., Cui, P., Liu, X. (2009). *Preliminary intermodel comparison of ground heat exchanger simulation models*. Effstock 2009, Stockholm, paper#115, 8 pages.

Sutton, M.G., Couvillon, R.J., Nutter, D.W., Davis, R.K. (2002). An algorithm for approximating the performance of vertical bore heat exchangers installed in a stratified geological regime. *ASHRAE Transactions*, *108*(2), 177-184.

Tarnawski, V. R., Momose, T., Leong, W. H., Bovesecchi, G., Coppa, P. (2009). Thermal conductivity of standard sands. Part I. dry-state conditions. *International Journal of Thermophysics*, *30*(3), 949-968.

Tarnawski, V. R., Momose, T., and Leong, W. H. (2011). Thermal conductivity of standard sands II. saturated conditions. *International Journal of Thermophysics*, *32*(5), 984-1005.

Veillon, F. (1972). *Quelques nouvelles méthodes pour le calcul numérique de la transforme inverse de Laplace*. Thèse de doctorat de 3^{em} cycle, University of Grenoble, France.

Wetter, M., Huber, A. (1997). TRNSYS Type 451 – Vertical borehole heat exchanger - EWS Model, (3.1 ed.).

Xu, X., Spitler, J.D. (2006). *Modeling of vertical ground loop heat exchangers with variable convective resistance and thermal mass of the fluid*. Proceedings of the 10th International Conference on Thermal Energy Storage – Ecostock 2006, Pomona, NJ.

Yang, H., Cui, P., Fang, Z. (2010). Vertical- borehole ground-coupled heat pumps: A review of models and systems. *Applied Energy*, *87*(1), 16-27.

Yavuzturk, C., Chiasson, A.D., Nydahl,J.E. (2009). Simulation model for ground loop heat exchangers. *ASHRAE Transactions*, *115*(2), 45-59.

Yavuzturk, C., Spitler, J. D. (2001). Field validation of a short time step model for vertical ground-loop heat exchangers. *ASHRAE Transactions*, *107*(1), 617-625.

Yavuzturk, C., Spitler, J. D. (1999). A short time step response factor model for vertical ground loop heat exchangers. *ASHRAE Transactions*, *105*, 475-485.

Yavuzturk, C., Spitler, J. D., and Rees, S. J. (1999). A transient two dimensional finite volume model for the simulation of vertical U-tube ground heat exchangers. *ASHRAE Transactions*, *105*(2), 465-474.

Young, T. R. (2001). *Development, verification, and design analysis of the borehole fluid thermal mass model for approximating short-term borehole thermal response*. Master of Science Thesis, Oklahoma State University, United States.

Zeng, H., Diao, N., Fang, Z. (2003). Heat transfer analysis of boreholes in vertical ground heat exchangers. *International Journal of Heat and Mass Transfer*, *46*(23), 4467-4481.

Zeng, H., Diao, N., Fang, Z. (2002). A finite line-source model for boreholes in geothermal heat exchangers. *Heat Transfer - Asian Research*, *31***,** 558-567.

APPENDIX A

Time step and grid independence check

This appendix presents the results of a time step and grid independence check performed on the numerical solution of transient heat transfer for the equivalent cylinder geometry presented in Chapter 2. A representative geometry and typical operating conditions are used for this check. These values are shown in Table A.1.

Table A.1: Parameters used in the time step and grid independence check.

Parameter	Value	Unit
r_b	0.075	m
r_{eq}	0.0265	m
k_{gd}	2.5	$W \cdot m^{-1} \cdot K^{-1}$
k_{gt}	0.74	$W \cdot m^{-1} \cdot K^{-1}$
$\rho_{gt} \times c_{gt}$	3.9	$MJ \cdot m^{-3} \cdot K^{-1}$
$\rho_{gd} \times c_{gd}$	2.5	$MJ \cdot m^{-3} \cdot K^{-1}$
T_∞	10	°C
$q''_{r_{eq}}$	232.95	$W \cdot m^{-2}$
T_w	Obtained from the solution to ground heat transfer	

The time step and grid independence check results are presented in Figure A.1 and Figure A.2, respectively. These figures show the temperature distribution inside the borehole, from the equivalent cylinder radius to the borehole wall.

In Figure A.1, there are three series of curves showing the temperature distribution in the equivalent cylinder for residence times (*RT*) corresponding to sixty, five and two minutes, respectively. A total of 40 grid nodes are used for this time step check. As will be shown shortly, this number ensures that the solution is essentially grid independent and that the results shown in Figure A.1 do not depend on the grid spacing. Each series of curves shows results for five

different Δt corresponding to RT, RT/5, RT/10, RT/20, RT/100. For RT=2 and 5 min, the temperature distribution are almost identical when $\Delta t \geq RT/5$. In the case of RT=60 min, results can be considered to be grid independent for $\Delta t \geq RT/20$. It should be noted that a value of RT=60 min is unlikely to occur in practice as the fluid residence time in a borehole is of the order of 2 to 5 minutes. The grid independence check presented in Figure A.2 shows temperature distributions obtained by varying the number of grids from 6 to 80 with RT=60 min and Δt = 3 min. The insert shows a close-up in the radial region from 0.04 to 0.05 m. Clearly, these results show that 10 grid points are sufficient to obtain a grid independent solution.

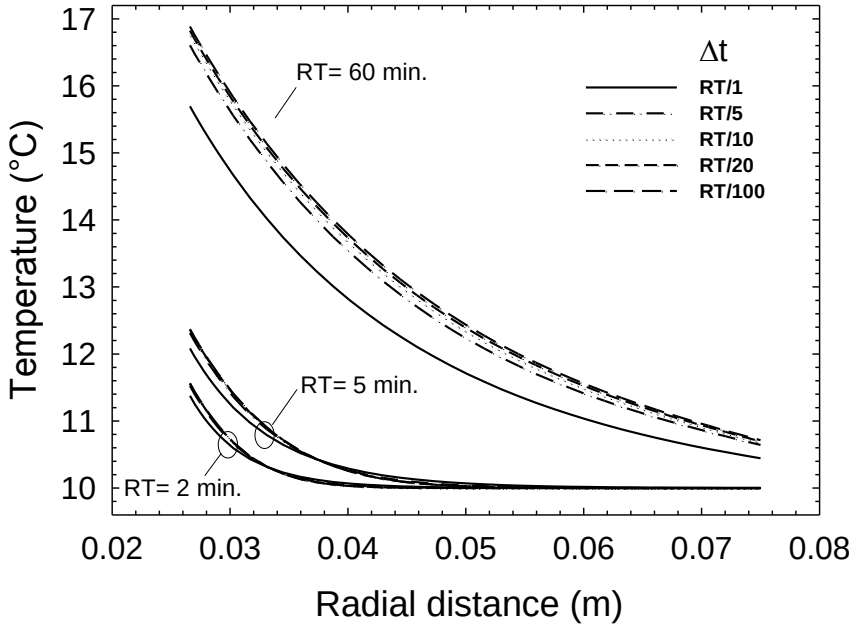

Figure A.1: Time step independence check for three different residence times (RT) and five corresponding numerical time step (Δt).

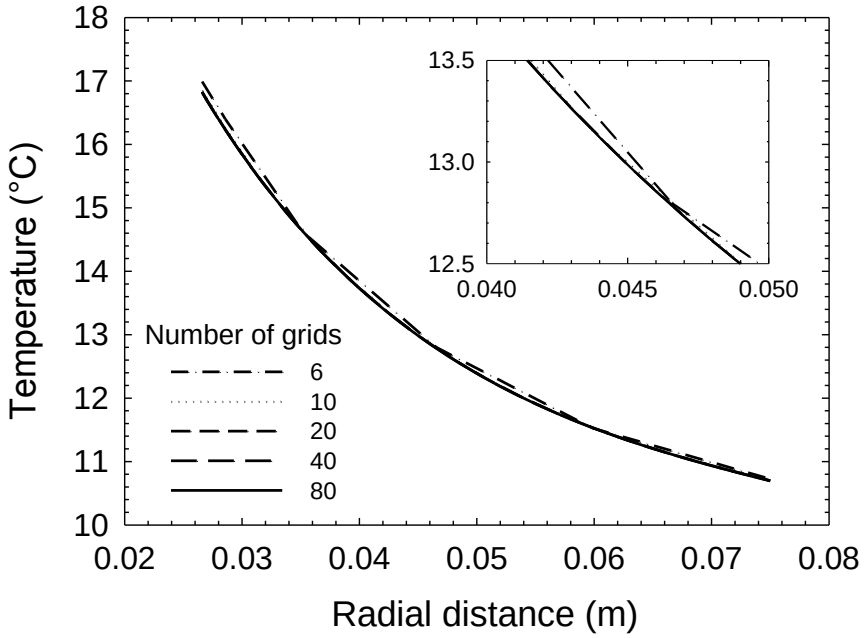

Figure A.2: Grid independence check for RT=60 min and Δt = 3 min.

APPENDIX B

Steady state analytical solutions to heat transfer from a cylinder

The steady state solution to heat transfer in a composite cylinder can be found in many standard text books on heat transfer (e.g. Incropera and Dewitt, 2004). The discrete values of temperatures shown in Figure 2.7 are obtained using the following approach. First, the domain is divided into 160 nodes (from r = 0.022 to 1 m). Then, the temperature at the first node *T(1)* , i.e., at the inner pipe wall, is evaluated using:

$$T(1) = T_{r_0} = T_\infty + (2\pi r_0 L) R_{total} q'' \tag{B.1}$$

where the total thermal resistance is given by:

$$R_{total} = \frac{Ln\left(\frac{r_1}{r_0}\right)}{2\pi k_1 L} + \frac{Ln\left(\frac{r_2}{r_1}\right)}{2\pi k_1 L} + \frac{Ln\left(\frac{r_3}{r_2}\right)}{2\pi k_3 L} \tag{B.2}$$

Then, the remaining nodes are calculated using:

$$T(i+1) = T(i) - q''(2\pi r_0 L)\frac{Ln\left(\frac{r_{i+1}}{r_i}\right)}{2\pi k_i L} \tag{B.3}$$

for $1 < i < 160$

APPENDIX C

Transient analytical solutions to heat transfer from a cylinder

Veillon (1972) and Baudoin (1988) provide a relatively simple analytical solution to transient heat transfer in a cylinder subjected to a constant heat transfer rate per unit length on its wall and immersed in an infinite medium at a constant far-field temperature. This solution is given by:

$$\theta(r,t) = \frac{q'}{2\pi r_{eq} k} \sum_{j=1}^{10} \frac{V_j}{j} \frac{K_0(\omega_j r)}{\omega_j K_1(\omega_j r_{eq})}$$

$$\omega_j = \sqrt{\frac{j\,ln(2)}{\alpha.t}} \qquad \text{(C.1)}$$

$$V_j = \sum_{k=int\left(\frac{j-1}{2}\right)}^{min(j,5)} \frac{(-1)^{j-5} k^5 (2k)!}{(5-k)!(k-1)!\,k!\,(j-k)!(2k-j)!}$$

where $\theta(r,t)$ *is* the relative temperature at different radii (i.e., temperature at a particular radial distance minus the far field temperature, $\theta(r,t)=T(r,t)-T_\infty$) as a function of time.

Values of $\theta(r,t)$ prevailing over discrete value of Δr are calculated. The time dependent heat flux at the borehole wall is then evaluated using Fourier's law of heat conduction:

$$-k \left.\frac{\Delta\theta}{\Delta r}\right|_{r=r_{bore}} = q''_{bore}(t) \qquad \text{(C.2)}$$

where $\Delta\theta = (\theta(r_{bore}) - \theta(r_{bore} - \Delta r))$.

APPENDIX D

Calibration of the temperature measurement probes

D.1 Introduction

In this appendix, the experimental procedure used for calibrating the thermocouples and the thermistors is described followed by a presentation of the calibration results. A total of sixty eight copper-constantan thermocouples (type T) and two prefabricated thermistors (TH-44032-1/8NPT-160 by Omega) were calibrated. The experimental set-up used for calibrating the thermocouples and thermistors is shown in Figure D.1 with a description of the various instruments given in Table D.1.

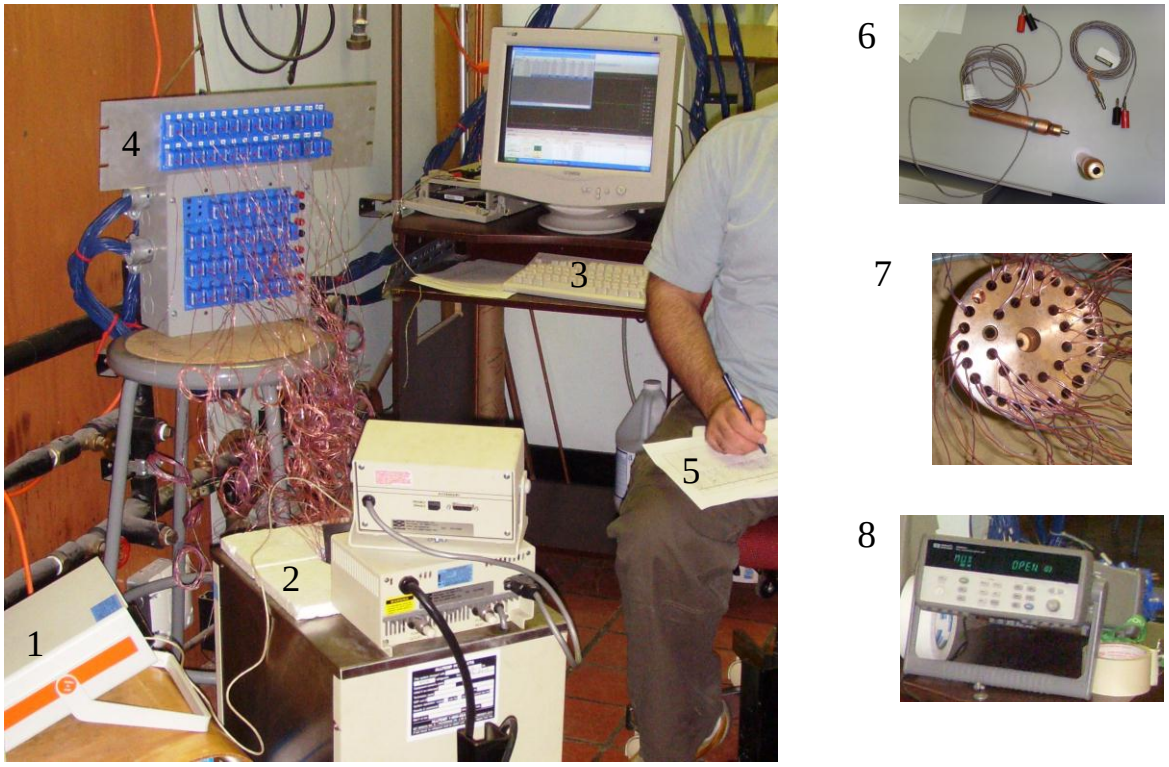

Figure D.1: Demonstration of the thermistor/thermocouple calibration set-up.

The objective of the calibration is to correct the measured temperatures and to obtain a measure of the uncertainty in the temperature measurements by comparing them with a reference

temperature. In the present case, the reference temperature is a digital platinum resistance thermometer (Guildline 9540). It has been calibrated at Hydro-Quebec's research institute in Varennes (IREQ). The calibration report states that the uncertainty of the reference thermometer is ±0.21°C when all possible sources of uncertainties are accounted for. Therefore, this is a conservative assessment of the uncertainty of the device.

Table D.1: Description of the various instruments in Figure D.1

Number in Figure D.1	Description
1	Digital platinum resistance thermometer (Guildline 9540)
2	Constant temperature bath (Neslab RTE 220)
3	Personal computer
4	Thermocouple junction box (i.e., TC box)
5	Manual readings of the reference temperature
6	Thermistors (TH-44032-1/8NPT-160 by Omega). Bare thermistor (on the right) and special water-tight jacket (on the left)
7	Copper block to hold thermocouples
8	Data acquisition unit (HP 34970A).

The platinum resistance thermometer, the thermocouples and the thermistors were inserted in holes in a machined cylindrical copper block 7.6 cm in diameter and 10 cm long (identified as number 7 in Figure D.1). The copper block is then inserted into a constant temperature bath (Neslab RTE 220) filled with a water-glycol mixture (50%). The copper block provides a thermal damper which reduces temperature fluctuations occurring in the bath fluid temperature. The calibration was performed over the temperature range of -15°C to 90°C for the thermocouples and -15°C to 75°C for the thermistors, with steps of 2.5°C for the temperature range from 50°C to 70°C and steps of 5°C for temperatures below 50°C or above 70°C.

As shown in Figure D.1 the thermocouples are connected to the data acquisition unit (HP 34970A) through the thermocouple junction box. The measuring chain in the calibration was the same as the one used in the actual experiments. For the thermocouples, the chain is composed of the measuring tip, the fine gage thermocouple wire, the junction TC box, the large gage extension

wire, and finally the junction in the data acquisition card. For the two thermistors, they were connected to the data acquisition unit directly just like in the actual experiments. The data acquisition unit is connected to a personal computer through a GPIB cable. A program developed in the Agilent BenchLink Data Logger Pro.3 software facilitated the calibration and data acquisition by displaying and recording all the thermocouple and thermistor measurements in real time.

It should be noted that the number of channels provided by the data acquisition unit was limited to 60. Since a total 70 measurements were required (68 thermocouples and 2 thermistors), the calibration is done by using two configurations. In the first configuration, both thermistors plus 58 thermocouples (TC-3 to TC-60) are connected while in the second configuration, 10 thermocouples (TC-51 to TC-60) are replaced by 10 "auxiliary" thermocouples (TC-A51 to TC-A60).

D.2 Thermocouple calibration

The calibration procedure for the thermocouples consists of the following steps:

1. Thermocouples are inserted in the copper block which is then submerged in the glycol-mixture filled constant temperature bath. The personal computer, all the measuring probes as well as the constant temperature bath are turned on almost three hours before starting the calibration and the constant temperature bath is set to -15°C for the first test.

2. After the constant temperature bath stabilizes at the target temperature, data reading starts with time intervals of ten seconds for both the digital platinum resistance thermometer and all thermocouples. When the difference between two consecutive readings is small enough (±0.05°C) it is assumed that steady-state conditions have been reached. The raw data from the thermocouples (in °C) are then read and saved on the personal computer for a time period of five minutes at intervals of ten seconds (30 sets of data recorded) while the readings from the platinum resistance thermometer are recorded manually every thirty seconds (a total of ten readings). The 30 readings for each thermocouple and the 10 readings for the platinum resistance thermometer are then averaged and constitutes the measured temperature at that bath temperature.

3. The target temperature of the constant temperature bath is increased by either 2.5 °C or 5°C depending on the target temperature. This whole procedure is replicated until the target temperature reaches a value of 90°C.

For each thermocouple, the averaged temperatures obtained for each target temperature are plotted against the corresponding averaged reference temperature. One such plot is presented in Figure D.2 where the temperatures given by the correlation equation are also shown (the procedure explained next).

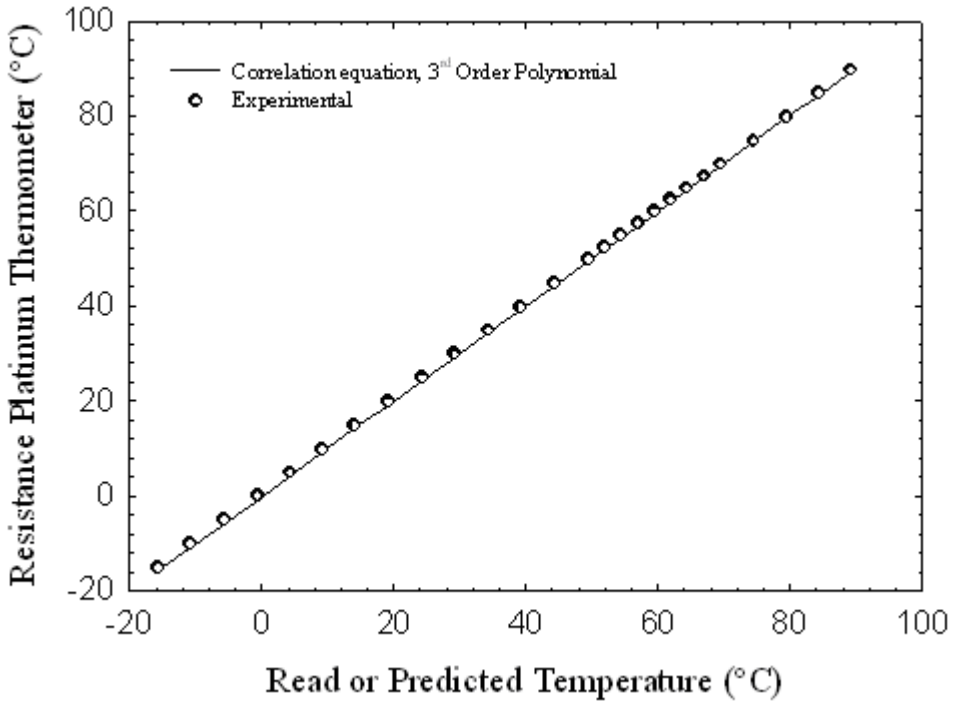

Figure D.2: Experimental and correlation predicted data versus those of the platinum probe for thermocouple # 37.

The measured raw thermocouple temperatures are corrected using a curve-fitted equation based on a least square procedure. Based on preliminary tests, a third order polynomial was found to predict the reference temperature with good accuracy ($R^2 > 0.99999$).

The calibration correlations have the following form:

$$T_{ref} = a_{0,j} + a_{1,j}\overline{T}_{tc,j} + a_{2,j}\overline{T}_{tc,j}^2 + a_{3,j}\overline{T}_{tc,j}^3 \qquad \text{(D.1)}$$

Table D.2: Correlation coefficients for all thermocouples.

TC Number	Channel Number	Reference Number	$a_{1,j}$	$a_{2,j}$	$a_{3,j}$	$a_{4,j}$
3	103	R1-0-Z1	-0.12507	0.998058	-4.8E-05	4.95E-07
4	104	R1-90-Z1	-0.14685	0.997559	-2.6E-05	2.97E-07
5	105	R1-180-Z1	-0.2203	0.998145	-2E-05	1.94E-07
6	106	R1-270-Z1	-0.25937	0.998179	-1.5E-05	1.53E-07
7	107	R1-0-Z2	-0.14915	0.99824	-2.9E-05	2.85E-07
8	108	R1-90-Z2	-0.15095	0.998589	-3E-05	2.81E-07
9	109	R1-180-Z2	-0.15049	0.998408	-4E-05	3.85E-07
10	110	R1-270-Z2	-0.08254	0.998538	-4.9E-05	4.79E-07
11	111	R1-0-Z3	-0.02594	0.998666	-6E-05	5.82E-07
12	112	R1-90-Z3	-0.08933	0.998945	-5.9E-05	5.3E-07
13	113	R1-180-Z3	-0.00876	0.999108	-7.6E-05	7.2E-07
14	114	R1-270-Z3	0.034194	0.998991	-7.9E-05	7.44E-07
15	115	R1-0-Z4	-0.00347	1.001284	-8.7E-05	7.65E-07
16	116	R1-90-Z4	0.105697	1.001089	-0.00011	9.74E-07
17	117	R1-180-Z4	0.149085	1.001332	-0.00011	9.92E-07
18	118	R1-270-Z4	0.243536	1.00097	-0.00012	1.15E-06
19	119	TC-U_{in}	0.330551	0.998327	-0.00012	1.27E-06
20	120	TC-U_{out}	0.341345	0.997644	-0.00012	1.27E-06
21	201	R2-0-Z1	0.61304	0.998694	-0.00015	1.4E-06
22	202	R2-90-Z1	0.529161	0.998167	-0.00012	1.16E-06
23	203	R2-180-Z1	0.515939	0.997957	-0.0001	1.02E-06
24	204	R2-270-Z1	0.451612	0.997867	-8.8E-05	8.62E-07
25	205	R2-0-Z2	0.374291	0.998196	-7E-05	6.62E-07
26	206	R2-90-Z2	0.292895	0.99807	-5.8E-05	5.88E-07
27	207	R2-180-Z2	0.408163	0.997946	-6.7E-05	6.63E-07
28	208	R2-270-Z2	0.418103	0.997723	-7.2E-05	7.17E-07
29	209	R2-0-Z3	0.429486	0.997771	-7.5E-05	7.5E-07
30	210	R2-90-Z3	0.505814	0.99794	-8.7E-05	8.95E-07
31	211	R2-180-Z3	0.547554	0.997687	-0.0001	1.04E-06
32	212	R2-270-Z3	0.394952	0.99848	-8.7E-05	8.48E-07
33	213	R2-0-Z4	0.480717	0.998201	-0.00011	1.14E-06
34	214	R2-90-Z4	0.498507	1.000374	-0.00013	1.23E-06
35	215	R2-180-Z4	0.537028	1.000169	-0.00013	1.25E-06

36	216	R2-270-Z4	0.659465	1.000155	-0.00015	1.44E-06
37	217	R3-0-Z1	0.767295	0.998058	-0.00016	1.66E-06
38	218	R3-90-Z1	0.825413	0.99772	-0.00018	1.82E-06
39	219	R3-180-Z1	0.803111	0.998003	-0.00019	1.95E-06
40	220	R3-270-Z1	0.784544	0.998152	-0.0002	2.07E-06
41	301	R3-0-Z2	0.327371	0.999971	-0.00018	1.74E-06
42	302	R3-90-Z2	0.167412	0.999585	-0.00015	1.45E-06
43	303	R3-180-Z2	0.062445	0.999679	-0.00014	1.39E-06
44	304	R3-270-Z2	-0.04547	0.999729	-0.00013	1.2E-06
45	305	R3-0-Z3	-0.20426	0.999761	-0.0001	9.84E-07
46	306	R3-90-Z3	-0.38188	1.002306	-9.8E-05	8.64E-07
47	307	R3-180-Z3	-0.39604	1.002136	-0.0001	9.43E-07
48	308	R3-270-Z3	-0.3415	1.001991	-9.7E-05	8.73E-07
49	309	TC-FF at 0°	-0.29848	0.999862	-9E-05	8.24E-07
50	310	TC-TOP at 0°	-0.29404	1.000306	-0.00011	1.07E-06
51	311	R3-180-Z4	-0.24068	1.003116	-0.00016	1.36E-06
52	312	R3-270-Z4	-0.25252	1.001721	-0.00011	1E-06
53	313	R4-0-Z1	-0.12099	0.999716	-0.00012	1.19E-06
54	314	R4-90-Z1	-0.07503	1.000045	-0.00014	1.28E-06
55	315	R4-180-Z1	-0.00396	1.000397	-0.00014	1.34E-06
56	316	R4-270-Z1	0.103522	0.999992	-0.00017	1.6E-06
57	317	R4-90-Z2	0.082435	1.000903	-0.00018	1.72E-06
58	318	R4-180-Z2	0.194644	0.999978	-0.00019	1.86E-06
59	319	R4-270-Z2	0.265263	0.999916	-0.0002	2.04E-06
60	320	R4-0-Z2	0.255417	1.000825	-0.00024	2.35E-06
A-51	311	R3-0-Z4	-0.15745	0.99953	-0.0001	9.85E-07
A-52	312	R3-90-Z4	-0.23973	1.001549	-9.1E-05	8.06E-07
A-53	313	R4-0-Z3	-0.10697	0.999651	-0.00011	1.06E-06
A-54	314	R4-90-Z3	-0.10427	1.001647	-0.00013	1.2E-06
A-55	315	R4-180-Z3	-0.03171	1.00224	-0.00014	1.26E-06
A-56	316	R4-270-Z3	0.071057	1.002371	-0.00018	1.66E-06
A-57	317	R4-0-Z4	0.123728	1.00047	-0.00019	1.88E-06
A-58	318	R4-90-Z4	0.192739	1.001879	-0.00021	2.1E-06
A-59	319	R4-270-Z4	0.255546	1.002595	-0.00025	2.42E-06
A-60	320	TC-BT at 0°	0.296125	1.001239	-0.00027	2.69E-06

where T_{ref} is the reference temperature, $\overline{T}_{tc,j}$ is the mean measured raw temperature of thermocouple j and $a_{i,j}$ represents the i^{th} order coefficient of the polynomial for the thermocouple j. These coefficients are presented in Table D.2 for each thermocouple.

D.2.1 Uncertainty analysis for thermocouples

The uncertainty of the temperature measurement itself together with that of the accuracy of the probe location, constitute the two elements of the global uncertainty of the temperature measurements of the sand in the tank.

In a recent study by Eslami Nejad (2011) for the same sand and a similar case, the uncertainty related to the accuracy of the thermocouple location was numerically determined following the method presented by Moffat (1982). Eslami Nejad (2011) proposed that except for close radial distances from the heat source, the impact of the imprecision of the probe location (±1 mm here) on the global uncertainty is insignificant. Based on this conclusion, it was decided to neglect the impact of the imprecision of the probe location on the temperature measurement uncertainties. Thus, the global uncertainty on the temperature measurement consists of the uncertainties associated with: the reference temperature probe; the fluctuations of the temperature measurements; and the calibration equation. These uncertainties are discussed below and are partly based on the analysis provided by Ndiaye (2007).

D.2.1.1 Uncertainty of the reference temperature

As mentioned before, the uncertainty of the reference thermometer, denoted here as U_1. is ±0.21°C.

D.2.1.2 Uncertainty in measuring the temperature

The temperature is measured and recorded by the data acquisition system for a time period of five minutes at intervals of ten seconds (30 sets of data recorded) at each target temperature where its averaged value is used for the calibration and uncertainty analysis. At each of the measured target temperatures, the impact of the fluctuation of the measured temperature has to be taken into account. At each target temperature, the standard deviation of the 30 measurements, σ, is calculated. The uncertainty associated with temperature measurement fluctuations is assumed to

be twice the standard deviation, 2σ, which covers 95.5% of the measurements (ASHRAE/ANSI , 1986). It is denoted by U_2.

D.2.1.3 Uncertainty of the correlation equation in predicting the temperature

Denoted by U_3, the uncertainty of the correlation represents the absolute difference between the reference temperature and the one calculated from the correlation equation.

D.1.1.4 Global uncertainty of the thermocouple measurements

Applying the method of propagation of the uncertainties presented by Coleman and Steele (1999), U_g, the global uncertainty is obtained from:

$$U_g = \sqrt{U_1^2 + U_2^2 + U_3^2} \tag{D.2}$$

A detailed example of the uncertainty calculation for TC37 is shown Table D.3. The global uncertainty values for all thermocouples are presented in Table D.4 and plotted in Figure D.3.

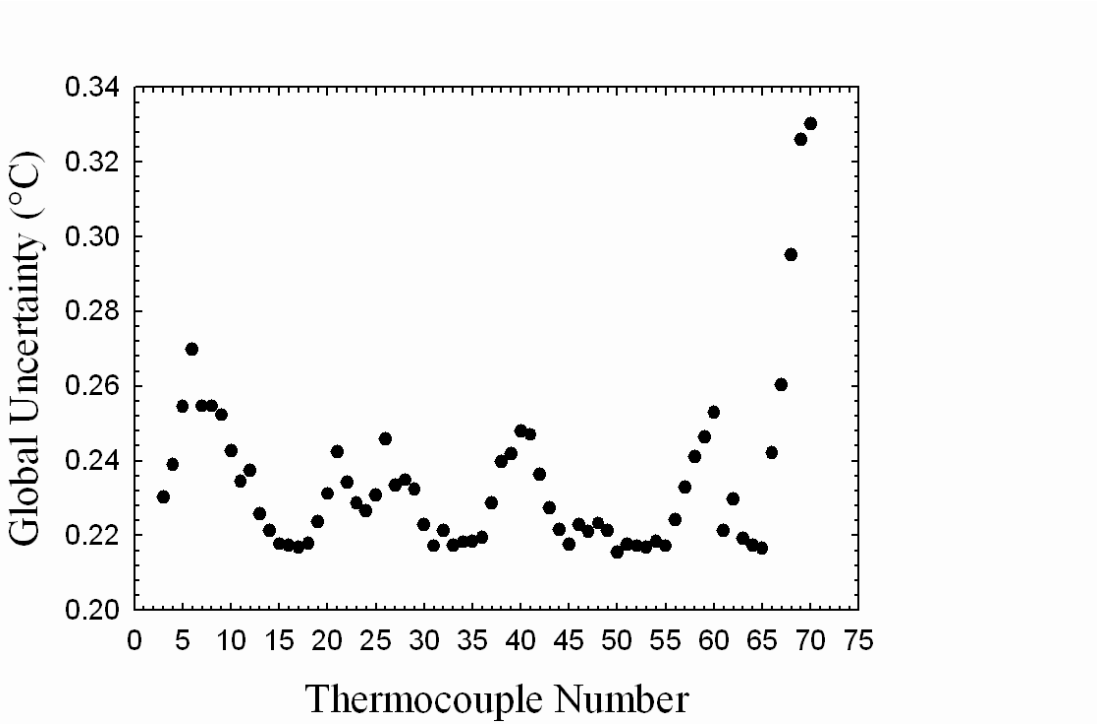

Figure D.3: Calculated global uncertainty for all the thermocouples (TC-A51 to TC-A60 are Numbered and demonstrated by 61 to 70).

Table D.3: Detailed calculation of the uncertainty for thermocouple # 37.

RTD (°C)	TC # 37 (°C)	σ (°C)	U2=2σ (°C)	Calibration Curve Fit (°C)	U_3 (°C)	U_g (°C)
-15.015	-15.787	0.0102	0.0203	-15.036	0.0208	0.212
-10.056	-10.8060333	0.0102	0.0204	-10.039	-0.0172	0.212
-5.023	-5.78936667	0.0101	0.0203	-5.017	-0.0064	0.211
0.0171	-0.70406667	0.0117	0.0235	0.064	-0.0474	0.217
4.942	4.2076	0.0131	0.0263	4.964	-0.0218	0.213
9.925	9.102	0.0145	0.0289	9.839	0.0859	0.229
14.865	14.094	0.0153	0.0306	14.806	0.0594	0.220
19.818	19.150	0.0089	0.0178	19.832	-0.0133	0.211
24.860	24.265	0.0086	0.0172	24.913	-0.0527	0.217
29.861	29.252	0.0100	0.0200	29.865	-0.0038	0.211
34.885	34.337	0.0107	0.0214	34.912	-0.0271	0.213
39.818	39.261	0.0107	0.0213	39.801	0.0167	0.212
44.781	44.278	0.0095	0.0190	44.784	-0.0030	0.211
49.844	49.400	0.0090	0.0179	49.873	-0.0287	0.213
52.360	51.905	0.0107	0.0213	52.363	-0.0032	0.211
54.829	54.378	0.0231	0.0462	54.824	0.0044	0.215
57.378	56.919	0.0130	0.0261	57.353	0.0255	0.213
59.856	59.440	0.0088	0.0177	59.864	-0.0079	0.211
62.324	61.888	0.0101	0.0202	62.3034	0.0204	0.212
64.811	64.380	0.0079	0.0158	64.789	0.0214	0.212
67.336	66.912	0.0113	0.0227	67.316	0.0203	0.212
69.879	69.495	0.0079	0.0158	69.896	-0.0172	0.211
74.869	74.482	0.0099	0.0199	74.885	-0.0159	0.211
79.782	79.379	0.0086	0.0171	79.794	-0.0121	0.211
84.759	84.329	0.0125	0.0249	84.768	-0.0093	0.212
89.650	89.164	0.0137	0.0273	89.638	0.0121	0.212
					MAX	0.229
					MIN	0.211

Table D.4: Global uncertainty for all thermocouples.

TC Number	Global Uncertainty (°C)	TC Number	Global Uncertainty (°C)	TC Number	Global Uncertainty (°C)
3	±0.23	26	±0.25	49	±0.22
4	±0.24	27	±0.23	50	±0.21
5	±0.25	28	±0.23	51	±0.22
6	±0.27	29	±0.23	52	±0.22
7	±0.25	30	±0.22	53	±0.22
8	±0.25	31	±0.22	54	±0.22
9	±0.25	32	±0.22	55	±0.22
10	±0.24	33	±0.22	56	±0.22
11	±0.23	34	±0.22	57	±0.23
12	±0.24	35	±0.22	58	±0.24
13	±0.23	36	±0.22	59	±0.25
14	±0.22	37	±0.23	60	±0.25
15	±0.22	38	±0.24	A51	±0.22
16	±0.22	39	±0.24	A52	±0.23
17	±0.22	40	±0.25	A53	±0.22
18	±0.22	41	±0.25	A54	±0.22
19	±0.22	42	±0.24	A55	±0.22
20	±0.23	43	±0.23	A56	±0.24
21	±0.24	44	±0.22	A57	±0.26
22	±0.23	45	±0.22	A58	±0.29
23	±0.23	46	±0.22	A59	±0.32
24	±0.23	47	±0.22	A60	**±0.33**
25	±0.23	48	±0.22		

As shown in Table D.4, most thermocouples have a global uncertainty less than ±0.25°C which indicates that the uncertainty associated with the reference temperature probe dominates the global uncertainty of the thermocouples. Thermocouple A60 has the maximum global uncertainty with a value of ±0.33°C. To be conservative, a global uncertainty value of ±0.35°C was assigned to all thermocouples.

D.3 Thermistor calibration

Resistance thermometry is a well-established temperature measuring technique which is based on the electrical resistance changes that a certain material undergoes as a result of temperature changes. The resistance temperature detectors (RTD) and thermistors constitute the two major classes of resistance thermometers; the former uses conductors while the latter employs semiconductors. Thermistors can be fabricated in relatively small sizes which imply that they can be used to react quickly to temperature changes. Their temperature versus resistance behavior is highly non-linear. It was planned to use negative temperature coefficient (NTC) thermistors to measure the inlet/outlet fluid temperatures. However, due to a malfunction, they were not used in the final experiment. However, the procedure to calibrate them is presented in this appendix with the goal of documenting the results for future experiments.

Two pipe plug thermistor probes (Omega TH-44032-1/8NPT-160) with a nominal electrical resistance of 30000Ω at 25°C have been chosen and calibrated to measure the inlet/outlet fluid temperature to the borehole. The thermistors were calibrated over the temperature range from -15°C to 75°C with steps of 2.5°C for the temperatures from 50°C to 70°C and 5°C temperature steps for the rest of the range. Over this temperature range, there is a sharp non-linear resistance variation: 200000Ω at -15°C and 4600Ω at +75°C. For calibration purposes, a copper sleeve was used to protect the extension wires in order to immerse the set-up in the constant temperature bath (the sleeve is shown as item 6 in Figure D.1). The measuring tip was, however, left intact and was immersed in the fluid.

The calibration procedure is the same as the one described earlier for the thermocouples. For each thermistor the averaged electrical resistances obtained during calibration are plotted against the corresponding averaged reference temperature measured via the digital platinum resistance thermometer. One such plot is shown in Figure D.4 where the exponential (logarithmic) nature of the response is evident. Based on a least square procedure, the data are curve-fitted using the following relation:

$$T_{ref,i} = a_i + b_i R_{read,i} + c_i Ln\left(R_{read,i}\right) + \frac{d_i}{Ln\left(R_{read,i}\right)} + \frac{e_i}{R_{read,i}} \qquad \text{(D.3)}$$

where $R_{read,i}$ is the electrical resistance reading from the thermistor i, $T_{ref,i}$ is the reference temperature (in °C) and a_i, b_i, c_i, d_i and e_i are the coefficients in the correlation equation for thermistor i. For each of the two thermistors (i=1 or 2), the corresponding coefficients are given in Table D.5.

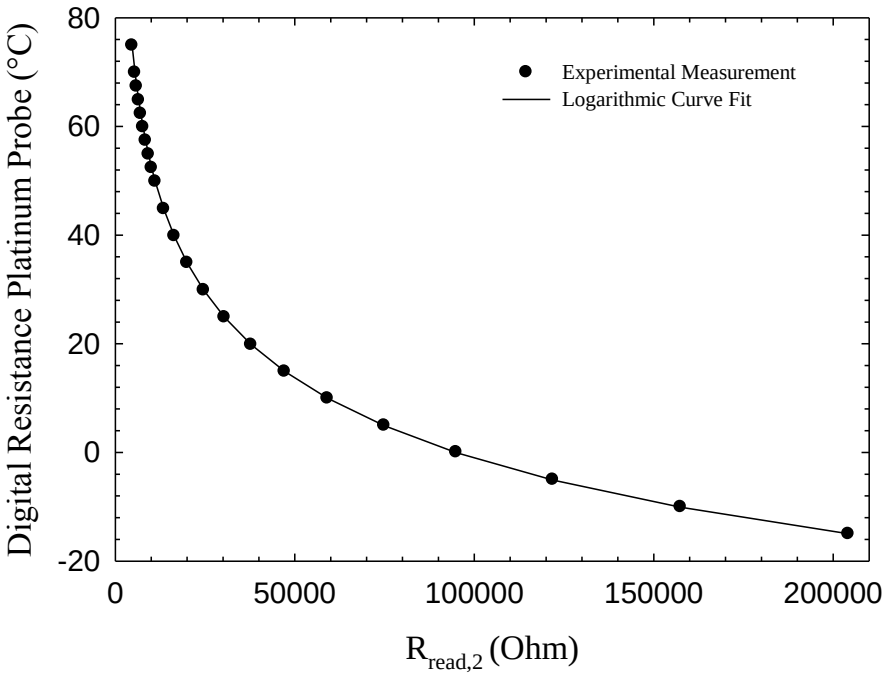

Figure D.4 : Experimental results versus the curve fitted values: Temperature-Resistance curves for thermistor # 2.

Table D.5: Coefficients of the temperature-resistance calibrations for the thermistors.

	a_i	b_i	c_i	d_i	e_i
Thermistor # 1, i=1	-162.143044	-0.0000069085	-2.95585551	2251.274365	-22782.3032
Thermistor # 2, i=2	104.7313958	0.0000115664	-15.310499	794.8910581	25988.61491

D.3.1 Uncertainty analysis for thermistors

The uncertainty analysis performed to estimate the error bands for the temperature readings yielded by each thermistor are summarized in Table D.6 and Table D.7. Much like the case of

thermocouples, the global uncertainty originates from: the uncertainties associated with the reference temperature probe; the fluctuations of the temperature measurement (actually the equivalent electrical resistance is measured in Ω); and the calibration equation. These three uncertainties are described below. It should be noted that even though the thermistor measurements are in Ω, the global uncertainty is obtained in °C.

D.3.1.1 Uncertainty of the reference temperature

As mentioned before, the uncertainty of the reference thermometer, U_1, is ±0.21°C.

D.3.1.2 Uncertainty in measuring the temperature

The electrical resistance (in Ω) are measured and recorded by the data acquisition system for a time period of five minutes at intervals of ten seconds (30 sets of data recorded) at each target temperature where its averaged value is used for the calibration. To obtain the uncertainty associated with the measurement fluctuations, readings are converted from electrical resistance (i.e., Ω) to temperature (°C) for all of the 30 readings at each target temperature. The passage from Ω to temperature (in K) is provided using the well-known Steinhart-Hart correlation which is given by:

$$T = \left(A + B(ln(R_{read,i})) + C(ln(R_{read,i}))^3 \right)^{-1} \quad \text{(D.4)}$$

where $R_{read,i}$ is the electrical resistance reading from the thermistor i . For the thermistors installed on the experimental apparatus (TH-44032-1/8NPT-160), A=9.376e-4 , B=2.208e-4 and C=1.276e-7. The calculated temperatures are converted from Kelvin (i.e., K) to °C. Note that equation D.4 is only used here to obtain temperature fluctuations.

The impact of the temperature measurement fluctuations are accounted for by first calculating the standard deviation of the set of 30 temperatures. The uncertainty associated with temperature measurement fluctuations, denoted by U_2, is assumed to be twice the standard deviation, 2σ.

D.3.1.3 Uncertainty of the correlation equation in predicting the temperature

Denoted by U_3, the uncertainty of the correlation represents the absolute difference between the reference temperature and the one calculated from the correlation equation. The values of U_3 are given in Table D.6 and Table D.7.

D.3.1.4 Global uncertainty of the thermistor measurements

Applying the method of propagation of the uncertainties presented by Coleman and Steele (1999), U_g, the global uncertainty is obtained from Equation(D.2).

Table D.6: Uncertainty calculation summary for thermistor # 1.

Target Temperature (°C)	**RTD (°C)**	**Thermistor #1 (°C)**	**σ (°C)**	**U_2=2 σ (°C)**	**Calibration Curve fit (°C)**	**U_3 (°C)**	**U_g (°C)**
-15	-15.015	-14.142	0.004	0.008	-15.010	-0.006	0.210
-10	-10.056	-9.339	0.005	0.010	-10.054	-0.002	0.210
-5	-5.023	-4.414	0.004	0.008	-5.024	0.001	0.210
0	0.017	0.524	0.004	0.009	-0.009	0.027	0.212
5	4.942	5.359	0.002	0.004	4.885	0.057	0.218
10	9.925	10.431	0.011	0.023	10.013	-0.088	0.229
15	14.865	15.252	0.006	0.012	14.888	-0.023	0.212
20	19.818	20.155	0.010	0.021	19.851	-0.033	0.214
25	24.860	25.070	0.003	0.005	24.833	0.027	0.212
30	29.861	30.019	0.018	0.036	29.858	0.003	0.213
35	34.885	34.899	0.017	0.034	34.821	0.065	0.222
40	39.818	39.761	0.033	0.066	39.768	0.050	0.226
45	44.781	44.672	0.052	0.104	44.769	0.012	**0.235**
50	49.844	49.713	0.008	0.016	49.898	-0.054	0.217
52.5	52.360	52.185	0.011	0.022	52.411	-0.051	0.217
55	54.829	54.620	0.007	0.014	54.884	-0.056	0.218
57.5	57.378	57.093	0.015	0.030	57.392	-0.014	0.213
60	59.856	59.514	0.014	0.028	59.843	0.013	0.212
62.5	62.324	61.947	0.014	0.028	62.301	0.023	0.213
65	64.811	64.420	0.016	0.032	64.793	0.018	0.213
67.5	67.336	66.869	0.031	0.063	67.253	0.083	0.234
70	69.879	69.523	0.005	0.009	69.912	-0.033	0.213
75	74.869	74.527	0.006	0.012	74.889	-0.020	0.211
						Max	**0.235**
						Min	**0.210**

Table D.7: Uncertainty calculation summary for thermistor # 2.

Target Temperature (°C)	**RTD (°C)**	**Thermistor #2 (°C)**	**σ (°C)**	**U_2=2 σ (°C)**	**Calibration Curve fit (°C)**	**U_3 (°C)**	**U_g (°C)**
-15	-15.015	-14.790	0.002	0.004	-14.969	-0.046	0.215
-10	-10.056	-9.902	0.002	0.004	-10.087	0.030	0.212
-5	-5.023	-4.935	0.001	0.002	-5.073	0.050	0.216
0	0.017	0.044	0.002	0.003	-0.024	0.041	0.214
5	4.942	4.917	0.004	0.008	4.922	0.020	0.211
10	9.925	9.909	0.011	0.023	9.982	-0.057	0.219
15	14.865	14.802	0.004	0.007	14.925	-0.060	0.218
20	19.818	19.712	0.003	0.006	19.871	-0.053	0.217
25	24.860	24.712	0.001	0.003	24.892	-0.031	0.212
30	29.861	29.665	0.002	0.004	29.853	0.008	0.210
35	34.885	34.677	0.003	0.005	34.865	0.020	0.211
40	39.818	39.576	0.005	0.011	39.766	0.052	0.217
45	44.781	44.529	0.004	0.008	44.727	0.053	0.217
50	49.844	49.568	0.003	0.007	49.792	0.052	0.216
52.5	52.360	52.071	0.005	0.009	52.318	0.042	0.214
55	54.829	54.532	0.003	0.007	54.811	0.018	0.211
57.5	57.378	57.056	0.005	0.009	57.377	0.002	0.210
60	59.856	59.503	0.007	0.014	59.876	-0.020	0.211
62.5	62.324	61.951	0.006	0.011	62.390	-0.066	0.220
65	64.811	64.263	0.005	0.009	64.777	0.034	0.213
67.5	67.336	66.861	0.010	0.020	67.477	-0.141	0.254
70	69.879	69.273	0.015	0.030	70.002	-0.123	0.245
75	74.869	73.706	0.044	0.089	74.694	0.175	**0.287**
						MAX	**0.287**
						MIN	0.210

As one can observe from see from Table D.6 and Table D.7, thermistor 1 has a maximum global uncertainty of ±0.235°C while the global uncertainty of thermistor 2 is ±0.287°C. The global uncertainty of the temperature readings provided by the thermistors is considered to be ±0.3°C.

APPENDIX E

Calibration of the flow meter

E.1 Introduction

The volume flow rate is measured using a turbine flow meter (FTB-1311 by Omega). It measures flow rates in the range from 0.08 to 0.4 Gallons per minute (GPM). The output signal from this device can either be set to frequency (in Hz) or DC current (in mA). According to the calibration document provided by the manufacturer of this flow meter, an output signal of 4 mA or 182.9 Hz corresponds to the minimum flow rate this device can measure (a flow rate of 0.08 GPM equivalent to 0.005 L/s) while 20 mA or 929 Hz corresponds to the higher end of its operating range (i.e., 0.402 GPM or 0.025 L/s). The output signal of the flow meter is set to frequency. The manufacturer reports that the accuracy of the device is ±1%.

The turbine flow meter is composed of a rotor with blades (similar to a paddle wheel) and a coil that induces a magnetic field. Fluid passing through the flow meter forces the rotor to turn at an angular speed proportional to the flow rate and generating an electronic pulse. The so-called *K*-factor, which is defined as the number of electronic pulses generated per unit volume of fluid passing through the flow meter, is unique to each meter and is constant over the flow meter's operating range. The *K*-factor provided by the manufacturer is 137933.5 pulses/gallon.

In the course of the current research, three independent sets of calibrations were carried out at different periods. The first one was successfully performed on June 30, 2010. However after a few months of operation the flow meter did not function properly. The problem was due to the growth of some sort of fungus inside the water in the constant temperature bath which had blocked the flow meter's passage and immobilized the rotor. After fixing the problem a second calibration was undertaken on November 5, 2010. As the results from the first and second calibrations did not match, further investigations were undertaken and the rotor shaft was found to be defective. After replacing the faulty part, the final calibration was carried out on February 21, 2011. The results presented below are for this third calibration.

E.2 Calibration procedure

The flow meter calibration is simply based on comparing the measured flow rates against a reference flow rate obtained here using a classic stopwatch and bucket method as illustrated in Figure E.1.

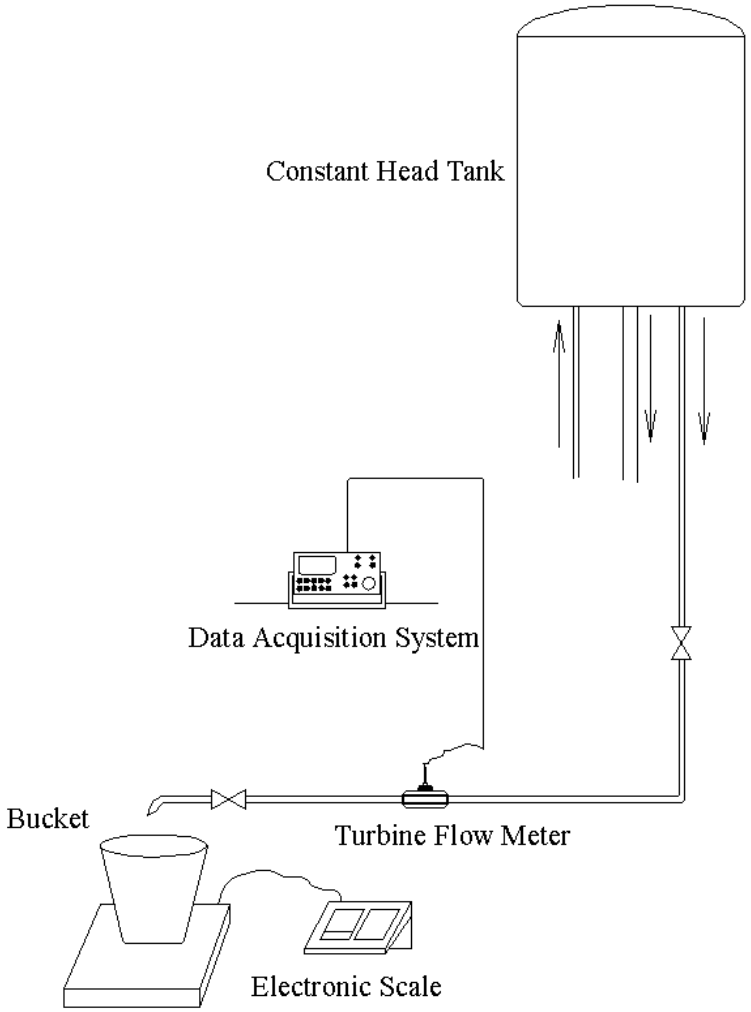

Figure E.1: Schematic of the experimental setup used for calibrating the flow meter.

The stopwatch and bucket method consists of measuring the time required to accumulate a certain mass of water in a bucket. An electronic scale, (OHAUS, model DS4) with a maximum capacity of 20 kg is used for weighing the water quantity. The elapsed time is determined by a stopwatch.

To carry out the calibration, the flow rate is first set to a certain value using a valve at the outlet of the constant head tank. It was found to be preferable to begin with a flow rate close to one

extreme of the flow meter's operating range and sweep towards the other one. The initial mass of the bucket is recorded and when the desired flow rate is obtained, the bucket is put in place under the flow and the stopwatch is started while the data acquisition system is activated to record (at two seconds intervals) the output signal of the flow meter (i.e., frequency) into a file. Once approximately five kilograms of water has accumulated in the bucket, the bucket is diverted to its original position and the stopwatch is stopped simultaneously. The temperature of the water is measured and recorded three times during each test using a T-type thermocouple. This procedure is repeated for another flow rate until the whole operating range of the flow meter is covered. The reproducibility of the calibration measurements is verified by repeating the procedure a second time over the whole operating range. Thus, two rounds of calibration are reported.

The reference mass flow rate is obtained by dividing the measured net water mass, m_{net}, by the measured filling time. Dividing the mass flow rate by the water density (corresponding to the measured water temperature) gives the reference volumetric flow rate.

E.3 Calibration results

The data obtained from both calibration rounds are summarized in Table E.1 and plotted in Figure E.2. The calibration points provided by the manufacturer are also presented on this figure. This figure shows that the response of the flow meter is linear and that the measured data correspond to the data supplied by the manufacturer.

By definition, the so-called flow meter *K*-factor is obtained from a linear relationship relating the frequency to the flow rate:

$$K = \frac{f}{Q_{measured}} \tag{E.1}$$

where;

f: is the flow meter output signal (Hz)

$Q_{measured}$: is the reference volume flow rate of the fluid passing through the flow meter (Gallons per minute in the present case). The units of K are in pulses/gallon.

Table E.1: Summary of the calibration data for FTB-1311 turbine flow meter.

Round	*Test*	*t, Measured time (s)*	*m_{net}, Net water mass (kg)*	*Water temperature (°C)*	*Density (kg/m^3)*	*Net volume (L)*	*$Q_{measured}$ Reference flow rate (L/s)*	**Average frequency (Hz)**
1	1	202.41	5.02	3.5	1000.8	5.02	0.025	899.131
	2	213.06	5.00	3.5	1000.8	5.00	0.023	851.713
	3	227.4	5.00	3.3	1000.8	5.00	0.022	799.662
	4	248.56	5.00	3.5	1000.8	5.00	0.020	733.734
	5	280.94	5.00	3.5	1000.8	5.00	0.018	651.207
	6	331.59	5.00	3.95	1000.7	5.00	0.015	553.618
	7	372.6	5.00	3.9	1000.8	5.00	0.013	492.789
	8	408.25	5.00	3.9	1000.8	5.00	0.012	448.890
	9	457.69	5.00	4.05	1000.7	5.00	0.011	400.517
	10	523.22	5.00	4.5	1000.7	5.00	0.010	351.234
	11	610.9	5.00	4.8	1000.6	5.00	0.008	301.547
	12	740.16	5.00	5	1000.6	5.00	0.007	247.537
	13	923.25	5.00	5.65	1000.5	5.00	0.005	198.077
	14	1006.06	5.00	7.4	1000.3	5.00	0.005	181.054
2	1	197	5.00	3.6	1000.8	5.00	0.025	920.671
	2	228.25	5.00	3.4	1000.8	5.00	0.022	797.696
	3	259.72	5.00	3.6	1000.8	5.00	0.019	701.918
	4	305.56	5.00	3.75	1000.8	5.00	0.016	599.158
	5	367.22	5.00	4.2	1000.7	5.00	0.014	500.630
	6	460.32	5.02	4.8	1000.6	5.02	0.011	399.443
	7	614.53	5.00	5.45	1000.6	5.00	0.008	299.634
	8	910	5.00	7.5	1000.3	5.00	0.005	200.529
	9	1034.75	5.00	13	999.45	5.00	0.005	175.586

A linear curve fit of all the data from both calibrations rounds gives the following value for the *K*-factor:

$$K = 137318 \text{ pulses/gallon} \tag{E.2}$$

The percentage difference between this *K*-factor and the one given by the manufacturer (137933.5 Pulse/gallon) is 0.44%.

Finally, based on the data provided in Figure E.2, the correlation relating the flow rate to the measured frequency is given by:

$$Q = -0.00010036 + 2.75645\text{e-}05 \times f \tag{E.5}$$

where Q is the calculated flow rate (L/s) and f is the frequency (Hz).

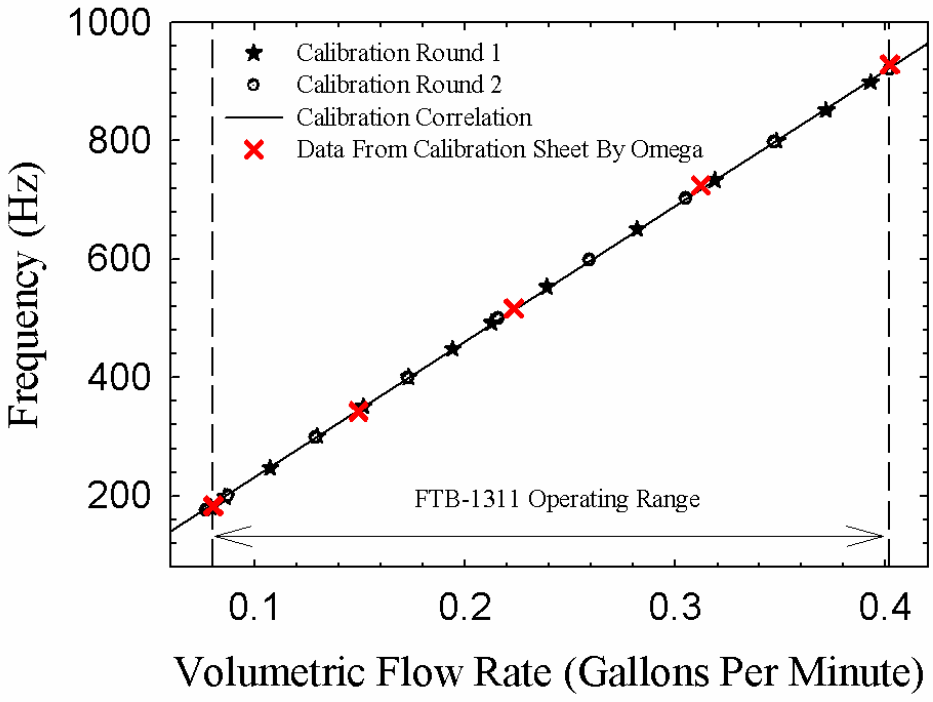

Figure E.2: Calibration of the FTB-1311 turbine flow meter together with its *K*-factor.

E.3 Uncertainty of the results

The global uncertainty is composed of the uncertainties associated with the reference flow rate measurement, the frequency measurement, and the calibration equation. Each of these components is evaluated below:

E.3.1 Uncertainty in the stopwatch and bucket measurement

The electronic scale itself was not calibrated and the uncertainty associated to weighing the mass of fluid was conservatively assumed to be ± 0.01 kg.

The uncertainty associated with the time measurement was estimated to be ± 0.1 s. Following the method of propagation of the uncertainties (AHRAE/ANSI, 1986 ; Coleman and Steele, 1999), the combined uncertainty associated with the stopwatch and bucket measurement, U_1, is:

$$U_1 = Q_{measured}\sqrt{\left(\frac{0.01}{m_{net}}\right)^2 + \left(\frac{0.1}{t}\right)^2} \tag{E.3}$$

where;

$Q_{measured}$: measured volume flow rate (L/s),

m_{net}: net measured mass (kg),

t: time measured during each test (s).

E.3.2 Uncertainty in measuring the frequency

The frequency is measured and recorded by the data acquisition system every 2 seconds. Its averaged value is used for the calibration and uncertainty analysis. At each of the measured flow rates, the impact of the fluctuation of the measured frequency has to be taken into account. It leads to analyzing the uncertainty associated with measuring frequency, U_2, which is obtained from:

$$U_2 = \frac{2\sigma}{K} \tag{E.4}$$

where σ is the standard deviation of the measured frequency. The uncertainty associated with measuring the frequency calculated from Equation (E.4) covers 95.5% of the measured data, i.e., twice the standard deviation.

E.3.3 Uncertainty of the correlation equation in predicting the flow rate

Denoted by U_3, the uncertainty of the correlation represents the absolute difference between the reference flow rate and the one calculated from the correlation equation. The resulting values are shown in Table E.2.

E.3.4 Global uncertainty

Applying the method of propagation of the uncertainties presented by Coleman and Steele (1999), U_g, the global uncertainty is obtained from Equation E.5.

$$U_g = \sqrt{U_1^2 + U_2^2 + U_3^2}$$
$$U_{rg} = 100\frac{U_g}{Q_{measured}} \tag{E.5}$$

where U_g denotes the absolute global uncertainty and U_{rg} stands for the relative global uncertainty. These values are shown in the last two columns of Table E.2.

An analysis of Table E.2 reveals that the relative global uncertainty is below 1% for most of the operating range. For low flow rates, the relative global uncertainty is higher than 1% and it reaches a value of 3.11% in the case of test 9 in round 2. Given that the final experiment is performed for a flow rate of ≈ 0.0114 L/s, the global uncertainty assigned to the flow rate in the final experiment was assigned a conservative value of ±1.50% for flow rates above .006 L/s

Table E.2: Summary of the uncertainty analysis results for FTB-1311 turbine flow meter.

Round	Test	Measured flow rate (L/s)	Average frequency (Hz)	Curve fitted flow rate (L/s)	U_1 (L/s)	2σ (95.5%)	U_2 (L/s)	U_3 (L/s)	U_g (L/s)	U_{rg} (%)
1	1	0.0248	899.13	0.0247	5.09E-05	3.482	9.60E-05	9.65E-05	1.45E-04	0.59
	2	0.0234	851.71	0.0234	4.82E-05	1.817	5.01E-05	7.11E-05	9.94E-05	0.42
	3	0.0220	799.66	0.0219	4.50E-05	3.137	8.65E-05	2.68E-05	1.01E-04	0.46
	4	0.0201	733.73	0.0201	4.10E-05	1.263	3.48E-05	2.58E-05	5.97E-05	0.30
	5	0.0178	651.21	0.0178	3.61E-05	1.071	2.95E-05	6.74E-05	8.20E-05	0.46
	6	0.0151	553.62	0.0152	3.05E-05	1.087	3.00E-05	9.30E-05	1.02E-04	0.68
	7	0.0134	492.79	0.0135	2.71E-05	2.456	6.77E-05	7.46E-05	1.04E-04	0.78
	8	0.0122	448.89	0.0123	2.47E-05	1.006	2.77E-05	3.55E-05	5.13E-05	0.42
	9	0.0109	400.52	0.0109	2.20E-05	1.741	4.80E-05	2.38E-05	5.79E-05	0.53
	10	0.0095	351.23	0.0096	1.92E-05	0.959	2.64E-05	3.19E-05	4.57E-05	0.48
	11	0.0082	301.55	0.0082	1.64E-05	2.255	6.22E-05	3.26E-05	7.21E-05	0.88
	12	0.0068	247.54	0.0067	1.35E-05	1.583	4.36E-05	2.79E-05	5.35E-05	0.79
	13	0.0054	198.08	0.0054	1.08E-05	3.402	9.38E-05	5.29E-05	1.08E-04	2.00
	14	0.0050	181.05	0.0049	9.95E-06	3.021	8.33E-05	7.79E-05	1.14E-04	**2.30**
2	1	0.0254	920.67	0.0253	5.23E-05	3.803	1.05E-04	8.21E-05	1.43E-04	0.56
	2	0.0219	797.70	0.0219	4.48E-05	3.105	8.56E-05	6.99E-07	9.66E-05	0.44
	3	0.0192	701.92	0.0192	3.92E-05	1.456	4.01E-05	1.22E-05	5.74E-05	0.30
	4	0.0164	599.16	0.0164	3.31E-05	1.046	2.88E-05	6.50E-05	7.85E-05	0.48
	5	0.0136	500.63	0.0137	2.75E-05	2.594	7.15E-05	9.38E-05	1.21E-04	0.89
	6	0.0109	399.44	0.0109	2.18E-05	1.638	4.52E-05	1.22E-05	5.16E-05	0.47
	7	0.0081	299.63	0.0082	1.63E-05	2.479	6.83E-05	2.75E-05	7.55E-05	0.93
	8	0.0055	200.53	0.0054	1.10E-05	2.033	5.61E-05	6.56E-05	8.70E-05	1.58
	9	0.0048	175.59	0.0047	9.68E-06	4.204	1.16E-04	9.52E-05	1.50E-04	**3.11**